On the Mathematical Analysis of the Relationship Between the Bulging Region and the Centerline Solidification Cracking in Laser Beam Welding

vorgelegt von
M.Sc.
Antoni Edit Artinov
ORCID:0000-0001-7533-5014

an der Fakultät V - Verkehrs- und Maschinensysteme
der Technischen Universität Berlin
zur Erlangung des akademischen Grades

Doktor der Ingenieurwissenschaften
- Dr.-Ing. -

genehmigte Dissertation

Promotionsausschuss:

Vorsitzender:	Prof. Dr. rer. nat. Valentin Popov
Gutachter:	Prof. Dr.-Ing. Michael Rethmeier
Gutachter:	Prof. Dr.-Ing. habil. Jean Pierre Bergmann

Tag der wissenschaftlichen Aussprache: 31. Mai 2023

Berlin 2024

Acknowledgment

This Ph.D. thesis was completed during my time working as a research associate in Division 9.3 Welding Technology at the Bundesanstalt für Materialforschung und -prüfung (BAM) in Berlin, Germany. I extend my sincere thanks to everyone who played a pivotal role in making this work possible.

First and foremost, I would like to express my gratitude to my doctoral advisor and division head, Prof. Dr.-Ing. Michael Rethmeier, for his guidance, support, and the main evaluation of the thesis. I am equally thankful to Prof. Dr.-Ing. habil. Jean Pierre Bergmann from Technische Universität Ilmenau for evaluating the thesis manuscript and providing a second expert opinion, as well as to Chairman Prof. Dr. rer. nat. Valentin Popov from Technische Universität Berlin for his valuable contributions.

Furthermore, I want to convey my deepest appreciation to Prof. Dr.-Ing. habil. Victor A. Karkhin from the Peter the Great St. Petersburg Polytechnic University, whose intensive guidance, support, and discussions significantly contributed to the success of this thesis. I owe a debt of gratitude to Dr.-Ing. Marcel Bachmann, who has supported and supervised me from day one.

In addition to my academic mentors, I am indebted to my colleagues, both current and former, whose exceptional support and knowledge exchange have significantly contributed to the advancement of my work. In particular, I want to mention my office colleague of many years, Dr.-Ing. Xiangmeng Meng, and thank him for his invaluable advice, insightful discussions, and constant support.

Lastly, I would like to express my heartfelt gratitude to my family and friends for their unwavering belief in me.

Antoni Artinov Berlin, May 2023

Abstract

The present Ph.D. thesis provides a comprehensive experimental and theoretical study of the bulging-cracking relationship in laser beam welding of thick unalloyed steel sheets. It focuses on experimentally proving the existence of the bulging region and on developing a coupled multiphysics mathematical framework to analyze its influence on the three critical factors controlling the susceptibility to solidification cracking, namely the thermal, metallurgical, and mechanical factors.

The research employs a novel experimental setup, utilizing a combination of transparent quartz glass and thick unalloyed steel sheet, enabling real-time visualization of the weld pool geometry and confirming the existence of a distinctive bulging region. To deepen the understanding of these experimental insights, an extensive multiphysics mathematical framework was developed and rigorously verified and validated. This framework introduces an innovative approach using Lamé curves for accurately describing complex three-dimensional weld pool geometries, including the bulging region's characteristics. Through analytical solutions and numerical procedures, it facilitates the computation of solidification parameters, which are crucial for understanding the metallurgical aspects of crack formation. The framework also incorporates a mechanical model to assess and evaluate the local stress distribution within the bulging region.

The findings indicate that an elongated, sharply shaped bulging region significantly increases the susceptibility to solidification cracking. This is attributed to its adverse impact on the distribution and local dwell time of liquid metal residing at grain boundaries during solidification, combined with the localized tensile stresses identified in the bulging region.

In essence, this research contributes to the broader understanding of solidification cracking in laser beam welding of thick unalloyed steel sheets, with a particular focus on the bulging region. The insights and methodologies developed in this thesis are valuable for future research and advancements in the application of the laser beam welding technology for joining high-thickness unalloyed steel components.

Contents

1 Introduction

> "With four parameters I can fit an elephant, and with five I can make him wiggle his trunk."
>
> John von Neumann

Laser beam welding (LBW) is an established high-performance joining process utilized in various industrial applications, e.g., for welding thin sheets in the automotive industry. It offers several advantages when compared to conventional arc welding methods. On the one hand, it results in a narrow heat affected zone (HAZ) and low distortion of the welded components due to the highly concentrated and precise heat input, especially when large-area parts are joined. On the other hand, it allows for high achievable welding speed and requires minimal to no consumption of filler material [1]. Due to the significant development of modern laser sources in the past 20 years, high-power laser systems of up to 100 kW have become available on the market. These enable, in particular, the joining of thick-walled structures, reaching wall thicknesses of up to 50 mm, by fewer passes or even by a single pass [2]. Hence, nowadays, the LBW process offers tremendous potential for more effective joining of steel sheets of higher thickness, such as those used in the production of pipelines for the oil and gas industry, crane construction, shipbuilding, and aerospace applications.

The trend toward increasing welding speed ($> 2\,\mathrm{m\,min^{-1}}$) and sheet thickness ($> 10\,\mathrm{mm}$) is, however, limited by the formation of weld imperfections that are untypical for low-alloyed and unalloyed steel sheets welded under conventional conditions. One of the most critical limiting factors is the occurrence of solidification cracks, as these are decisive for the reliability and safety of the joined components [3, 4]. Generally, the susceptibility to solidification cracking is mainly controlled by the thermo-metallurgical and thermo-mechanical interactions [5], and therefore by three dominant factors. These are the thermal, metallurgical, and mechanical factors. The dominant factors are coupled and depend strongly on the weld pool geometry, and vice versa [6, 7]. The weld pool geometry, on the other hand, is long-known to be crucial for the formation of weld imperfections during solidification [8, 9]. Experimental studies on deep penetration electron beam welding (EBW) of thick low-alloyed and unalloyed steel sheets suggest a strong correlation between the geometrical characteristics of the weld pool and the susceptibility to solidification cracking [10, 11]. Specifically, the presence of a so-called bulging region within the weld pool, characterized by local elongation and widening, was found to be highly susceptible to centerline solidification cracking. [12]. The link between the bulging region and the formation of centerline cracks has been confirmed in more recent studies on high power LBW of thick unalloyed steel sheets [13–15]. Nevertheless, due to the optical inaccessibility of the LBW process, the bulging region has been only observed in

metallographic macro sections rather than in real time. Furthermore, the significant influence of this region on the three dominant factors controlling the cracking behavior remains poorly understood and has yet to be studied in detail. Therefore, considering the current state of knowledge, a need to expand the understanding of the complex relationship between the bulging region and the susceptibility to centerline solidification cracking therein arises.

The present work aims to perform a methodical experimental and theoretical analysis of the influence of the bulging region on the local susceptibility to centerline solidification cracking in LBW of thick unalloyed steel sheets. For this purpose, first, the occurrence of a bulging region during the LBW process has to be experimentally confirmed. Then, in subsequent steps, the dependence of the thermal, metallurgical, and mechanical factors on the bulging region has to be estimated by applying analytical and numerical methods, allowing to overcome the optical inaccessibility of the LBW process. Finally, several experimental measurements must be performed to verify and validate the developed models and the corresponding theoretical results.

2 State of the Art

This chapter outlines the main process features involved in deep penetration welding of thick steel sheets, with a specific focus on the LBW process employed in the present work. Based on this, an analysis of the significant factors influencing the cracking behavior of the welded components is performed. Furthermore, the relationship between weld solidification cracking and a local elongation and widening of the weld pool, known as a bulging region, is described. Following, modeling techniques that can contribute to the fundamental understanding of this kind of weld imperfections are presented. Finally, the objectives of the work are set based on the current state of knowledge.

2.1 Deep Penetration Welding

The joining of semi-finished steel components with wall thicknesses above 10 mm is essential for many industrial applications, including the production of pipelines for the oil and gas industry, shipbuilding, crane construction, and the assembly of vast pressure and reactor chambers. Two criteria must be met to obtain welds of high penetration depths. First, extremely high power densities of above $10^6\,\mathrm{W\,cm^{-2}}$ are needed. Second, the energy must be effectively absorbed by the material [16]. When these criteria are fulfilled, most metallic materials subjected to the welding process will undergo melting followed by vaporization, producing a deep, narrow, vapor-filled cavity known as a keyhole, surrounded by liquid metal. When the energy source is traversed along the weld trajectory, the keyhole moves with it through the workpiece at the welding speed. The keyhole geometry changes dynamically during welding, depending on the balance of forces acting on its surface, as illustrated schematically in Figure 2.1. The forces include, above all, the ablation force, the friction force of the rising metallic vapor, the capillary pressure (Laplace pressure), the static and dynamic pressure of the liquid metal and the metallic vapor, the buoyancy forces induced by the density differences, and the thermo-capillary force resulting from the variation of the surface tension with temperature. As a result, the liquid metal flows around the keyhole and solidifies at the rear part of the weld pool. Typically, keyhole welding produces a weld seam characterized by a nearly parallel-sided fusion zone (FZ), a narrow width, and a uniform internal structure. Moreover, the weld depth is typically about ten to fifteen times greater than the weld width [16]. The high weld seam depth-to-width ratio indicates that most of the locally absorbed energy serves for melting the interfaces to be joined. Hence, deep penetration welding is one of the most efficient joining processes, especially in the case of partial penetration welding, as no laser energy gets lost through the bottom of the keyhole.

In the welding field, the joining efficiency is defined as $v_{\mathrm{weld}}\,h/P$, where v_{weld} is the traverse welding speed in $\mathrm{mm\,s^{-1}}$, h is the thickness of the weld in mm, and P is the incident power

in kW. Although this is not the true efficiency, as it has the unit of $mm^2\,kJ^{-1}$, by comparing the joining efficiency of various welding methods, it becomes evident that an electron beam or a laser beam offers the highest power density available to industry at present [16]. Therefore, deep penetration welding can be easily achieved by utilizing each of these as an energy source. In fact, single-pass welding of thick-walled metal structures has been successfully applied for the first time in EBW [17]. Nonetheless, the EBW process is not well suited for joining components with large dimensions since vast vacuum chambers are required for this purpose. In contrast to EBW, LBW does not require a low-pressure environment but offers a similar power density to an electron beam. Moreover, LBW enables the processing of magnetic materials. This feature is particularly important for complete penetration welding of thick steel components as it allows to use an electromagnetic weld pool support, preventing the drop-out of liquid metal on the weld root caused by the force of gravity [18].

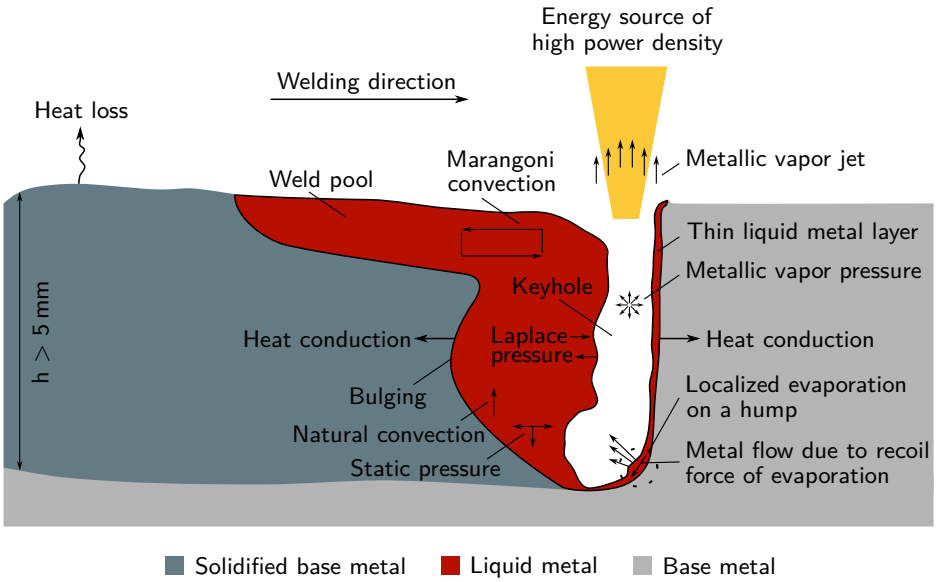

Figure 2.1: Schematic of the deep partial penetration welding process in the longitudinal section, illustrating the keyhole geometry, energy source, and main acting forces in the liquid and vapor phases

In general, the laser systems are divided into gas, solid-state, liquid, and semiconductor lasers, depending on the type of the applied active medium. Thereby, the most common types used in industry and research are the gas and the solid-state lasers, represented by the CO_2 (carbon dioxide) laser and the Yb/Nd:YAG (Ytterbium/Neodymium doped Yttrium Aluminum Garnet) lasers, respectively [16]. In addition to the higher achievable penetration

depth, the LBW process offers several further benefits, including [19]:

- Suitable for processing a range of metallic materials and thicknesses, including reflective and magnetic materials. The latter capability enables the utilization of electromagnetic weld pool support to prevent the drop-out of liquid metal on the weld root.
- Highly concentrated, precise, and low heat input, resulting in a narrow HAZ and low distortion of the welded components, especially when large-area components are joined.
- High degree of flexibility, in particular for solid-state lasers as these use fiber optic cables to deliver the beam.
- High automation degree and achievable welding speed, ensuring efficient economic production.
- Very accurate welding with no to minimal consumption of filler material.

In LBW, the keyhole serves as an optical black body, with the entering laser beam reflecting multiple times off its walls. As a result of the multiple reflections, the laser beam energy is nearly entirely absorbed by the liquid metal, and the efficiency of the welding process rises, enabling deep penetration welding [16]. However, the maximum penetration depth differs for the different LBW processes. The maximum achievable penetration depth for the older generation of high-power CO_2 laser systems is limited, for example, by the laser beam wavelength of 10.6 µm as this results in low energy absorption, e.g., approximately 10% for steel and only 2% for aluminium. In addition, the high wavelength of the laser beam contributes to the formation of charged plasma, resulting from the ionization of the hot metallic vapor. Consequently, the plasma attenuates the laser beam, causing the weld seam depth-to-width ratio to decrease, and thus limiting the single-pass welding with CO_2 lasers to sheet thicknesses below 20 mm [20]. In contrast, due to the development of modern solid-state disk and fiber laser systems with available power of up to 100 kW and a wavelength of about 1 µm, the single-pass welding of steel sheets of thicknesses exceeding 50 mm has been enabled [2]. Moreover, these lasers can achieve a sound, complete penetration welding of even thicker components by using a double-sided laser beam, i.e., two passes from both surface sides. According to [21], complete penetration of 70 mm thick steel sheets have been realized when welding under atmospheric pressure. At a low vacuum of approximately 1 kPa, however, the maximum wall thickness of the joined steel components reached up to 125 mm.

2.2 Solidification Cracking in Deep Penetration Laser Beam Welding

With the increase in the available laser power, not only the application possibilities grow but also the necessity to better understand the phenomena and effects that occur during LBW of thick steel components [22, 23]. As described in the section above, a unique feature of deep penetration LBW is the small quantity of energy required for joining the components due to the highly concentrated heat input. Furthermore, the LBW process is characterized

by relatively high welding speeds and overheating in the weld center, resulting in rapid local cooling rates in the order of $10^3\,\mathrm{K\,s^{-1}}$, and thus very short cooling times of the weld metal. Accordingly, the solidification conditions may become critical, leading to weld solidification cracking, which is decisive for the reliability and safety of the joined components [6, 7, 24].

Solidification cracks are among the material- and process-related challenges that must be overcome to successfully integrate the LBW technology for joining components of high wall thicknesses into everyday industrial practice. The occurrence of solidification cracking represents a long-known problem in the welding field, being the object of study in many research works since the early 1930s [6, 13, 25–27]. The correlation between the laser beam and laser-hybrid welding of thick low-alloyed and unalloyed steel sheets and the occurrence of cracking was identified experimentally in [3, 13, 28]. It was discovered that in contrast to conventional arc welding processes, centerline cracks form most frequently and represent one of the most critical material failures in deep penetration LBW of unalloyed steel sheets. However, the mechanisms involved in their formation are highly complex and have not yet been researched to their full extent. One reason for this is the challenging experimental accessibility of the environment in which solidification cracks form and propagate, making three-dimensional and time-dependent measurements during the LBW process difficult or even impossible to perform [29–31]. On the other hand, as the physical effects of the LBW process and the mechanism involved in the formation of cracks are strongly coupled and highly nonlinear, the theoretical study of the cracking problem is often simplified and limited to single aspects to ensure numerical stability and moderate computing time [32, 33].

With regard to the available literature on the topic, the main critical conditions required for the formation of solidification cracks can be identified. The first critical condition is the presence of liquid metal between the coalescing solidification fronts [14, 26]. This condition is derived from observations of the fracture surfaces of solidification cracks [7, 13]. In these studies, the cracks were fractured, and their surfaces were examined with a scanning electron microscope (SEM). Thereby, it was discovered that the crack surfaces fit well together, indicating that only a thin liquid film was present between them at the moment of crack formation. The SEM observations also showed that the fracture surfaces are predominantly smooth and that the dendrite tips are well-rounded, undeformed, and regularly arranged. These findings suggest that solidification cracks form during the final solidification stage at temperatures higher than the local solidus temperature. Hence, the second critical condition is strongly related to the first one and is given by the dwell time of the liquid film residing on the grain boundaries [34, 35]. The third condition is as well derived from the SEM observations. It is based on the discovery of solid metal bridges at the boundary between the fracture surfaces and the crack. The existence of such bridges suggests that the faces of the crack were moved apart during solidification. Therefore, the third critical condition for the crack formation is the increase in the local strains and stresses causing the rupture of the liquid film residing on the grain boundaries [31, 36, 37].

The three critical conditions required for the formation of weld solidification cracks depend on several factors and their various interrelationships. According to [5], the susceptibility to solidification cracking is mainly determined by the thermo-metallurgical and thermo-mechanical interactions. These control the solidification microstructure and the local and

global strains and stresses, respectively. Therefore, three dominant factors, which govern the local susceptibility to solidification cracking, can be identified, namely the thermal, metallurgical, and mechanical factors. Nonetheless, in reality, the dominant factors represent the combined influence of many sub-factors as indicated in Table 2.1. The relationships between the three dominant factors and the three critical conditions required for the formation of weld solidification cracks are schematically represented in Figure 2.2. As depicted in the figure, the thermal factor determines the presence of liquid metal, and thus directly influences the first critical condition. In contrast, the second and third critical conditions are influenced by two dominant factors and their interactions. The dwell time of the liquid film residing on the grain boundaries is determined by the thermo-metallurgical interactions, therefore involving both the thermal and the metallurgical factor. Thereby, the thermal factor controls the liquid metal distribution and the cooling rate, whereas the metallurgical factor controls the local solidus temperature. The local change of the solidus temperature, however, is governed by the segregation process, which leads to the accumulation of liquating elements, such as S and P, ahead of the solidification front. As a consequence of the non-uniform distribution of these impurities, locally, the solidification interval extends to lower temperatures, i.e., the local solidus temperature decreases, and the dwell time of the liquid film residing on the grain boundaries increases [33, 38, 39]. On the other hand, the localized strains and stresses, which represent the third critical condition for the formation of solidification cracks, are determined by the thermo-mechanical interactions. Therefore, these interactions involve both the thermal and mechanical factors. Here, the thermal factor controls the shrinkage force generated in the weld metal during solidification, and the mechanical factor controls the response of the solid metal to the shrinkage of the liquid metal surrounded by it.

Table 2.1: Sub-factors influencing the three dominant factors controlling the susceptibility to solidification cracking [5, 7, 35]

Mechanical factor	Thermal factor	Metallurgical factor
Component and weld geometry	Welding speed	Lattice type of weld metal
Restraint intensity	Focal position	Grain structure and size
Pre-loading	Energy input	Chemical composition
Tacking	Wire feed	Solidification interval
Thermomechanical/Thermophysical material properties		
...	...	...

Numerous theories and experimental methods, based on different criteria, have been developed to determine the susceptibility to solidification cracking. A critical review of existing theories and their applicability to solidification cracking, such as the shrinkage-brittleness theory [40], the technological strength theory [41], and the rate of feeding - rate of shrinkage theory [42], can be found in [43]. Nevertheless, most theories and experimental

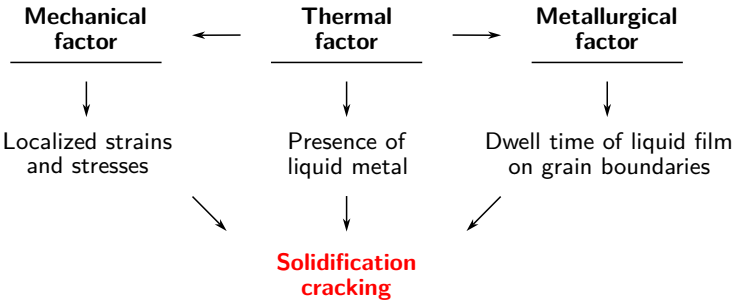

Figure 2.2: Schematic indicating the relationships between the dominant factors and the critical conditions determining the susceptibility to solidification cracking

tests do not focus on the interactions between the dominant factors and their combined influence on the susceptibility to solidification cracking. Instead, these primarily concentrate on the influence from a single factor or sub-factor. For example, attempts are often made to classify materials experimentally as resistant or susceptible to cracking based on mechanical or metallurgical aspects. The influence of the mechanical response on the susceptibility to cracking of the joined components is usually experimentally studied by self-restraint or externally loaded cracking tests [44]. These tests are designed to determine critical values for the strain or the strain rates at which cracking occurs. Moreover, in practice, certain materials, such as cast steel, high-alloy steels, nickel-based alloys, and aluminum alloys, have proven particularly susceptible to cracking due to the influence of various metallurgical sub-factors [45–47]. The lattice type in which the weld metal solidifies is one of these sub-factors leading to lower cracking resistivity. Materials solidifying in a face-centered cubic (FCC) lattice are considered susceptible to solidification cracking due to the low diffusion rate and low solubility of liquating elements such as S and P [14, 48]. Another factor contributing to the higher susceptibility of the FCC lattice to cracking is the thermal shrinkage that occurs in the weld metal during solidification. The FCC lattice has lower thermal conductivity compared to the body-centered cubic (BCC) lattice, which results in higher peak temperatures, and thus higher temperature gradients. Additionally, it is more densely packed than the BCC lattice, therefore having a higher thermal expansion coefficient ($23 \times 10^{-6}\,\mathrm{K}^{-1}$ for FCC and $16 \times 10^{-6}\,\mathrm{K}^{-1}$ for BCC in the temperature range between 1392 °C and 1539 °C [49]). Consequently, the higher temperature gradient and thermal expansion coefficient of the FCC lattice lead to a stronger shrinkage force, and hence a higher risk of solidification cracking [14, 50]. Furthermore, the dependence of the cracking susceptibility on the substructures forming inside the grains, such as planar, cellular, or dendritic, as well as on their grain size, are often considered relevant. The type and size of the crystal substructure are determined by both the chemical composition and the local cooling rate. According to [51], when the weld metal solidifies primarily in a cellular substructure, the tendency to solidification cracking increases compared to the case of a

primarily dendritic substructure. In [52], the influence of grain size on cracking resistivity has been studied, showing that grain refinement can be beneficial for crack prevention.

Despite the extensive knowledge on the influence of mechanical and metallurgical factors on the formation of solidification cracks, cracks can form even in cases contrary to the general understanding. For example, in [37], the relationship between the degree of restraint and the occurrence of solidification cracking was studied. The authors found that the susceptibility to cracking can be reduced or completely avoided by artificially increasing the degree of restraint in the welded structure. Furthermore, various nickel-based alloys, whose weld metal solidifies completely in an FCC lattice, are classified as crack-resistant [53]. On the contrary, low-alloyed and unalloyed materials, whose weld metal solidifies completely in a BCC lattice, have been found to be susceptible to solidification cracking, depending on the wall thickness of the components and the welding process. Drawing upon the comprehensive literature review on the relationships between the dominant factors and the critical conditions determining cracking susceptibility, it can be suggested that the influencing factors for the formation of solidification cracks can only be used as an indirect, and not as a direct measure of the cracking susceptibility. The interrelationships between solidification cracking, metallurgical mechanisms, and mechanical mechanisms indicate that the formation of solidification cracks is not governed by a single mechanism or its corresponding sub-factors. Instead, the various influences from the three dominant factors must be related to the particular welding application to allow for a comprehensive study of their interactions. Only then could the mechanisms causing solidification cracking be clarified for the specific case.

2.3 Bulging Region in Deep Penetration Laser Beam Welding

Experimental Evidence of the Bulging-Cracking Relationship

From the literature review on solidification cracking susceptibility in deep penetration LBW presented in Section 2.2 follows that the cracking behavior of the joined components is controlled by three dominant factors and their corresponding interactions [5]. The dominant thermal, mechanical, and metallurgical factors are, however, strongly dependent on the weld pool geometry and vice versa [6, 7]. The weld pool geometry, on the other hand, has long been known to be decisive for the formation of material defects during the solidification stage of the welding process, particularly regarding the occurrence of solidification cracking in deep penetration welding [6, 24, 54].

The influence of the weld pool geometry on the susceptibility to solidification cracking in deep penetration EBW of thick steel sheets has been researched since the late 1970s. In [8], the relationship between the weld pool geometry and solidification cracking was experimentally studied for different welding conditions. According to the findings, a focal position on or above the top surface of the joined steel sheets leads to a widening and elongation of the keyhole geometry at approximately one-third to one-half of the penetration depth. Consequently, the liquid metal behind the keyhole is pushed backward, i.e., in the opposite direction to the welding direction, forming a region of geometrical particularity, nowadays often referred to as a bulging region, see Figure 2.3. The authors discovered

that the size of the bulging region is decisive for the formation of weld imperfections. A large bulging region was shown to lead to the separation of the column of liquid metal into roughly two parts, which solidify independently, forming a void in-between. On the other hand, a bulging region of a smaller size was found to significantly increase the susceptibility to centerline solidification cracking. The study presented in [8] has been further extended by a series of experiments published in [10–12]. In these works, the influence of the bulging region on the occurrence of cracking in deep penetration EBW of thick unalloyed steel sheets has been studied by adding pure Ni (Nickel) at different depths along the weld trajectory before the welding process. Subsequently, the authors used the segregation patterns of the Ni element remaining in the weld metal to identify the geometry of the FZ in the longitudinal section and several metallographic cross-sections. Based on the experimental observations, it was suggested that the liquid metal in the bulging region experiences a local delay in solidification. Moreover, it was shown that due to its larger dimensions compared to the regions located above and below it, the bulging region solidifies at a later stage. Therefore, the liquid metal in the bulging region becomes isolated, i.e., surrounded by solid, which results in an increased formation of centerline cracks therein, as indicated in Figure 2.3.

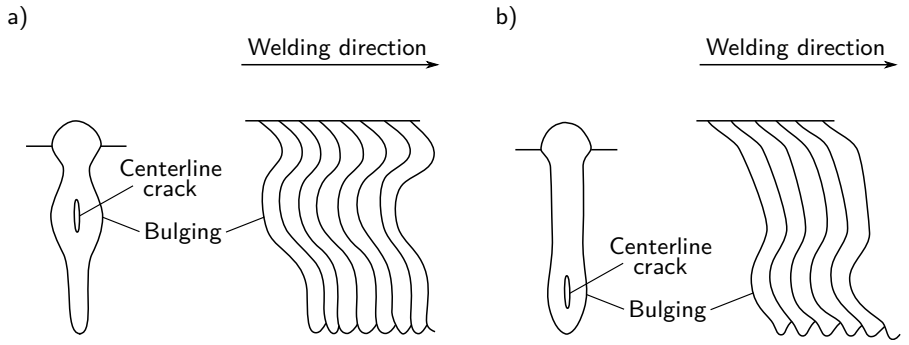

Figure 2.3: Solidification patterns indicating the occurrence of centerline cracking in the bulging region due to a local solidification delay, according to [8, 10, 11]

The correlation between the bulging region and the formation of solidification cracks has been confirmed by experimental studies on high power LBW of thick unalloyed steel sheets as well [13, 14]. Thereby, the focus was on the widening of the weld pool geometry in the transversal direction and its hypothetical influence on the cracking susceptibility of the welded components. Similar to the observations made on electron beam welded steel sheets, the locations of the bulging region and the solidification cracks coincide. Moreover, nearly all cracks found in the FZ were centerline cracks located approximately in the middle of the bulging region. In [13], the author analyzed the solidification sequence of the liquid metal in the cross-section and hypothesized that the cause of the centerline cracks may be the longer transversal distance between the seam flanks in the bulging region. This

hypothesis was based on two considerations. A closer look at Figure 2.4 shows that the crystals start growing from the cold parallel seam flanks into the weld pool in opposite directions to each other. As the crystals continue growing, the first dendrite tips coalesce where the distance between the seam flanks is smallest. Considering that the cooling rates in the bulging region are higher than the growth rate of the crystals, the dendrite tips at its center may not coalesce at all. This could result in a void being left in the middle of the bulging region, potentially leading to the formation or initiation of a crack. On the other hand, due to the longer distance between the seam flanks, the crystals growing in the bulging region will need a longer time to reach the weld centerline. Considering the extended solidification time in the bulging region, it can be expected that the liquid metal therein will be subjected to higher tensile forces induced by its shrinkage and the resistance of the surrounding solid metal [14]. As a result, the solidification fronts may be pulled apart from each other at the final solidification stage, leading to the formation of a centerline crack, see Figure 2.4. Both considerations are supported by recent SEM observations of the fracture surfaces of centerline cracks, as described in Section 2.2. This suggests that there may be more than one mechanism involved in the formation of centerline cracks in deep penetration LBW. Furthermore, in [54], an effort was made to evaluate the extent of the bulging region in the weld cross-section and quantify its influence on solidification cracking in hybrid laser-gas metal arc welding of thick steel sheets. There, a bulging widening angle, defined as the angle between the narrowest and widest cross-sectional dimensions within the bulging region, was used as a measure of the extent of the bulging region. The authors reported conflicting results regarding the influence of the welding speed and the laser beam energy on the occurrence of solidification cracking. However, the obtained results indicated that solidification cracking strongly depends on the geometries of the keyhole and the weld pool, and thus on the dimensions of the bulging region. Moreover, the observed solidification

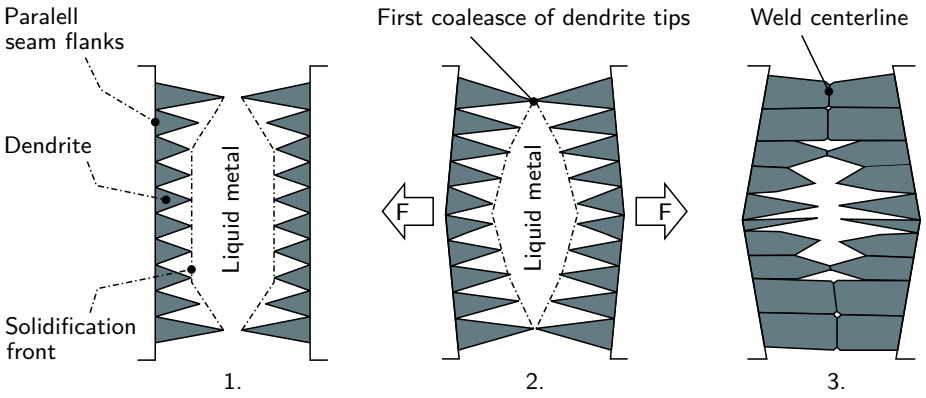

Figure 2.4: Hypothetical formation of a centerline solidification crack in deep penetration laser beam welding of low-alloyed and unalloyed steel sheets, according to [14]

cracks were always associated with the presence of a widened FZ around the crack location, showing a tendency of increasing crack formation with increasing bulging widening angle. Nonetheless, there is no known relationship between the elongation of the bulging region or its shape and the cracking susceptibility of the joined components.

Theoretical Studies on the Bulging Region

The observation and study of the bulging region and its influence on the formation of solidification cracks during deep penetration EBW or LBW represent a highly challenging task due to the optical inaccessibility of the welding process and the complex technical equipment required for the recording. For this reason, in all studies mentioned in the paragraphs above, the bulging region has only been observed in metallographic macro sections rather than in real-time. Despite this fact, a bulging region appears in several sophisticated numerical simulations of the weld pool geometry, even though not being the object of study [55–57], [AJ16]. In reference to the available literature on the occurrence of a bulging region in EBW, the bulging region is considered to be the consequence of a strong metallic vapor flow induced on the front keyhole wall [8, 12]. Nevertheless, recent research work of the author on the nature of the bulging region, and in particular, on its temporal evolution in deep partial penetration high power LBW of thick unalloyed steel sheets, suggests a slightly different formation mechanism [AJ23-AJ25]. In these studies, a multiphysics numerical model allowing to consider the keyhole dynamics and its influence on the liquid metal, was developed and used to estimate the three-dimensional weld pool geometry and the fluid flow therein. Based on the numerically predicted flow patterns, the weld pool was characterized by two regions, a top and a bottom region, which dimensions and shape were determined by two main vortexes, independent of the formation of a bulging region, see Figure 2.5. The vortex in the top region is due to the combined action of the Marangoni force, the recoil force, and the metallic vapor flow inside the keyhole. This vortex accelerates from the keyhole rear surface along the top surface of the weld pool, transporting the hotter liquid metal away from the keyhole. Subsequently, when the liquid metal reaches the weld pool rear boundary, the flow turns its direction to the welding direction, bringing the liquid metal back to the vicinity of the keyhole, and thus ensuring mass conservation. The second vortex acts in the bottom region and is mainly caused by the strong recoil force of evaporation, which pushes the liquid metal at the keyhole bottom backward, i.e., in the opposite direction to the welding direction. As a result, the liquid metal flows upward along the solidification front and changes its direction to the welding direction once it reaches the top region. As the liquid metal in the top and bottom regions of the weld pool flows along the solidification front, its temperature continuously decreases. Therefore, at the moment when the two vortexes meet, and their flow directions turn into the welding direction, the liquid metal solidifies, separating the top and bottom regions of the weld pool by forming a narrow channel between them, see Figure 2.5. Consequently, more liquid metal accumulates in the bottom region, leading to the formation of a bulging region. Furthermore, it was found that the narrow and bulging regions form simultaneously, approximately when the weld pool geometry reaches a quasi-steady state. The numerical results also indicated that both

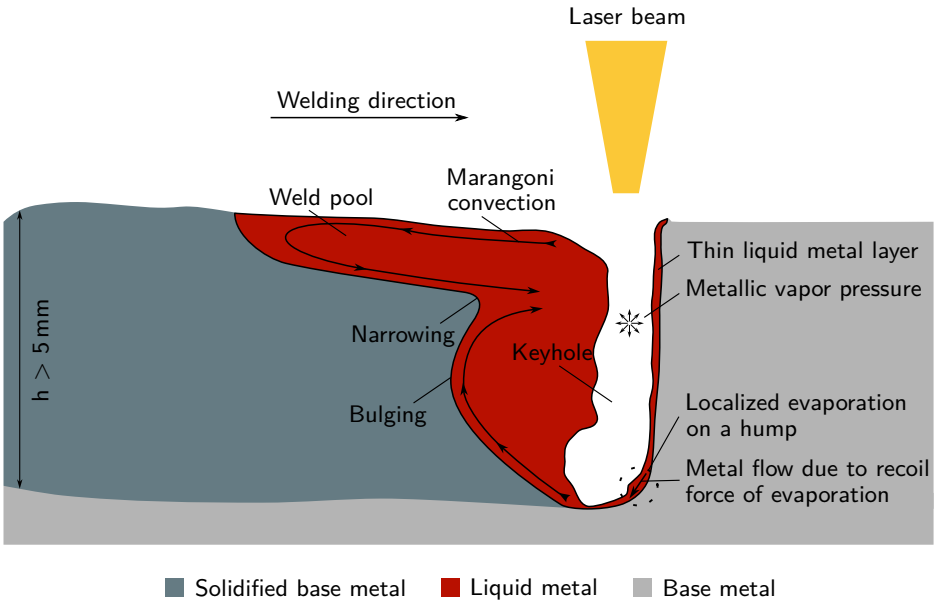

Figure 2.5: Schematic of the formation of a bulging region in deep partial penetration laser beam welding, according to [AJ23-AJ25]

regions occur transiently and that the formation of a bulging region depends strongly on the penetration depth, having a transition threshold from a slight bulging to a fully developed bulging region at penetration depths between 6 mm and 9 mm [AJ23-AJ25]. A narrow and a bulging region were as well observed in recent numerical simulations of deep partial penetration wire-feed LBW [AJ26-AJ28]. In these studies, it was shown that the formation of these two regions significantly deteriorates the downward transfer of liquid metal from the top to the bottom region of the weld pool. This resulted in a non-homogeneous distribution of the alloying elements fed into the weld pool during the wire-feed LBW process, and hence to significant differences in the mechanical properties of the final weld along its thickness.

Concerning the studies on the bulging region and the bulging-cracking relationship mentioned above, both the experimental and the theoretical research works seem to be limited to deep partial penetration welding. Moreover, most attempts to link the bulging region to solidification cracking focus on studying one of the three dominant factors controlling the cracking behavior, e.g., the solidification range or the critical strains and stresses, see Section 2.2, and do not consider their interrelationships, i.e., their combined influence on the cracking behavior. In addition, only the width of the bulging region is regarded as relevant, neglecting the influence of its length or shape on the weld microstructure, and therefore on the local susceptibility to solidification cracking.

2.4 Welding Simulation

The aforementioned large number of influencing parameters and physical effects involved in the formation of solidification cracks in deep penetration welding, as well as the poor optical accessibility of the welding process, do not allow for building up a sufficient experimental database and expertise needed to deepen the understanding of the influence of the bulging region on the cracking susceptibility, see Sections 2.1 to 2.3. Therefore, mathematical modeling, including functional-analytical methods, e.g., the method of sources or the method of separation of variables, and numerical methods, e.g., the finite element method or the finite volume method, has become a crucial part to the solution of such technically demanding joining tasks. Compared to the experimental approach, a computer-aided study offers several advantages in understanding the fundamentals related to welding phenomena. Specifically, it allows for a significant gain in information by predicting three-dimensional transient field quantities, which can be challenging to access experimentally in some cases or entirely inaccessible in others. Examples include temperature and velocity distributions inside the weld pool or residual stresses within welded structures with high wall-thicknesses. Moreover, synthetic modeling provides the flexibility to selectively add or omit physical effects, thereby enabling the isolation of the action of a single effect or a combination of effects on the computational results. This facilitates the analysis of their interactions and the weighting of their influence on the object of study. Hence, mathematical modeling techniques offer great potential to study the relationship between the bulging region and the local susceptibility to solidification cracking.

2.4.1 Classification of Welding Simulation

As described in Section 2.1, the physics behind the deep penetration welding process is very complicated as it involves several strongly coupled and highly nonlinear interactions between the processed material and the energy source, the vapor phase, the weld pool, and the solid metal. Accordingly, several complex physical effects such as energy absorption, melting, vaporization of liquid metal, recondensation of metallic vapor, solidification, thermo-capillary convection, heat conduction in the liquid and solid, distortion, and heat transfer by radiation and evaporation have to be considered for its sufficient mathematical description. Despite the advances in the development and optimization of solution algorithms and the rising computer performance, the comprehensive coupled consideration of all physical aspects governing the deep penetration welding process remains a major difficulty. Moreover, the mathematical description of the involved phenomena and their interrelationships represents a rather challenging task. Therefore, the research in welding simulation has focused on decoupling the welding process into physical domains, each considering different time and size scales, depending on the application and objectives.

According to [58], there are three main physical domains, namely the domains of process, mechanical, and material simulations, see Figure 2.6. Thereby, the process simulation aims at the detailed modeling of the three-dimensional weld pool geometry and the flow dynamics of the liquid metal therein by considering various dynamic interactions such as these between

the energy source and the processed material. It enables, e.g., the prediction of the seam width, the penetration depth, the weld reinforcement, the weld pool length, the process efficiency, and the process stability. The material simulation, on the other hand, is concerned with the thermo-metallurgical effects. It is used to estimate the microstructure state in the FZ and the HAZ, the resulting hardness of the weld metal, and the susceptibility to cold and hot cracking. In recent times also the prediction of thermo-physical material properties, e.g., heat capacity and heat conductivity, and thermo-mechanical material properties, e.g., stress-strain curves, Young's modulus, and Poisson's ratio, became an essential part of the material simulation. In contrast to the material simulation, the structure simulation deals with the thermo-mechanical effects of welding. These include the prediction of welding distortions and residual stresses as well as the estimation of their influence on the stiffness of the welded structure, the strength of the weld metal in the FZ, and the material in the HAZ.

As described above, the decoupling approach allows studying the aspects of each physical domain independent of the consideration of the other domains. However, theoretically, this

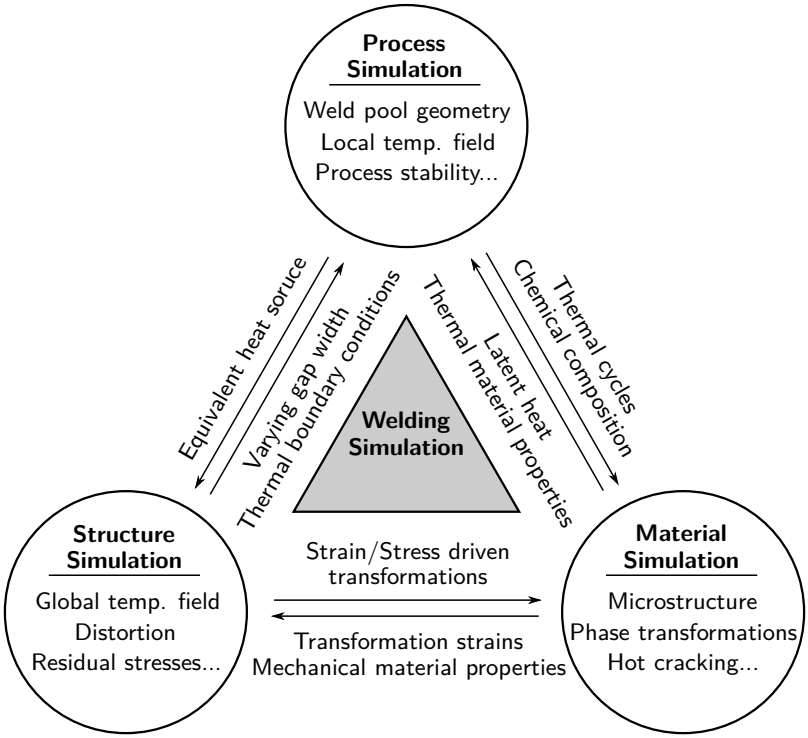

Figure 2.6: Coupling of the physical domains in welding simulation, according to [58]

approach also allows to account for the influence from one domain on another by using input and output quantities, as schematically indicated in Figure 2.6. The influence, e.g., of the process simulation on the structure simulation, can be modeled by transferring an equivalent heat source (EHS) from the process simulation to the structure simulation. Conversely, the influence of the structure on the process simulation, can be considered by transferring the varying gap width and the thermal boundary conditions. Nonetheless, even the one-way coupling of the physical domains brings significant complexity to the modeling task, and is therefore usually not accounted for in welding simulation.

2.4.2 Mathematical Modeling of the Bulging-Cracking Relationship

With regard to Sections 2.2, 2.3 and 2.4.1, the physical domains involved in the mathematical analysis of the relationship between the bulging region and the local susceptibility to solidification cracking can be identified. A closer look at the interrelationships between the critical conditions and the dominant factors controlling the local susceptibility to solidification cracking, see Figure 2.2, and the main physical domains of welding simulation, see Figure 2.6, reveals that the study of the bulging-cracking relationship requires information from all three physical domains. Thereby, the process simulation enables the estimation of the influence of the bulging region on the thermal factor by providing information about the liquid metal regions present at the final solidification stage. Furthermore, the material simulation allows to compute the dwell time of the liquid film residing on the grain boundaries, and thus assess the influence of the bulging region on the metallurgical factor. Finally, the structure simulation can be used to estimate the influence of the bulging region on the mechanical factor by analyzing the predicted strains and stresses in the critical regions.

In the following, an overview of the mathematical approaches needed for the study of the bulging-cracking relationship in deep penetration LBW is given, focusing on the mathematical models and methods with relevant capabilities for the solution of this task.

- Process simulation

To study the influence of the bulging region on the thermal factor in LBW, the three-dimensional weld pool geometry, including the bulging region, must be computed by a process simulation as this determines the liquid metal distribution during solidification. A closer look at the physical phenomena governing the formation of the keyhole and the weld pool in deep penetration welding, described in Section 2.1, indicates that the process simulation can be divided into two parts. The first part describes the interactions of the laser beam with the processed material, and the second part focuses on the heat and mass transfer in the liquid, solid, and vapor phases. A mathematical description of the governing conservation equations of mass, energy, and momentum can be found in [59]. As the fundamentals of process simulation in welding date back to the early 1940s, nowadays, many different analytical and numerical models dealing with the prediction of the weld pool geometry are available in the literature. An overview of developed analytical and numerical models can be found in [58, 60]. The first contributions in that field of research

were analytical [61] and entirely based on the theory of heat conduction in solids [62]. In this approach, the linear partial differential equation (PDE) of heat conduction is solved considering a given energy input represented by a concentrated or non-concentrated energy distribution, e.g., a point, line, or cylindrical heat source [39], to provide information about the global temperature distribution in the joined components. However, since the convection of the liquid metal in the weld pool was not explicitly calculated, and other significant effects such as the latent heat of melting and solidification [39], or the temperature dependence of the material properties [63, 64] were not accounted for, these models fail to adequately predict the real weld pool geometry, even after intensive calibration of the applied heat source [65].

The inability of the analytical models to describe the weld pool geometry with sufficient accuracy, especially in three dimensions, led to the development of numerical models, which allow for the consideration of convective heat and mass transfer in the liquid phase. The first phenomenological numerical models were two-dimensional and accounted for the flow of liquid metal around a fixed keyhole of a circular shape [66, 67]. Later, this concept was extended to three-dimensional models, which included the most important physical effects such as the relative movement of the keyhole to the solid, the thermo-capillary convection, the latent heat of solidification, and the temperature-dependent material properties [68, 69]. Typically, in these models, the liquid metal is assumed to be an isotropic Newtonian and incompressible fluid, and the flow regime laminar [60]. However, it has been shown that for specific applications [70, 71], including a turbulence model, such as the standard $\kappa - \epsilon$ model, can significantly improve the accuracy of the computational results in the high-velocity regions, e.g., around the keyhole or near the top and bottom surfaces of the weld pool [72]. Moreover, these models use the keyhole geometry as an EHS. This means that its surface temperature is set to the evaporation temperature of the material used based on the assumption that the temperature inside the keyhole should be at least equal to or higher than the evaporation temperature to vaporize the liquid metal [73]. Thereby, the keyhole is often assumed to have a cylindrical or conical shape, whereas in some cases, its geometry is estimated by computations based on the energy balance on the keyhole surface [18, 74]. When assuming the keyhole geometry, the model has to be calibrated so that the energy absorbed by the processed material lies in a plausible range of 65% to 85% of the initial laser power [75]. Furthermore, the deformation of the free surfaces is not taken into account, meaning that the effects caused by keyhole oscillations are neglected. Nonetheless, the influence of the focal position and the multiple reflections on the energy absorption, and thus on the recoil pressure can be considered phenomenologically by adapting the cross-sectional area of the fixed keyhole accordingly. In general, the fixed keyhole models have proven to be a practical tool for computing heat and mass transfer in deep penetration LBW, enabling the three-dimensional weld pool geometry estimation with sufficient accuracy and at a low computational cost.

In recent times, process simulation has become an intensively growing field of study due to the possibilities of using high-performance computing (HPC) systems and software design [76]. Modern numerical models aim not at the phenomenological description of the process but rather at a self-consistent formulation of the relevant physical phenomena.

Hence, in addition to the heat and mass transfer in the liquid, solid, and vapor phases, self-consistent models have to account for the interactions between the laser beam and the processed material, including the attenuation of the laser beam by the metallic vapor. Typically, different approaches are utilized to consider the laser-beam material interactions dependent on the application and objectives [60]. In a self-consistent approach, e.g., an electromagnetic simulation of the laser beam propagation is performed, which requires the solution of Maxwell's equations [77]. This approach is strongly limited by the required mesh size, and therefore typically formulated in two dimensions. Thereby, the maximum mesh size has to be smaller than the beam wavelength, which in the case of solid-state lasers is around 1 µm. This requirement results in a considerable number of elements and correspondingly long computational times, reaching up to several days even on HPC systems. For this reason, an alternative consideration of the interactions between the laser beam and the processed material by a ray-tracing method is often used by researchers [59].Thereby, the laser beam is divided into several sub-rays by discretizing the laser spot in the focal plane. Each sub-ray receives its location-dependent energy density, which, when multiplied by the surface area of the corresponding sub-region, yields the energy carried by the sub-ray. Subsequently, the three-dimensional energy distribution on the vapor-liquid interface is obtained by accounting for the multiple reflections of the sub-rays and their absorption on it. Although the ray-tracing method reduces the computational intensity compared to the models considering the real propagation of the laser beam, the typical computational times for approximately 1 s to 2 s of the real process remain in the order of hundreds of hours.

As described above, two types of weld pool models, namely phenomenological and self-consistent models, can be employed to study the influence of the bulging region on the thermal factor and, subsequently, the relationship between bulging and cracking in deep penetration LBW. However, the latter takes considerable time to be developed appropriately and requires high computational power. Moreover, as mentioned in Section 2.3, while the formation of the bulging region in deep partial penetration LBW has been recently elucidated by models utilizing the ray-tracing approach, there is currently no comprehensive model that deals with and explains the formation of the bulging region in complete penetration high power LBW. Therefore, a phenomenological model allowing for the reproduction of the bulging region is considered well-suited to study its influence on the dominant factors controlling the susceptibility to solidification cracking.

- Coupling of process and material simulation

Following the relationships between the dominant factors and the critical conditions controlling the formation of solidification cracks, illustrated in Figure 2.2, it becomes clear that the influence of the bulging region on the metallurgical factor can be estimated by evaluating the second critical condition, i.e., the dwell time of the liquid film residing on the grain boundaries in the liquid metal regions identified as critical in terms of the thermal factor. Therefore, the thermo-metallurgical interactions need to be studied, which requires the coupling of the process and material simulation, as illustrated in Figure 2.6. To obtain the dwell time of the liquid film, the solidification process of the weld metal has to be mathematically described

and subsequently analyzed [78]. Even though mathematical methods have been used to model the solidification process of the weld metal for more than 50 years [79, 80], this task remains extremely complicated. This is due to the complexity of the solidification process, which involves various factors, including the weld pool geometry, the local temperature field, and the chemical composition of the material used. An overview of established techniques in metallurgical modeling, such as the phase-field method, the cellular automaton model, and the Monte Carlo model, can be found in [81–83]. In the case of a melt of impure metal of uniform composition, the solidification process is governed by the processes of diffusion and segregation [84, 85]. As a result of segregation, impurities such as S and P accumulate ahead of the solidification front during crystal growth, leading to their non-uniform distribution in the weld metal. This chemical inhomogeneity causes local variations in the solidus temperature, being lower in regions with increased concentration of liquating elements [39, 86]. Consequently, in these regions, the dwell time of the liquid film increases, elevating the susceptibility to solidification cracking [14, 26].

It is well-known that the local solidus temperature is strongly dependent on both the peak value and the width of the region of accumulated impurities ahead of the solidification front [33, 38]. Therefore, its quantitative prediction requires the solution of the non-homogeneous diffusion problem by considering the difference in the solubility of impurities in the liquid and solid phases. The solution of the non-homogeneous diffusion problem, however, depends on the main solidification parameters controlling the degree of inhomogeneity, namely the crystal axis, the growth rate, and the corresponding cross-sectional area of the crystal [33, 39]. On the other hand, these parameters depend on the movement of the isothermal surface of the solidus temperature, the crystallographic orientation, and the competitive grain growth during the solidification process. However, the consideration of all dependencies makes the problem rather unfeasible to solve, especially in three dimensions, and therefore such complex models are often limited to two-dimensional computational domains of microscopic sizes [87]. In more practical approaches, the main solidification parameters are computed by neglecting the change of the weld pool geometry due to the varying solidus temperature and the effects of crystallographic orientation and competitive growth. Instead, the process and material simulation are coupled using the experimentally measured or numerically determined weld pool geometry [79]. This simplification of the solidification problem allows to predict the solidification parameters within the entire FZ. Once determined, these can be analyzed to provide a qualitative estimation of the local dwell time of the liquid film. Referring to Section 2.3, the weld pool geometry has a strong influence on the dominant factors controlling the cracking behavior of the welded components. Therefore, when the simpler approach is utilized, the weld pool geometry has to be mathematically described with a sufficient accuracy to account for the influence of any geometrical particularities, such as the bulging region, on the solidification parameters. Approximation techniques developed to describe the three-dimensional weld pool geometry in partial penetration welding have been proposed in [79] and more recently in [88]. Nonetheless, these techniques are limited to simpler weld pool geometries and can not be applied for reconstructing the complex three-dimensional weld pool geometry, including the bulging region.

- Coupling of process and structure simulation

The coupling of the process and structure simulations aims to estimate the influence of the bulging region on the mechanical factor, see Figure 2.2, and, subsequently, on the susceptibility of the welded components to cracking. Therefore, the third critical condition, i.e., the local rise of strains and stresses in the regions identified as critical in terms of the thermal and metallurgical factors, has to be evaluated. To determine the influence of the bulging region on the strains and stresses in these critical regions, it is first necessary to estimate its effect on the transient global temperature field. An essential part of achieving this is the adequate representation of the welding conditions in the formulation of the heat conduction problem in welding. Typically, the welding conditions are expressed in terms of either a heat input or a temperature [39]. Due to its simplicity and flexibility, the first approach has been widely utilized in welding simulation. Nowadays, a variety of heat source models can be found in the literature, reaching from simple concentrated and uniformly distributed, e.g., a point, line or plane heat source [61], over concentrated and non-uniformly distributed [89], to more sophisticated non-concentrated uniform as well as non-concentrated and non-uniform heat sources, e.g., a Gaussian, exponential, or parabolic distribution over a surface, e.g., disc, cylinder, cone or strip [90], or a volume e.g., cylinder or semi-infinite body [91–93]. Nonetheless, this modeling approach requires an appropriate selection and intensive calibration of the heat source model [39, 91], which does not allow to accurately account for the effect of the bulging region on the temperature evolution in the welded structure, and thus on the mechanical factor.

The second approach is based on the concept of the EHS. This approach is much more compact and straightforward in terms of information technology as it does not require the representation of the net absorbed power and its distribution. Instead, the temperatures are prescribed in fixed points, e.g., on a cylindrical or conical surface, as done in the fixed keyhole modeling approach presented above. As depicted in Figure 2.6, the EHS represents the input quantity transferred from the process to the structure simulation. Thereby, the information required for the computation of the temperature distribution is entirely contained in the isothermal surface of the solidus temperature, which represents the three-dimensional weld pool geometry [94]. Hence, to determine the transient global temperature distribution in the solid phase outside the weld pool, it is sufficient to specify the movement of the weld pool geometry through the welded components in time and space and prescribe the solidus temperature to all points located on or within the weld pool. The first applications of the EHS technique can be found in research works from the early 1960s, where the finite difference method has been utilized to solve the two-dimensional heat conduction problem [94]. Moreover, the EHS technique has been implemented in the commercial welding and assembly simulation software Sysweld® with the limitation of providing only the isothermal contour from metallographic cross-sections. In [95], the authors made use of this feature and extended it to consider several such contours. This approach enabled the application of the numerically predicted weld pool geometry as an EHS. Nevertheless, the capability of this approach to reproduce complex three-dimensional weld pool geometries is limited in accuracy. More recently, the EHS technique has been combined with a moving mesh approach [AJ1].

The mesh used to compute the weld pool geometry was part of the mesh utilized to compute the global temperature distribution. This allowed for keeping the predicted temperature of each point of the three-dimensional weld pool while moving along the welding trajectory. One advantage of this approach is the more accurate prediction of the temperature field after the energy source is turned off. In this case, the energy in the weld pool is slightly higher than when the solidus temperature is prescribed to all points. Nonetheless, the moving mesh approach has limited applicability due to the deformation of the mesh and can not be utilized when complex welding trajectories are studied. Furthermore, an EHS has been defined by using the boundary element method [AJ9]. In this study, analytical point heat sources have been defined on the weld pool surface, and their power densities have been obtained by inverse modeling so that the computed temperature on the surface equals the solidus temperature of the material used. Once the power densities of the heat sources are computed, the temperatures outside the weld pool can be determined by summing the contributions of each heat source. However, due to the application of analytical heat sources, this approach does not allow to consider the temperature dependence of the material properties. Moreover, the analytical heat sources have the disadvantage of providing the temperature only for single points. Hence, the global temperature field has to be obtained by first calculating the temperature at several locations and subsequently interpolating between these. To the best of the author's knowledge, no model available in the literature has the capability of describing complex three-dimensional weld pool geometries, including geometrical particularities such as the bulging region, with sufficient detail and accuracy.

According to experimental and numerical studies published in [96, 97], the highly concentrated energy input used in deep penetration welding, see Section 2.1, results in non-uniform heating and subsequent rapid cooling of the processed material. Thereby, the material temperature increases up to temperatures even higher than the evaporation temperature of the material and cools down with typical cooling rates in the order of $10^3\,\mathrm{K\,s^{-1}}$ as the absorbed energy is transferred to the bulk of the joined components by conduction and convection of heat and mass [73]. Consequently, different regions of the processed material thermally expand and contract simultaneously, which generates temporal and residual stresses in the weld metal, and leads to the deformation of the final part [98]. However, it is well-known that the effect of material deformation on the temperature field is negligible. Thus, the heat conduction computation is usually decoupled from the structure simulation [99, 100]. Instead, only the influence of the temperature field on the mechanical response of the material is accounted for by applying the predicted global temperature distribution as a transient thermal load. A detailed description of the general procedure of the structure simulation can be found in [101, 102]. Many significant contributions in the field of numerical modeling of residual stresses and distortion have been summarized in [99, 103]. Studies on the influence of several factors, e.g., the material model, the welding sequence, the clamping, and the initial condition of the joined components in terms of stress state, on the accuracy of the predicted strains and stresses are published in [104–106]. The modeling of the material behavior, however, i.e., consideration of temperature-dependent material properties, strain hardening, and solid-state phase transformations (SSPTs), is decisive for the accuracy of the structure simulation [102, 106].

As described in Sections 2.2 and 2.3, centerline solidification cracking represent one of the most critical material failures in deep penetration LBW of unalloyed steel sheets, especially with regard on its frequent occurrence. According to the present state of the art, one formation mechanism of centerline solidification cracking is based on the rupture of the liquid film residing on the grain boundaries by the rising strains and stresses at the final solidification stage. In this case, it is assumed that centerline solidification cracking is caused by the horizontal strains and stresses acting in opposite directions to the growing direction of the crystals, thus pulling the solidification fronts apart from each other. Therefore, the study of the influence of the bulging region on the mechanical factor can be performed in two dimensions, as done in [6]. The mechanical model presented in that work is based on a plane strain formulation. This means that a long and straight weld seam was assumed, allowing to neglect all out-of-plane strain components. Hence, the only quantity not provided by the model but assumed to be zero, is the strain component in the welding direction, which is not considered to influence the susceptibility to centerline solidification cracking. In addition, the two-dimensional model enables finer discretization of both spatial and temporal domains, resulting in higher accuracy of the numerically predicted strains and stresses.

2.5 State of the Art Summary and Objectives of the Work

Numerous theories and experimental methods have been published over the past decades, contributing to the understanding of the mechanisms involved in the formation of solidification cracks in deep penetration welding. Nevertheless, due to the highly complex nature of this material failure, none of these have proven to describe or predict the occurrence of cracking adequately. Most theories generally focus on isolated factors, thus addressing the problem from a single aspect. The detailed review of the available literature, however, suggests that the susceptibility to weld solidification cracking is mainly determined by the thermo-metallurgical and thermo-mechanical interactions, and thus involves three dominant factors, namely the thermal, metallurgical, and mechanical factors. Thereby, the thermal factor determines the distribution of liquid metal at the final solidification stage. The metallurgical factor governs the dwell time of the liquid film residing on the grain boundaries, and the mechanical factor controls the local and global strains and stresses, which may lead to the rupture of the liquid film in the critical regions. The three dominant factors are strongly coupled and depend on the weld pool geometry, which is long known to be decisive for the formation of defects in laser beam welded steel sheets. The relationship between the weld pool geometry and the susceptibility to solidification cracking has been studied experimentally in early research on EBW of thick low-alloyed and unalloyed steel sheets from the 1980s [8, 10–12]. A local elongation and widening of the weld pool, called a bulging region, was found to increase the susceptibility to centerline solidification cracking. Similar research results have been published on LBW of thick unalloyed steel sheets. In these studies, the strong correlation between the dimensions and the shape of the bulging region and the occurrence of centerline solidification cracking has been confirmed [6, 13, 14]. Nonetheless, due to the optical inaccessibility of the LBW process, the bulging region was not observed during the

experiments but rather identified in metallographic macro sections. Moreover, none of the published studies seem to address the significant and yet poorly understood influence of the bulging region on the three dominant factors, and thus on the formation of solidification cracks. Therefore, in present time, a fundamental need arises to deepen the knowledge on the relationship between the bulging region and the formation of centerline solidification cracks in deep penetration LBW.

The main objective of the present work is to perform a methodical experimental and theoretical analysis of the influence of the bulging region on the local susceptibility to centerline solidification cracking in LBW of thick unalloyed steel sheets. According to the current state of the art, this can be achieved by estimating the dependence of the three dominant factors controlling the cracking behavior on the bulging region. Due to the complexity of the LBW process and the mechanisms involved in the formation of solidification cracks, it is not possible to determine these dependencies experimentally. Nonetheless, the problem can be tackled by applying analytical and numerical methods, which are not limited by the technical equipment or the optical inaccessibility of the welding process. Therefore, first, the occurrence and conditions under which a bulging region forms during the LBW process have to be assessed experimentally. Furthermore, a weld pool geometry, including a bulging region, as experimentally observed, has to be phenomenologically reproduced by a numerical model. Once predicted, the weld pool geometry can be directly used to assess the dependence of the thermal factor on the bulging region, as it allows to study the change of the liquid metal distribution with time. In addition, the weld pool geometry can be utilized to estimate the influence of the bulging region on the metallurgical factor, i.e., the decrease in the local solidus temperature caused by chemical inhomogeneity and the corresponding increase in the dwell time of the liquid film. For this purpose, the main solidification parameters governed by the weld pool geometry, namely, the crystal axis, the growth rate, and the corresponding cross-sectional area of the columnar crystal, have to be determined. Finally, the numerically reproduced weld pool geometry can be applied as an EHS, thus allowing to consider the effect of the bulging region on the temperature history. Subsequently, the influence of the bulging region on the mechanical factor can be estimated by using the obtained temperature history as the thermal load inducing the global and local strains and stresses in a structure simulation.

To summarize, the particular objectives of the present work are the following:

- Conduct an experimental study to observe the geometrical characteristics of the weld pool geometry during the LBW process.
- Develop, based on models and submodels published in the literature, a comprehensive numerical model for the calculation of the local heat and mass transfer, allowing to phenomenologically reproduce the experimentally observed weld pool geometry, including the bulging region.
- Use the numerically reproduced weld pool geometry to determine the liquid metal distribution at the final solidification stage and estimate, based on this, the influence of the bulging region on the thermal factor.

- Develop a technique allowing to approximate an arbitrary three-dimensional weld pool geometry, including geometrical particularities such as the bulging region.
- Develop a method for the three-dimensional calculation of the main solidification parameters, i.e., the crystal axis, the growth rate, and the cross-sectional area of the columnar crystal, using the approximated weld pool geometry as an input parameter.
- Use the calculated solidification parameters to identify the solidifying regions experiencing a solidification delay, i.e., increased dwell time of the liquid film residing on the grain boundaries, and estimate, based on this, the influence of the bulging region on the metallurgical factor.
- Develop a method allowing to utilize the approximated weld pool geometry as an EHS and compute the global temperature history.
- Develop, based on models and submodels published in the literature, a comprehensive numerical model for the calculation of the global strains and stresses, which applies the temperature history obtained with the EHS as the thermal load.
- Use the calculated temporal evolution of the strains and stresses to identify the solidifying regions in which these increase at the final solidification stage and estimate, based on this, the influence of the bulging region on the mechanical factor.
- Rigorously verify and validate the developed models and the corresponding theoretical results.

3 Materials and Experimental Procedures

In the present work, it is distinguished between two types of experiments. The first type aims to provide qualitative results, which are used to confirm the existence of the bulging region. In contrast, the second type of experiment was designed to deliver quantitative results. These results are utilized for both setting up the multiphysics mathematical framework presented in Chapter 4 and validating the predictions made with it. All measured data utilized for validation purposes were obtained according to the ISO/TS 18166:2016 standard, which provides a workflow for the execution, verification, validation, and documentation of a numerical welding simulation within the field of computational welding mechanics [100].

3.1 Materials and Metallography

Two materials were utilized in the experimental procedures, namely hot-rolled unalloyed structural S355J2+N and austenitic chrome-nickel 316L steel sheets. The S355J2+N steel sheets were used for the real-time visualization of the bulging region and the validation of the numerically obtained results. For this purpose, 15 mm thick sheets were used to experimentally prove the existence of the bulging region, and 12 mm thick sheets were utilized to provide validation data for the theoretical predictions. Additionally, 2 mm thick 316L steel sheets were used to validate the crystal structure computed with the solidification model, see Section 4.3. The choice of the 316L steel was based on its higher contrast between different grains after etching. This contrast is caused by variations in the chemical composition of the grains, enabling a clear comparison between the experimental and numerical results. The chemical composition of the materials used was measured with spark optical emission spectroscopy and is given together with the corresponding standards [107, 108] in Tables 3.1 and 3.2.

To validate the computational results, the geometry of the FZ in the weld cross-sections and the crystal structure on the top surface of the welded steel sheets were determined metallographically. The metallographic cross-sections for both materials were obtained by perpendicular cuts to the welding direction taken from the region where the process is considered quasi-static. The macro-cuttings of the 12 mm thick S355J2+N steel sheets were prepared with a 2% nital etching, according to [109]. For the validation of the numerically estimated crystal axis, the 2 mm thick 316L steel sheets were used. To obtain metallographic samples from the top surface, the sheets were first polished until the structure was examined in an even horizontal section. Subsequently, the corresponding microstructure in the horizontal section and the weld cross-section was visualized by color etching, according to Bloech and Wedl II [109].

Table 3.1: Standardized and measured chemical composition of the S355J2+N steel in wt. %

	C	Si	Mn	P	S	Cr	Cu	Fe
DIN EN 10025-2 [107]	≤ 0.2	≤ 0.55	≤ 1.6	≤ 0.035	≤ 0.035	-	≤ 0.55	bal.
Measured (15 mm)	0.116	0.29	0.79	0.013	0.009	0.052	0.027	bal.
Measured (12 mm)	0.088	0.34	1.38	0.011	0.002	0.048	0.02	bal.

Table 3.2: Standardized and measured chemical composition of the 316L steel in wt. %

	C	Si	Mn	P	S	Cr	Mo	Ni	Fe
DIN EN 10088-3 [108]	≤ 0.03	≤ 1.0	≤ 2.0	≤ 0.045	≤ 0.03	16.5 - 18.5	2.0 - 2.5	10.0 - 13.0	bal.
Measured (2 mm)	0.03	0.39	1.36	0.04	0.004	16.95	2.28	10.57	bal.

3.2 Real-Time Visualization of the Bulging Region

The qualitative experimental proof of the existence of the bulging region requires a specially designed setup due to the optical inaccessibility of the LBW process. In the present experimental approach, a butt joint configuration of 15 mm thick hot-rolled unalloyed structural S355J2+N steel sheet and transparent flame-fused FN08 quartz glass was utilized to enable the observation of the liquid metal in the longitudinal section in real-time [110, 111]. The center of the laser spot was adjusted to symmetrically distribute the laser radiation between the steel sheet and the quartz glass. A schematic of the experimental setup, including the geometrical dimensions of the workpieces, is shown in Figure 3.1. The chemical composition of the steel and the process parameters used in the experiment are given in Tables 3.1 and 3.3, respectively. The quartz glass was selected according to the special requirements for the material properties. Its transmission properties for wavelengths between 200 nm and 2500 nm are up to 90%, thus providing suitable transparency for the laser wavelength of 1070 nm. Furthermore, its unique thermo-physical properties, such as low thermal conductivity, low thermal expansion coefficient, excellent thermal shock resistance, and high melting temperature, allow the glass–steel interface to be considered a plane of symmetry.

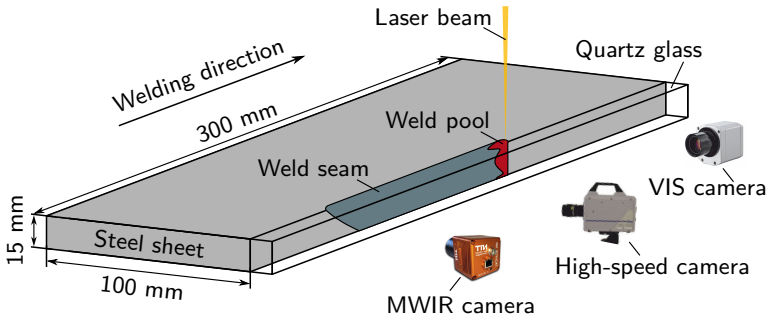

Figure 3.1: Schematic of the experimental setup utilized for the real-time visualization of the liquid metal in the longitudinal section

The geometrical characteristics of the liquid metal distribution in the longitudinal section were observed using an infrared camera, a thermal camera, and a high-speed camera, recording simultaneously from the glass side, see Figure 3.1. A TACHYON 16k infrared camera from NIT with a sensor allowing for detection of medium wavelength infrared (MWIR) light, i.e., in the range of approximately 1000 nm to 5000 nm, was used. The sensor has a minimum detection temperature of 100 °C and a maximum frame rate of 2000 Hz. The intersection between the spectral transmission of the glass and the detecting range of the MWIR camera allows visualizing the thermal profile of the liquid metal through the glass. In addition, a second thermal camera, PI 05M from Optris, was utilized, which is well suited

for temperature measurements of liquid metals. This camera is used for laser applications without a filter and works within the visible light spectrum (VIS), i.e., for wavelengths in the range of about 500 nm to 540 nm. Moreover, it offers a wide temperature measurement range reaching from 900 °C to 2450 °C. The quartz glass is fully transparent for the complete wavelength range of the MWIR and VIS cameras, and therefore does not interfere with the laser radiation and reflections. The FASTCAM SA4 high-speed camera from Photron was set at 10,000 frames per second and equipped with a filter with a bandwidth of (808 ± 10) nm to reduce the process emissions, thus permitting the visualization of the liquid metal.

3.3 Temperature Measurements and Weld Pool Dimensions

The experimental setup described here was used to provide quantitative reference data for the validation of the calculated temperature distribution and weld pool geometry obtained with the models described in Sections 4.1 and 4.4. Due to limitations of the technical equipment, in particular, the combination of the laser sources, the cameras, and the clamping device, the measurements were performed on 12 mm thick S355J2+N steel sheets. The specimens were

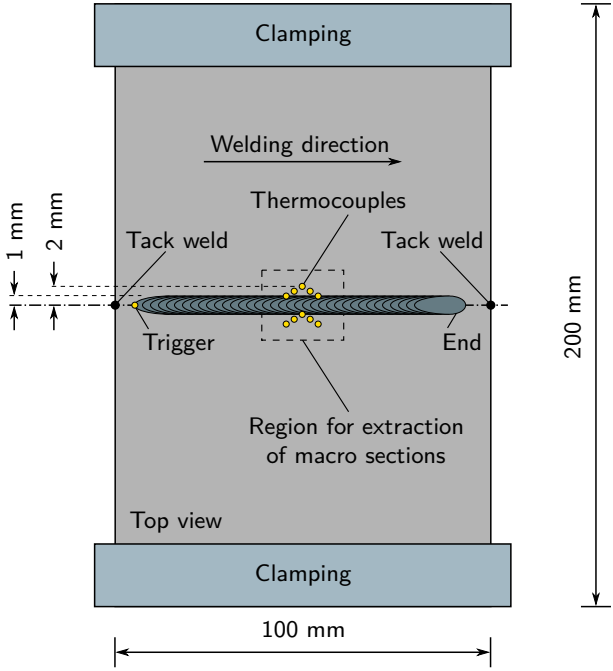

Figure 3.2: Schematic of the experimental setup used for the temperature measurement

tack welded at the beginning and at the end of the weld centerline and clamped along their free edges as shown in Figure 3.2. These were welded in a single pass on a linear welding trajectory with a technical zero gap width.

Thermocouples of type K (Ni/Cr − Ni) with diameters of 0.1 mm were used to measure the temperature. Thereby, the maximum diameter of the corresponding hot junctions was approximately 0.2 mm. The sampling rate for the measurements was set to 300 Hz. The thermocouples were placed at the top and bottom surfaces of the steel sheets at distances between 1 mm and 2 mm from the weld centerline, as indicated in Figure 3.2. The exact positions of the hot junctions were measured with an optical microscope after the welding process. In addition, to validate the dimensions of the weld pool geometry, macro sections were extracted from the region where the process is considered quasi-static, see Section 3.1.

3.4 Process Parameters

The experiments were conducted using two different laser systems: a 20 kW Yb:YAG fiber laser YLR-20000 from IPG Photonics and a 16 kW Yb:YAG disc laser 16002 from Trumpf. The IPG YLR-20000 laser system was utilized for the experiments with 15 mm thick S355J2+N steel sheets, as these required higher laser power. In contrast, the Trumpf 16002 laser system was used for the experiments with 12 mm thick S355J2+N and 2 mm thick 316L steel sheets. The process parameters used in the experiments are grouped depending on the utilized laser system and summarized in Tables 3.3 and 3.4.

Table 3.3: Process parameters of the experiments performed with the 20 kW Yb:YAG IPG YLR-20000 fiber laser system

Wavelength	1070 nm
Fiber diameter	200 µm
Beam parameter product	11.5 mm mrad
Optical system	HIGHYAG BIMO HP
Focal diameter	560 µm
Focal length	350 mm
Rayleigh length	6.8 mm
Material	S355J2+N
Sheet thickness	15 mm
Laser power	18 kW
Focal position	−5 mm
Welding speed	2 m min^{-1}
Laser torch angle	0°
Shielding gas nozzle angle	35°
Shielding gas	Ar, 25 L min^{-1}

Table 3.4: Process parameters of the experiments performed with the 16 kW Yb:YAG Trumpf 16002 disc laser system

Wavelength	1030 nm	
Fiber diameter	200 µm	
Beam parameter product	8 mm mrad	
Optical system	Trumpf BEO D70	
Focal diameter	420 µm	
Focal length	425 mm	
Rayleigh length	5.6 mm	
Material	S355J2+N	316L
Sheet thickness	12 mm	2 mm
Laser power	14 kW	2.3 kW
Focal position	−2 mm	5 mm
Welding speed	2 m min^{-1}	1.2 m min^{-1}
Laser torch angle	0°	0°
Shielding gas nozzle angle	15°	35°
Shielding gas	N_2, 25 L min^{-1}	Ar, 50 L min^{-1}

4 Description of the Developed Models

This chapter describes the computational studies conducted in the present work. These aim at the methodical mathematical analysis of the influence of the bulging region on the centerline cracking susceptibility, as hypothesized in Chapter 2. Hence, a multiphysics mathematical framework consisting of five models linked by one-way couplings has been developed, see Figure 4.1. The framework is designed to fulfill the objectives defined in Section 2.5 and is based on the EHS technique, which is further extended here to allow for the consistent coupling of the models.

The mathematical framework consists of two simulation chains, describing the thermo-metallurgical and thermo-mechanical interactions, which determine the susceptibility to solidification cracking, see Section 2.2. Thereby, chain I is defined by the simulation sequence $1 \rightarrow 2 \rightarrow 3$, and chain II by the simulation sequence $1 \rightarrow 2 \rightarrow 4 \rightarrow 5$, as illustrated in Figure 4.1. The first model (1) is a thermo-fluid dynamics model, which enables the phenomenological reproduction of the three-dimensional weld pool geometry, and thus of the bulging region, by a steady-state simulation of the fluid flow and heat transfer on a local level. The weld pool geometry calculated herewith is subsequently approximated with Lamé curves in the second model (2). This novel technique enables a complete and accurate three-dimensional approximation of an arbitrary weld pool geometry, including geometrical particularities such as the bulging region. The third model (3) uses the approximated weld pool geometry from (2) to describe the solidification process of a single three-dimensional columnar crystal, thus representing an approach for calculating the main solidification

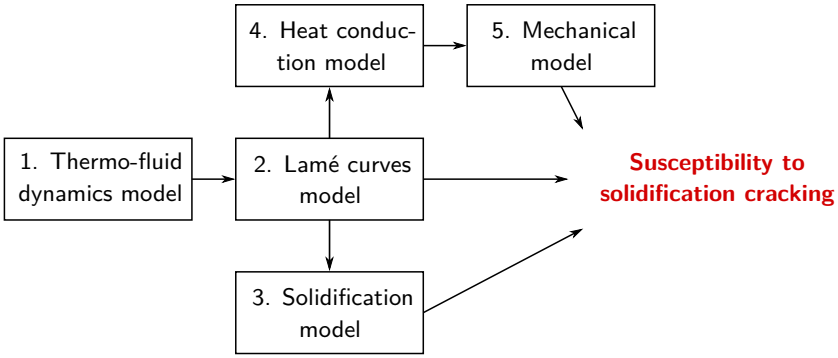

Figure 4.1: Flowchart of the developed multiphysics mathematical framework

parameters, namely the crystal axis, the growth rate of the crystal, and its cross-sectional area. Furthermore, the predicted solidification parameters are used to qualitatively estimate the extended dwell time of the liquid film residing on the grain boundaries, caused by solute enrichment in the liquid metal ahead of the solidification front. The outcomes from the second model (2) are used once more in the fourth model (4), which calculates the global transient temperature distribution by utilizing the approximated weld pool geometry as an EHS. The fifth model (5) represents a two-dimensional mechanical model, which uses the predicted temperature distribution as a transient thermal load to estimate the spatial and temporal strain and stress distribution.

A point worth stressing is that there can be two definitions of the weld pool boundary dependent on its subsequent application in the framework. When utilized in the solidification model (3), the weld pool boundary can be defined by the isothermal surfaces of either the liquidus or the solidus temperature since the solidification process begins in the so-called mushy zone, which is defined between these two isosurfaces. On the other hand, when used as an EHS in (4), the weld pool boundary should be defined by the solidus isosurface to include the amount of latent heat of solidification. In addition, note that a left-handed Cartesian coordinate system with positive values in the beam direction was used to define the models of the multiphysics mathematical framework.

4.1 Weld Pool Simulation

The weld pool simulation described here aims to obtain the three-dimensional steady-state weld pool geometry and temperature distribution on a local level, including the bulging region, as observed experimentally in Section 3.2. For this purpose, several basic physical phenomena have been mathematically described and coupled with the mass, momentum, and energy conservation equations and the transport equations for the turbulent kinetic energy and the turbulent dissipation rate. Thereby, the complexity of the mathematical description is confined to the most relevant physical effects, such as the thermo-capillary driven flow, known as the Marangoni convection, the natural convection, the latent heat of solidification, and the temperature dependence of the material properties, to ensure sufficient accuracy at a comparatively low computational cost. As there is comprehensive published research on weld pool modeling in LBW, see Section 2.4, the present model is based on several previous works [68, 69, 112], including some further improvements and modifications. The physical phenomena, their coupling to the corresponding conservation and transport equations, and the assumptions made in the model are discussed in detail in the following subsections.

4.1.1 Assumptions and Governing Equations

The quasi-steady-state mathematical formulation of the thermo-fluid dynamics problem is based on the following assumptions and simplifications:

- The liquid metal is considered to be an isotropic Newtonian and incompressible fluid [68, 69]. Moreover, since the mass density varies only slightly in the temperature range

above the liquidus temperature $\left(\Delta\rho \ll \rho_{\text{liq}}\right)$, the density variations due to temperature differences are accounted for by the Boussinesq approximation [113].

- It is assumed that a steady state is reached. Thus, the time derivatives in the governing PDEs are neglected [112].
- An Eulerian reference frame is used, i.e., the workpiece is considered infinitely long and moving relative to the origin of the Cartesian coordinate system, which coincides with the origin of the laser beam [69, 112]. Consequently, the determined quasi-steady-state solution does not include the formation, collapsing, or closing of the keyhole.
- The deformation of the weld pool and the keyhole surfaces is not taken into account, i.e., the dynamic effect of the recoil pressure, causing temporal keyhole oscillations or unstable free surfaces, is neglected and assumed to be perfectly balanced by the surface tension force [69, 112]. Thus, the process is assumed to be symmetrical.
- The laser beam is replaced by an EHS, as described in Section 2.4.2, which represents a keyhole of right circular cone geometry [114]. Thereby, an inclination of the keyhole is not considered due to the moderate welding speed used in the experiments, see Tables 3.3 and 3.4. Furthermore, the keyhole surface temperature is set to the evaporation temperature of the material, assuming that the temperature inside the keyhole should be at least equal to or higher than the evaporation temperature of the processed material [73, 96]. According to [66, 115], the heat input and the resulting amount of liquid metal are mainly determined by the keyhole diameter. Hence, in the proposed configuration, the keyhole radii are defined as a model parameter, dependent on the penetration depth and used for the calibration of the model. In employing such an approach, it should be ensured that the amount of energy absorbed by the processed steel sheets through the keyhole surface results in a plausible process efficiency value determined under similar experimental conditions and process parameters. This means that for complete penetration LBW, the surface integral of the conductive heat flux through the keyhole surface should yield an energy amount in the range of 65% to 85% of the input laser power [75]. Furthermore, since the keyhole diameter is much smaller than the width of the weld pool, the influence of the keyhole geometry on the flow field is assumed to be relatively small [66, 69].
- As the chosen numerical setup does not allow for considering the effects of the focal position and the multiple reflections on the energy absorption, which play a crucial role in the formation of the bulging region [8, 12, 54], the horizontal cross-sectional area of the keyhole in the middle of the steel sheet is slightly increased to enhance the bulging in the narrow regions around the keyhole.
- Heat losses due to radiation and convection are neglected because of the large volume-to-surface area ratio of the steel sheet [66, 91]. Moreover, heating due to the laser-induced weekly ionized metallic vapor is not considered because of the low heat absorption for the wavelength of around 1 µm [116, 117] and the minor differences

between the evaporation temperature of the material and the temperature of the metallic vapor [118].

- Although many experimental and theoretical attempts have been made to determine the flow regime in the weld pool, the question of how the flow should be treated numerically remains open. However, it has been shown that turbulence models are more accurate for specific cases [70, 71, 119],[AC7] especially in high-velocity regions of the weld pool, e.g., near the top and bottom surfaces of the welded steel sheets [72]. Therefore, a turbulent flow pattern is accounted for in the model by combining the steady-state Reynolds-averaged-Navier-Stokes equations with the standard $\kappa - \epsilon$ turbulence model [120].
- As the mass density of the liquid metal is several orders of magnitude higher than the mass density of the surrounding mixture of air and process gases and since the formation of a thermal boundary layer has no significant influence on the predicted weld pool geometry, the keyhole surface, as well as the surfaces of the steel sheet, are assumed to be frictionless [121].

The governing differential equations are given as implemented in the finite element software COMSOL Multiphysics® [122].

- Mass conservation equation

$$\nabla \cdot \mathbf{u} = 0, \tag{4.1}$$

where $\mathbf{u} = (u_x, u_y, u_z)$ is the fluid velocity vector.

- Momentum conservation

$$\rho_{\text{liq}} \mathbf{u} \cdot \nabla \mathbf{u} = \nabla \cdot \left[-p\mathbf{I} + (\eta + \eta_{\text{turb}}) \left(\nabla \mathbf{u} + (\nabla \mathbf{u})^{\top} \right) \right] + \mathbf{F}, \tag{4.2}$$

where ρ_{liq} is the mass density at the liquidus temperature, p is the fluid pressure, $\mathbf{I}$ is the identity matrix, η is the dynamic viscosity, η_{turb} is the turbulent viscosity, and $\mathbf{F}$ is the source term; the superscript $\top$ denotes the transpose of a matrix. Here, $\mathbf{F}$, is defined as follows:

$$\mathbf{F} = \rho_{\text{liq}} \mathbf{g} \left(1 - \beta \left(T - T_{\text{melt}} \right) \right) - c_1 \frac{\left(1 - f_{\text{L}}\right)^2}{f_{\text{L}}^3 + c_2} \left(\mathbf{u} - \mathbf{v}_{\mathbf{weld}} \right). \tag{4.3}$$

The first term on the right-hand side of Equation (4.3) represents the hydrostatic pressure and the Boussinesq approximation accounting for the thermal buoyancy. Here $\mathbf{g}$ is the gravity acceleration vector, β is the volumetric thermal expansion coefficient, T is the temperature, and T_{melt} is the melting temperature defined as $T_{\text{melt}} = \left(T_{\text{sol}} + T_{\text{liq}} \right) / 2$, where T_{sol} and T_{liq} are the solidus and liquidus temperatures, respectively. The second term is the solidification term described by the Carman-Kozeny equation [123]. Numerically, this term tends to zero in the liquid phase and to infinity in the solid phase, which mimics a solid behavior by

Table 4.1: Model constants for the $\kappa - \epsilon$ turbulence model [120]

Constant	C_η	C_{ϵ_1}	C_{ϵ_2}	σ_ϵ	σ_κ
Value	0.09	1.44	1.92	1.0	1.3

severely damping the acceleration of the material outside the weld pool region resulting from the momentum equation [124]. In addition, the term also accounts for the effect of the mushy zone, which is treated similarly to porous media. The two computational constants are chosen to be very large $\left(c_1 \sim 1 \times 10^6\,\mathrm{kg\,m^{-3}\,s^{-1}}\right)$ for the deceleration of the flow, which is linked to the inverse of the size of the interdendritic structure, and very small $\left(c_2 \sim 1 \times 10^{-3}\right)$ to avoid division by zero, respectively [125]. Due to the Eulerian approach used in the quasi-steady-state formulation of the thermo-fluid dynamics model, the welding speed vector, $\mathbf{v_{weld}} = \left(v_{\mathrm{weld}_x}, v_{\mathrm{weld}_y}, v_{\mathrm{weld}_z}\right)$, must be subtracted from the fluid velocity vector, $\mathbf{u}$. This allows the solid material to move through the computational domain at the desired welding speed. The function, f_L, represents the liquid fraction in the finite element and is defined as follows:

$$f_\mathrm{L} = \begin{cases} 0 & \text{for} \quad T \leq T_\mathrm{sol} \\ \frac{T - T_\mathrm{sol}}{T_\mathrm{liq} - T_\mathrm{sol}} & \text{for} \quad T_\mathrm{sol} < T < T_\mathrm{liq} \\ 1 & \text{for} \quad T \geq T_\mathrm{liq}. \end{cases} \tag{4.4}$$

The liquid fraction is assumed to vary linearly as the temperature decreases within the mushy zone. To avoid numerical instabilities, which can arise at the phase boundary where material parameters differ significantly in magnitude [18], the liquid fraction is numerically approximated with a smoothed Heaviside function [126].

- The transport equations for the turbulent kinetic energy, κ, and the turbulent dissipation rate, ϵ, read [127]:

$$\rho_\mathrm{liq}\mathbf{u} \cdot \nabla\kappa = \nabla \cdot \left[\left(\eta + \frac{\eta_\mathrm{turb}}{\sigma_\kappa}\right)\nabla\kappa\right] + P_\kappa - \rho\epsilon, \tag{4.5}$$

$$\rho_\mathrm{liq}\mathbf{u} \cdot \nabla\epsilon = \nabla \cdot \left[\left(\eta + \frac{\eta_\mathrm{turb}}{\sigma_\epsilon}\right)\nabla\epsilon\right] + C_{\epsilon_1}\frac{\epsilon}{\kappa}P_\kappa - C_{\epsilon_2}\rho_\mathrm{liq}\frac{\epsilon^2}{\kappa}, \tag{4.6}$$

where the turbulent viscosity, η_turb, and the turbulent production term, P_κ, are given as follows:

$$\eta_\mathrm{turb} = \rho_\mathrm{liq} C_\eta \frac{\kappa^2}{\epsilon}, \tag{4.7}$$

$$P_\kappa = \eta_{\text{turb}} \left[\nabla \mathbf{u} : \left(\nabla \mathbf{u} + (\nabla \mathbf{u})^\top \right) \right]. \tag{4.8}$$

Here the : symbol means a contraction over two indices, see [128]. The remaining model constants C_η, C_{ϵ_1}, C_{ϵ_2}, σ_ϵ, and σ_κ are designed to satisfy the physical consistency of the turbulence model. These are determined from experimental data and taken from the literature [120]. The constants and their corresponding values are listed in Table 4.1.

- Energy conservation

$$\rho_{\text{liq}} C_p^{\text{app}} \mathbf{u} \cdot \nabla T + \nabla \cdot q = 0, \tag{4.9}$$

where C_p^{app} is the apparent heat capacity and q the heat flux. By making use of the apparent heat capacity method [129], the latent heat of solidification, H_{f}, is taken into account:

$$C_p^{\text{app}} = C_p^0 + \frac{\exp\left[-\left(\frac{T - T_{\text{melt}}}{\Delta T} \right)^2 \right]}{\sqrt{\pi} \Delta T} \cdot H_{\text{f}}. \tag{4.10}$$

Here, H_{f} is normally distributed within the mushy zone, which is modeled by a half width of $\Delta T = 50\,\text{K}$ [130]. Note that although the real solidification range is narrower, a further decrease to $\Delta T = 35\,\text{K}$ does not lead to any significant difference in the predicted weld pool geometry and the liquid metal flow therein. The sum of the temperature-dependent heat capacity, C_p^0, and the released latent heat of solidification, H_{f}, defines the final apparent heat capacity, C_p^{app} [131]. Here, the energy needed for the ferrite-austenite phase transformation is included in the C_p^{app} curve shown in Figure 4.10. However, the austenite-martensite phase transformation does not affect the parameters which are decisive for the solidification cracking and is therefore not accounted for in the material properties used in the developed multiphysics mathematical framework. More details on the material modeling are given in Section 4.6.2.

As the steady-state Reynolds-averaged-Navier-Stokes equations are combined with the $\kappa - \epsilon$ turbulence model, the Kays-Crawford heat transport turbulence model is applied to modify the heat conductivity, by accounting for the turbulent component [132]. Thereby, the heat flux is defined as:

$$q = -\lambda_{\text{eff}} \nabla T, \tag{4.11}$$

where $\lambda_{\text{eff}} = \lambda + \lambda_{\text{turb}}$ is the effective thermal conductivity. The turbulent thermal conductivity, λ_{turb}, is given as a function of the turbulent dimensionless Prandtl number, Pr_{turb}:

$$\lambda_{\text{turb}} = \frac{\eta_{\text{turb}} C_p^{\text{app}}}{\text{Pr}_{\text{turb}}}. \tag{4.12}$$

It should be noted, nonetheless, that the extended Kays-Crawford model provides more

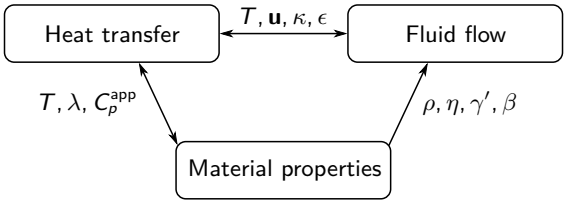

Figure 4.2: Physical domains and corresponding coupling variables

accurate approximation of turbulent flows in liquid metals [133]. Yet, to use the extended model, the Reynolds number at infinity must be provided either as a constant or as a function of the flow field. Nevertheless, the estimation of the Reynolds number in the weld pool represents a non-trivial task due to the unknown characteristic length [71, 110]. Thus, the implementation of the extended Kays-Crawford model is omitted in the proposed model setup.

The bi-directional coupling of the single physics is visualized in Figure 4.2. Note that the surface tension, γ', included in Figure 4.2, does not appear in the governing equations of the thermo-fluid dynamics model as it is used to consider the thermo-capillary driven flow induced by the surface tension gradient in the form of a boundary condition, see Section 4.1.2. The solving sequence of the thermo-fluid dynamics model begins with estimating the fluid flow variables, i.e., velocity and pressure. In the subsequent computation steps, the turbulent variables and the temperature field are calculated using the velocity field from the first step to account for the convective energy transport. Once the temperature field is determined, the local material properties are adjusted according to their temperature dependence, thus inducing a change in the flow field. This procedure is done iteratively until the velocity and temperature fields reach a steady state. All equations were solved with the commercial finite element software COMSOL Multiphysics 5.4® [122].

4.1.2 Computational Domain and Boundary Conditions

The computational domain of the thermo-fluid dynamics model has the geometrical dimensions of 70 mm in length, 10 mm in width, and 12 mm in thickness, see Figure 4.3. In the model, the process's symmetry is exploited, and therefore the computational domain represents only half of the real steel sheet. To further reduce computation cost, the domain is divided into finely and coarsely meshed regions, which are discretized with a polygonal mesh consisting of 1,241,520 tetrahedral and triangular elements. Thereby, the finer mesh, with a minimum element size of 0.1 mm, is used around and on the keyhole and symmetry surfaces, as well as on the top and bottom surfaces, influenced by the thermo-capillary convection, to resolve the locally steep temperature and velocity gradients, see Figure 4.3. The cell size outside the finely meshed region is defined by a growth rate of 1.05 and a maximum element size of 0.75 mm. Furthermore, to reduce the total number of elements and allow for finer spatial discretization of the weld pool region, the shape of the finely meshed region is

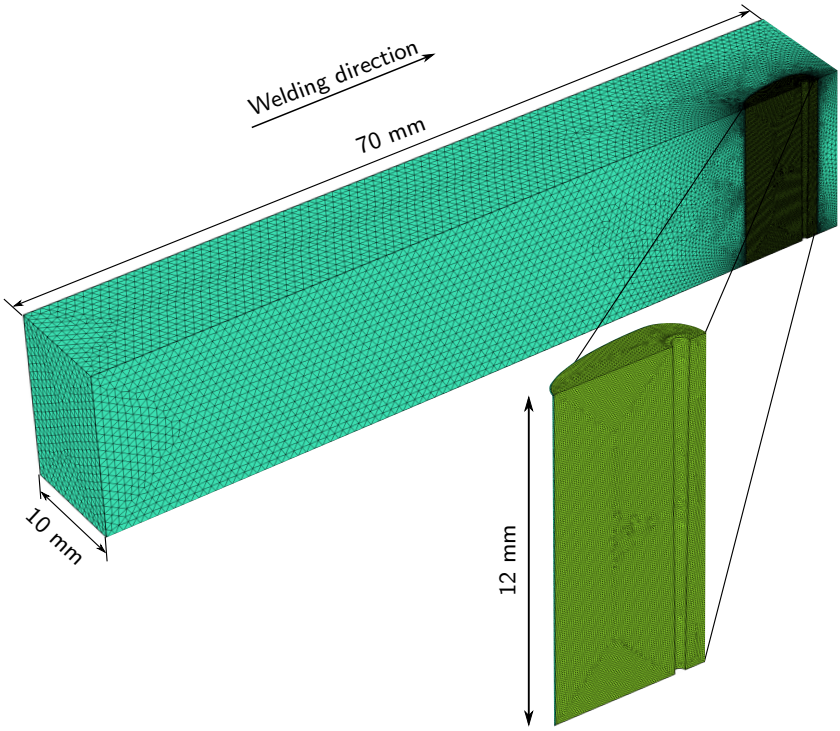

Figure 4.3: Discretization of the computational domain of the thermo-fluid dynamics model with an enlarged view of the weld pool and keyhole regions

derived from weld pool geometries calculated for similar welding conditions [18, 69], [AJ1], [AJ9]. The radii of the keyhole geometry utilized in the present work are given in Table 4.2.

The coupled fluid flow and heat transfer boundary conditions are summarized in Figure 4.4. All boundary conditions are constructed using the variables of interest: pressure, velocity, turbulent kinetic energy, turbulent dissipation rate, temperature, and their corresponding derivatives. The Eulerian approach used in the quasi-steady-state formulation of the thermo-

Table 4.2: Radii of the keyhole used in the weld pool simulation

Height, mm	0	2	4	6	8	10	12
Radius, mm	0.33	0.32	0.27	0.36	0.28	0.33	0.34

fluid dynamics model requires inlet and outlet boundaries to allow for the relative movement of the steel sheets to the laser beam. Thereby, the material enters the domain at the inlet with the welding speed and at room temperature. On the other hand, at the outlet, the material leaves the computational domain at the welding speed but at an increased temperature determined by the local heat and mass transfer. Nevertheless, the energy transport by conduction through the outlet is neglected since the temperature distribution behind the weld pool is rather homogeneous, i.e., the temperature gradient is low [18, 39]. The inlet and outlet boundary conditions are defined as follows:

- Right surface (inlet)

$$u_x = -v_{\text{weld}_x}, \qquad T = T_0, \qquad \kappa = \frac{3}{2}\left(v_{\text{weld}_x} I_T\right)^2, \qquad \epsilon = C_\eta^{3/4}\frac{\kappa^{\frac{3}{2}}}{L_T}. \tag{4.13}$$

Here, $I_T = 0.05$ is the dimensionless turbulent intensity and $L_T = 0.01$ is the turbulent length scale given in m [120].

- Left surface (outlet)

$$p = p_0, \qquad u_y = 0, \qquad u_z = 0, \qquad \frac{\partial T}{\partial x} = 0, \qquad \nabla\kappa \cdot \mathbf{n} = 0, \qquad \nabla\epsilon \cdot \mathbf{n} = 0. \tag{4.14}$$

where $\mathbf{n}$ is the unit normal inward vector of the surface and p_0 is the ambient pressure.

- Top and Bottom surface (wall)

To account for the thermo-capillary driven flow induced by the variations of the surface tension with temperature [134, 135], shear stress is prescribed in the corresponding liquid regions on the top and bottom surface of the steel sheet. In contrast, the solid regions on these surfaces are modeled as frictionless, and thus the shear stress there vanishes. Furthermore, due to the dominant convective energy transport and large volume-to-surface-area ratio of

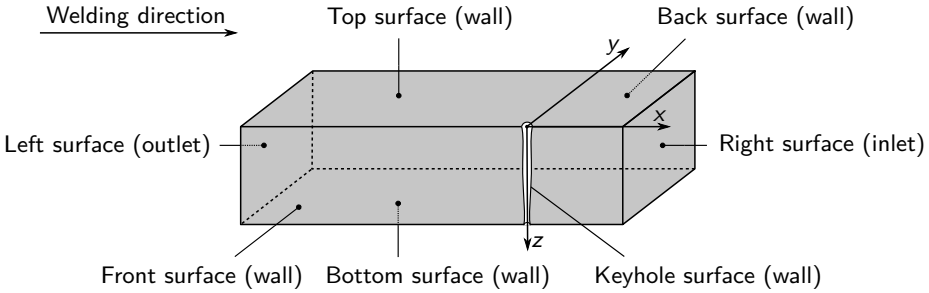

Figure 4.4: Boundary conditions of the thermo-fluid dynamics model

the steel sheet, the heat loss through the top and bottom surfaces are neglected. These boundaries are considered adiabatic, i.e., perfectly insulated, and thus impermeable to the flow of heat across them. In addition, the velocity component in the normal direction to the top and bottom boundaries is set to zero, and hence, no mass can be transferred through these boundaries. The boundary conditions on the top and bottom surfaces are given as:

$$\eta\frac{\partial u_x}{\partial z} = f_L\frac{\partial \gamma}{\partial T}\frac{\partial T}{\partial x}, \qquad \eta\frac{\partial u_y}{\partial z} = f_L\frac{\partial \gamma}{\partial T}\frac{\partial T}{\partial y},$$
$$u_z = 0, \qquad \frac{\partial T}{\partial z} = 0, \qquad \nabla\kappa\cdot\mathbf{n} = 0, \qquad \nabla\epsilon\cdot\mathbf{n} = 0. \tag{4.15}$$

- Front and Back surface (wall)

The front and back surfaces in the model are used to bound the material and prevent it from leaving the computational domain. Mathematically, the constraints on these boundaries can be formulated as follows:

$$u_y = 0, \quad \frac{\partial u_x}{\partial y} = 0, \quad \frac{\partial u_z}{\partial y} = 0, \quad \frac{\partial T}{\partial y} = 0, \quad \nabla\kappa\cdot\mathbf{n} = 0, \quad \nabla\epsilon\cdot\mathbf{n} = 0. \tag{4.16}$$

It is important to note that the domain's width (y-direction) is adapted with regard to the weld pool width so that no temperatures much higher than the room temperature appear near the back surface. In this way heat accumulation is prevented, resulting in more accurate computational results. Moreover, note that the front surface is typically considered a symmetry plane, and thus modeled with a symmetry boundary condition. This requires a zero normal velocity component as well as a zero flux of all dependent variables on the symmetry boundary; these requirements are fulfilled by the slip wall boundary condition defined in Equation (4.16).

- Keyhole surface (wall)

Since the keyhole surface is assumed to be fixed and frictionless, the normal component of the velocity and the shear stress should vanish. Furthermore, the keyhole surface is used as an EHS in the weld pool simulation. Therefore, its temperature is prescribed with the corresponding evaporation temperature of the processed material. The conditions defined on the keyhole boundary are expressed as follows:

$$\mathbf{u}\cdot\mathbf{n} = 0, \qquad \nabla\mathbf{u}\cdot\mathbf{n} = 0, \qquad T = T_{ev}, \qquad \nabla\kappa\cdot\mathbf{n} = 0, \qquad \nabla\epsilon\cdot\mathbf{n} = 0, \tag{4.17}$$

where T_{ev} is the evaporation temperature of the material, see Table 4.3.

4.2 Lamé Curves Approximation of the Weld Pool Geometry

The accurate approximation of the three-dimensional steady-state weld pool geometry plays a crucial role in the proposed mathematical framework as it enables the coupling of the different models, see Figure 4.1, and hence the study of the influence of the bulging region on the thermo-metallurgical and thermo-mechanical interactions, which determine the susceptibility to solidification cracking. As described at the beginning of Chapter 4, the approximated weld pool geometry is utilized in both simulation chains. Thereby, the first simulation chain uses the weld pool geometry to calculate the main solidification parameters, in particular, the crystal axis, the growth rate, i.e., the solidification rate, and the corresponding cross-sectional area of a columnar crystal. In contrast, the second simulation chain applies it as an EHS.

In general, two different weld pool geometries can be defined and used in the simulation chains. In the solidification model, the weld pool geometry can be either defined by the isothermal surface of the liquidus or the solidus temperature, see Section 4.3. On the contrary, when used as an EHS in the heat conduction model, the weld pool geometry should be defined by the isothermal surface of the solidus temperature to include the amount of latent heat of solidification. Both the solidus and the liquidus isosurface can be obtained

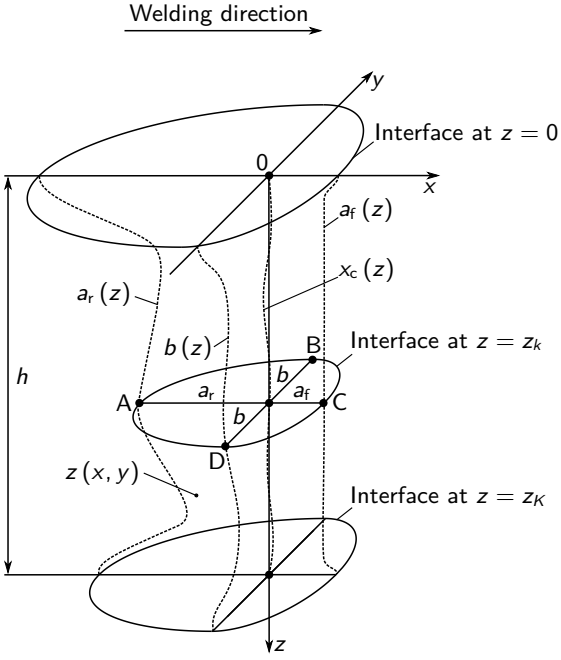

Figure 4.5: Schematic of the weld pool geometry approximated with Lamé curves

numerically. Nonetheless, the current literature indicates that only the solidus isosurface can be determined experimentally. Therefore, in the present work, the solidus isosurface is approximated and subsequently utilized in both simulation chains.

The Lamé curves approximation is based on the observation that in any horizontal section taken along the thickness direction, as schematically illustrated in Figure 4.5, the contours of the weld pool geometry have a similar shape, and thus can be mathematically described with a single expression. Here, each two-dimensional contour is approximated with two Lamé curves, also known as super-ellipses, one for the front and one for the rear part of the weld pool. The Lamé curves are explicitly determined by eight parameters, namely the semi-major axes, $a_{\mathrm{r,f}}(z)$, representing the approximated length of the front and rear parts of the weld pool; the semi-minor axis, $b(z)$, defining the approximated half-width of the weld pool; the center of the Lamé curve, x_{c}, and the corresponding shape parameters, $m_{\mathrm{r,f}}(z)$ and $n_{\mathrm{r,f}}(z)$, expressed as functions of the z-coordinate, see Figure 4.5. For the approximation, data points located on the solidus isosurface are extracted from the solution of the weld pool simulation and used to fit the parameters.

The complete mathematical description and numerical implementation of the Lamé curves approximation technique for an arbitrary three-dimensional weld pool geometry are given in Section 5.4.

4.3 Solidification of a Steady-State Weld Pool Geometry

The present solidification model aims to qualitatively estimate the change of the local solidus temperature during the steady-state solidification process of the weld pool. Therefore, the main solidification parameters, namely the geometry of the crystal axis, the growth rate, and the cross-sectional area of the crystal are computed and subsequently used to assess the decrease in the liquidus temperature due to a solute enrichment in the liquid metal ahead of the solidification front. Here, the approximated weld pool geometry, including the bulging region, is used to describe the solidification process of a single columnar crystal. The primary microstructure is determined by the rate and direction of solidification, which depend on the movement of the solidification front. Due to the complex nature of the solidification process, it is inevitable to limit the simulation to the effects influencing the process the most. Hence, the proposed solidification model is based on the following assumptions:

- The formation of substructures (planar, cellular, or dendritic) inside the grains are not accounted for since these have no significant influence on the macroscopic grain structure for polycrystalline materials [48].
- The solidification process is in a steady state, i.e., the weld pool dimensions do not change with time. This assumption is well established for continuous LBW on a linear welding trajectory and at moderate welding speed.
- The solidification front is not influenced by the rising impurity concentration, and thus kept constant in the computation. Moreover, its shape is represented by the isosurface of the solidus temperature, T_{sol}, obtained with the thermo-fluid dynamics model, see

Section 4.1, and approximated mathematically with Lamé curves, as described in the previous section.

- The crystallographic orientation of the crystals and the competitive growth between these crystals are not considered in the model as these effects significantly complicate the task [80]. Instead, as illustrated in Figure 4.6, it is assumed that the crystals grow along the temperature gradient, G, i.e., in the normal inward direction to the solidification front [48].

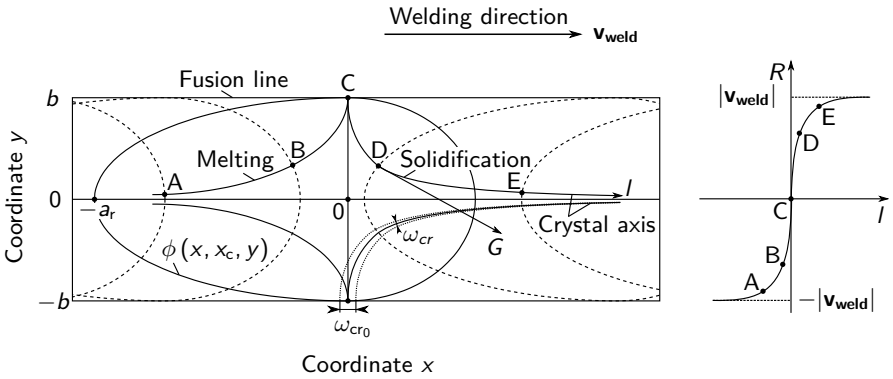

Figure 4.6: Schematic of a two-dimensional columnar crystal growth and a corresponding change of the growth rate during movement of a steady-state weld pool geometry

The basic approach used here refers to the concepts developed by Prokhorov [79] and Karkhin [33]. Thereby, the crystal starts growing from point C located at the fusion line, as exemplarily shown in Figure 4.6 for the two-dimensional case, where the trajectories of the melting and solidification fronts, depicted by the curves ABC and CDE, respectively, coincide. The crystal grows following the movement of the solidification front, $\phi(x, x_c, y)$, along the x-axis until it reaches the weld centerline, which in the mathematical sense represents its asymptote. During its growth, highlighted by the curve CDE, the crystal intersects the moving solidification front, depicted by the dashed lines in Figure 4.6, perpendicularly. Thus, the crystal axis can be determined by computing and connecting the intersection points. Once known, the intersection points are subsequently applied in the calculation of the growth rate, R, which is defined as the infinitesimal change in length, $\mathrm{d}l$, of the crystal axis, l, in the infinitesimal time interval, $\mathrm{d}t$. The growth rate is position dependent, changing from zero at point C to its maximum value of $R = |\mathbf{v}_{\mathbf{weld}}|$ on the weld centerline. Furthermore, since the cross-sectional area of the columnar crystal depends on its curvature, the intersection points are also used to calculate the area at any position along the crystal axis. This is done by using the explicit trigonometric relationship between the initial cross-sectional area, ω_{cr_0}, and the current cross-sectional area, ω_{cr}, of the crystal.

The developed solidification model comprises two methods for the calculation of the main solidification parameters. The first method is based on general analytical solutions derived for the case of two-dimensional columnar crystal growth, as described above. On the other hand, the second method represents a general numerical procedure enabling the calculation of the solidification parameters in the cases of two-dimensional or three-dimensional columnar crystal growth. The derivation of the analytical solutions and the description of the proposed numerical procedure are presented in detail in Section 5.5.

4.4 Global Heat Conduction Simulation with an Equivalent Heat Source

This chapter deals with the computation of the global transient temperature distribution in the joined components using the EHS technique. This technique enables the one-way coupling of the process and structure simulations, see Section 2.4.2, and thus the study of the influence of the bulging region on the thermal history and subsequently on the mechanical behavior of the welded parts. In addition, it also offers high accuracy and efficiency when solving the heat conduction equation compared to commonly used point [61, 62], line [89, 90], or volumetric heat sources, such as the cylindrical heat source, the conical heat source, or the elliptic cone heat source [91, 93, 136].

All the necessary information for the computation of the temperature field generated by the three-dimensional heat source is contained within the weld pool geometry [94]. By definition, the EHS coincides with the weld pool geometry and is defined as the isothermal surface of the solidus temperature. Once determined, the solidus isosurface is moved through the computational domain according to the welding trajectory at the welding speed. During the welding process, the mesh nodes located within the weld pool or on its surface are detected and assigned the solidus temperature, which results in a transient isothermal boundary condition assuring an equivalent heat input. It is important to note that the actual temperatures of the mesh nodes are higher than the prescribed solidus temperature. As a result, the total amount of heat contained in the EHS will be slightly lower than predicted by the weld pool simulation. However, the difference in the heat amount contained in the weld pool is lost only once at the end of the welding process, when the laser machine is turned off, and therefore has nearly no influence on the predicted temperature history. Outside the solidus isosurface, the heat conduction model is strictly valid. Hence, the temperature distribution there is determined by solving the energy conservation equation considering only heat transfer by conduction:

$$\rho_{\mathrm{hc}} C_p^0 \frac{\partial T}{\partial t} = \nabla \cdot q, \tag{4.18}$$

where ρ_{hc} is the mass density used for conductive heat transfer in the solid region, C_p^0 is the temperature-dependent heat capacity, see Section 4.6.1, q is the heat flux, and T is the temperature. Once the EHS reaches the end point of the weld, the prescription of the temperature is stopped, and the temperatures in the complete computational domain are obtained by solving Equation (4.18).

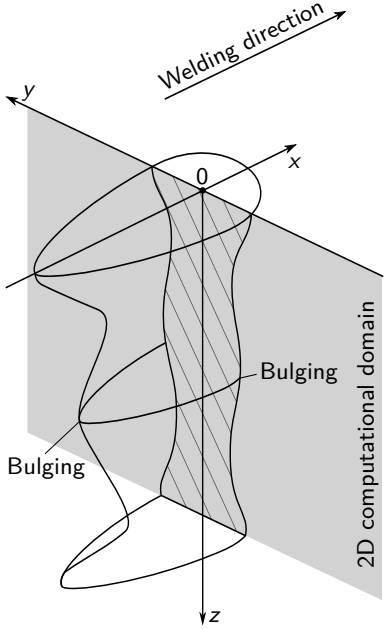

Figure 4.7: Schematic of a three-dimensional equivalent heat source moving through a two-dimensional computational domain

When welding at high speed and with high power, the temperature distribution behind the keyhole is rather homogeneous in the welding direction, i.e., the temperature gradient is low, and therefore the heat flux in the welding direction can be neglected [90]. Hence, the three-dimensional heat conduction model can be reduced to a two-dimensional model by considering only a cross-section perpendicular to the weld seam. As this is the case in the present work, see Tables 3.3 and 3.4, and since the EHS technique allows to consider the influence of any geometrical particularity of the weld pool geometry at a negligible loss of accuracy, the three-dimensional EHS is used to study the influence of the bulging region on the temperature field in 2D. Following the concept of the EHS technique described above, the temperature distribution in the cross-section is calculated by moving the solidus isosurface of the weld pool through it, as shown in Figure 4.7. Thereby, as in the three-dimensional case, the solidus temperature is assigned to all mesh nodes located within the weld pool or on its surface, see the hatched area in Figure 4.7, and the temperature distribution in the solid region is obtained by solving Equation (4.18). After the EHS has passed through the computational domain, the computation is continued without further prescription of the temperatures to account for the cooling stage of the process. To further reduce the computational intensity of the heat conduction model, the symmetry of the process is

exploited so that only half of the real weld seam is considered. Additionally, the heat loss through the top and bottom surfaces caused by radiation and convection is neglected, as described in detail in Section 4.1. Furthermore, the left and right boundaries are considered adiabatic as their temperature remains unchanged and equal to the room temperature during the computation. It is worth mentioning that the EHS technique offers one more advantage in terms of simplicity as it automatically accounts for the amount of latent heat of solidification considered in the energy balance on the solidus isosurface in the weld pool simulation, see Section 4.1.1.

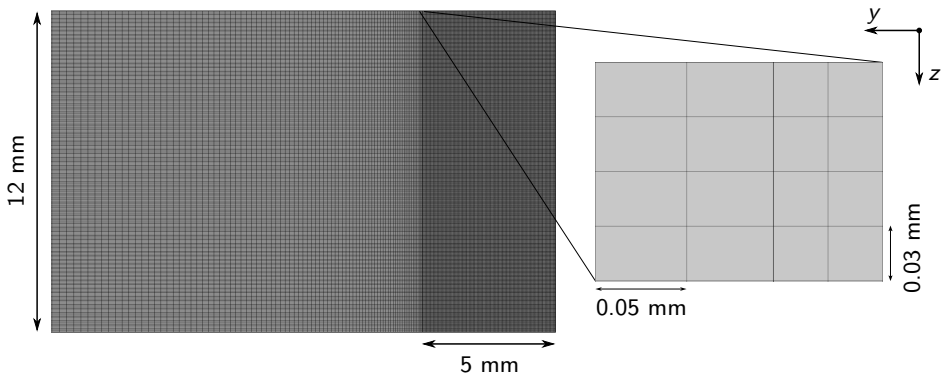

Figure 4.8: Discretization of the two-dimensional computational domain of the heat conduction and mechanical models

The 2D computational domain of the heat conduction model has the geometrical dimensions of 100 mm in width and 12 mm in thickness, see Figure 4.8. The domain is discretized with a mesh of about 166,800 quad elements with a minimum element size of 0.03 mm. In the model, the finest mesh is used in the region where the EHS passes through the computational domain, see Figure 4.8.

The transient temperature distribution was obtained with the commercial finite element software COMSOL Multiphysics 5.4® [122].

4.5 Mechanical Simulation

Typically, during welding, the joined components experience highly non-uniform heating. In LBW, the area close to the laser spot is heated up to a few thousand degrees Celsius due to the highly localized energy input and subsequently rapidly cooled down due to the conduction of the absorbed heat to the bulk of the welded structure [97]. The local heating and cooling induce volumetric changes, which result in deformations and thermal stresses, i.e., stresses caused by thermal expansions or contractions, often referred to as temporal stresses, as well as residual stresses [98]. In contrast, the influence of the material deformation on the

temperature field is small, and thus the mechanical simulation is weakly coupled to the temperature field simulation [99, 100].

The mechanical simulation presented here aims to study the influence of the bulging region on the temporal and spatial strain and stress evolution and, in particular, its correlation to the formation of solidification cracks. However, as estimated in [6], the computational intensity of a three-dimensional model is very high, which does not allow for discretizing the spatial and temporal domains properly. On the other hand, the discretization of these two domains determines the calculation accuracy of the physical quantities of interest. Hence, to ensure a high degree of accuracy and keep the computational time within reasonable limits, the three-dimensional model is mathematically reduced to two dimensions. To achieve this, a plane strain approach is applied in the formulation of the mechanical model, i.e., the long straight weld seam, see Figure 3.2, is considered in a cross-section model, neglecting all out-of-plane strain components [6]. Thus, it is assumed that the displacements of the steel sheet in the welding direction are negligible and that the in-plane displacements are independent of the x-coordinate. As a result of this mathematical reduction to two dimensions, the transient temperature distribution computed by the two-dimensional heat conduction model, using the weld pool geometry as an EHS, as illustrated in Section 4.4, can be directly applied as the thermal load in the mechanical model.

Governing Equations and Boundary Conditions

The solid mechanics problem is governed by the equilibrium equation given by Newton's second law, i.e., the equation of motion. Usually, this is mathematically expressed using a spatial formulation in terms of the Cauchy stress tensor, σ, as follows [122]:

$$\rho \frac{\partial^2 \mathbf{u}}{\partial^2 t} = \nabla \sigma + \mathbf{f_V}. \tag{4.19}$$

Here ρ is the mass density, $\mathbf{u}$ is the displacement vector, t is the time, and $\mathbf{f_V}$ is a body force per unit deformed volume. Nevertheless, the implementation of the strong form of the equilibrium equation in most commercial finite element analysis software is not based on the equation of motion but rather on the principle of virtual work [128, 137, 138].

In the current study, the inertial terms are excluded, resulting in a quasi-static formulation of the mechanical model, i.e., the mass effects are neglected. Accordingly, all second-order time derivatives must be set to zero, i.e., left-hand side of Equation (4.19). Furthermore, geometrical linearity is assumed, meaning that Equation (4.19) is formulated in the undeformed state and is not updated with the displacement. The material used in the mechanical simulation is characterized by an elastic-plastic response (von Mises yield surface) governed by a yield criterion, a flow rule, and a hardening rule. Thereby, isotropic hardening, also known as work hardening, is assumed, i.e., the yield surface expands in size as the plastic strain develops but remains centered about its initial centerline [139, 140]. In addition, it is assumed that the inelastic deformations at any given point of the welded structure are small. Therefore, an additive decomposition is used to express the total strain [106, 141]. In the mechanical model, the total strain is defined as the sum of the recoverable (elastic) and the

irrecoverable (inelastic) deformations:

$$\varepsilon_{\text{tot}} = \varepsilon_{\text{el}} + \varepsilon_{\text{pl}} + \varepsilon_{\text{th}} + \varepsilon_{\text{tr}}, \tag{4.20}$$

where the subscripts tot, el, pl, th, and tr stand for total, elastic, plastic, thermal, and transformation strain. In welding, the thermal strain is the driver of both elastic and inelastic deformations.

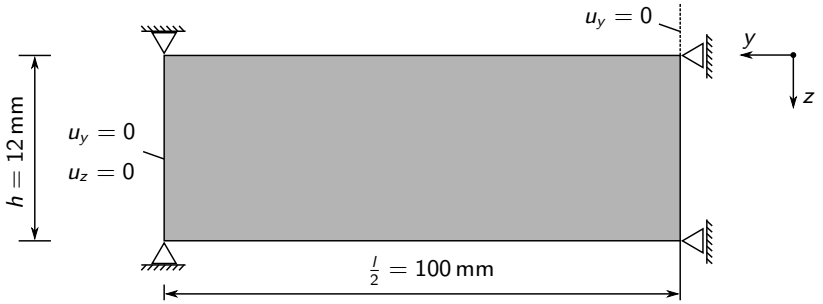

Figure 4.9: Boundary conditions of the mechanical model

The boundary conditions of the two-dimensional mechanical model are summarized in Figure 4.9. Note that the geometrical dimensions and the discretization of the computational domain are identical to the heat conduction model described in the previous section and can be seen in Figure 4.8. As described in Section 3.3, the specimens were tack welded at the beginning and the end of the weld centerline and clamped along their free edges as shown in Figure 3.2. Accordingly, the free edges were rigidly fixed in the model, i.e., the displacements u_y and u_z are set to zero. Moreover, the mechanical model is symmetrical, and therefore no displacement in the normal direction to the symmetry line is allowed, see Figure 4.9.

The 2D temporal and spatial stress evolution were obtained with the commercial finite element software COMSOL Multiphysics 5.4® [122].

4.6 Material Modeling

In the present work, 12 mm thick hot-rolled unalloyed structural S355J2+N steel sheets were utilized to study the influence of the bulging region on the susceptibility to centerline solidification cracking, see Section 3.1. Due to the different physical phenomena considered in the models of the multiphysics mathematical framework presented in Chapter 4, each model requires specific input of material properties. Therefore, the material properties used in the framework are divided into two groups, namely, thermophysical and thermomechanical. The thermophysical material properties are utilized in both the thermo-fluid dynamics model (1) and the heat conduction model (4), whereas the thermomechanical material properties are employed solely in the mechanical model (5). In contrast, the Lamé curves model (2) and

the solidification model (3) are not directly dependent on the material properties as these use the weld pool geometry calculated by thermo-fluid dynamics model as input parameter, see Figure 4.1.

4.6.1 Thermophysical Material Properties

The thermophysical material properties play a crucial role in the modeling of heat and mass transfer. Thus, these have been implemented as temperature-dependent up to the evaporation temperature in the thermo-fluid dynamics (1) and heat conduction model (4). However, in (4), only material properties for temperatures lower than the solidus temperature are required due to the applied EHS technique.

Since the material used, S355J2+N, is a hot-rolled unalloyed structural steel, it has to be modeled with the material properties of the different phases, namely ferrite **F**, perlite **P**, bainite **B**, austenite **A**, and martensite **M**. The S355J2+N steel has a BCC crystal structure known as ferrite, perlite, or the α-phase. During heating, the initial microstructure of the steel sheet, also called base metal, transfers either partially or completely into a FCC crystal structure called austenite or the γ-phase [48], depending on the peak temperature, T_{peak}. The transformation is partial when the peak temperature exceeds the austenitization starting temperature, A_1. Conversely, when T_{peak} exceeds the austenitization ending temperature, A_3, the base metal transfers completely into austenite. Usually, in the literature, A_{c1} and A_{c3} refer to the austenitization temperatures on heating, and A_{r1} and A_{r3} to the austenitization temperatures on cooling [142]. For simplicity, in the current material model, A_1 and A_3 are used instead. During cooling, the γ-phase transfers depending on the cooling rate from 800 °C (1073 K) to 500 °C (773 K), defined as the $\Delta t_{8/5}$ [106], to ferrite-perlite, bainite, or martensite. A point worth stressing is that the transformation to ferrite, perlite, or bainite is a diffusion-type transformation. Hence, the critical temperatures, A_1 and A_3, depend not only on the chemical composition but as well on the heating rate [143, 144]. In other words, an increase in the heating rate leads to a decrease in the duration of the diffusion process, which increases the required energy needed for the transformation by increasing the critical austenitization temperatures. Moreover, it should be noted that the increased critical temperatures result in an increased austenite formation rate. However, as the difference between $A_1 \approx 700\,^{\circ}\mathrm{C}\,(973\,\mathrm{K})$ and $A_3 \approx 850\,^{\circ}\mathrm{C}\,(1123\,\mathrm{K})$ is relatively small [145], and since in the case of deep penetration LBW the region between their corresponding isosurfaces is very narrow, in the material model the $\alpha \rightarrow \gamma$ transformation is determined only by A_3. Furthermore, according to [102, 146], below an austenitization temperature of about $A_3 = 800\,^{\circ}\mathrm{C}\,(1073\,\mathrm{K})$, the heat capacity and the thermal conductivity of the ferrite, perlite, bainite, and martensite phases are nearly identical. Therefore, the base metal of the S355J2+N steel is modeled as α-phase for temperatures up to $A_3 = 800\,^{\circ}\mathrm{C}$ and as γ-phase for higher temperatures, as indicated in Figure 4.10.

Moreover, as the variations of the mass density with temperature are accounted for in the weld pool simulation by the Boussinesq approximation, see Section 4.1.1, and since the maximum difference between the densities of the ferrite and the austenite phases is at room temperature and lies below 3% [102, 146], the mass density of the α-phase at

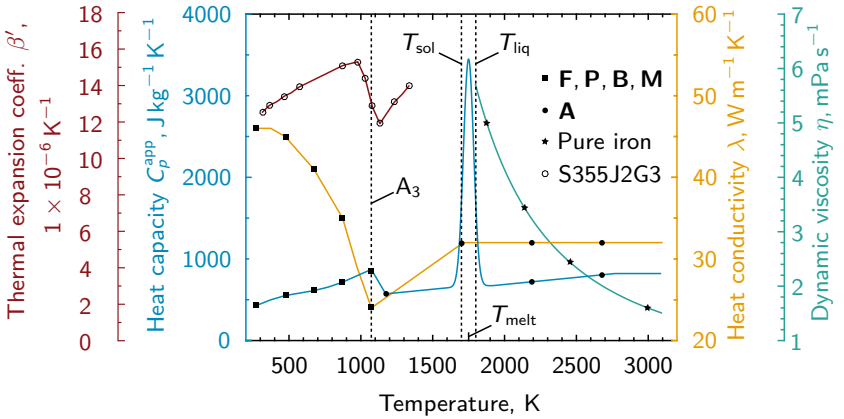

Figure 4.10: Thermophysical material properties of the unalloyed S355J2+N steel [146–150]

the liquidus temperature, $\rho_{liq} = 7300\,\mathrm{kg\,m^{-3}}$, is used to model the heat and mass transfer in the weld pool. This assumption affects the energy transport in the solid region since the mass density at room temperature is about 6% higher than the used constant value. Nonetheless, the impact of this assumption on the final weld pool geometry is negligible due to the dominance of the convective over the conductive energy transport, see Section 4.1. A constant mass density is used in the heat conduction simulation as well, see Section 4.4. However, the density value is averaged over the temperature range of interest, between the room temperature and the solidification temperature, resulting in $\rho_{hc} \approx 7700\,\mathrm{kg\,m^{-3}}$. Furthermore, note that for isotropic materials, the volumetric thermal expansion coefficient, β, used in the Boussinesq approximation, is defined as three times the linear coefficient of thermal expansion, β' [151]. Here, β' is taken from measurements performed with S355J2G3 steel sheets [149, 150]. As seen in Figure 4.10, β' varies only slightly with temperature, and therefore a constant value is used in the weld pool simulation. All constant thermophysical material properties of the unalloyed steel used in the models are summarized in Table 4.3.

The temperature coefficient of the surface tension, defined as the derivative of the surface tension with respect to the temperature, $\mathrm{d}\gamma'/\mathrm{d}T$, is of particular importance for the weld pool simulation. The surface tension, γ', is a function of the temperature and the chemical activity of the dissolved surface-active substances such as oxygen (O) and S [152]. According to [135], the surface tension of most pure metals, including iron and steels with low O and S contents, decreases with increasing temperature, resulting in a negative derivative. When the content of O or S is higher than 60 ppm, the temperature coefficient of the surface tension is positive. As pointed out in [153], systems with a positive temperature coefficient of the surface tension must go through a maximum at a certain temperature, and hence have a negative temperature coefficient of the surface tension at higher temperatures. According to [AC7], the maximum value of 0.035 wt. % or 350 ppm sulfur allowed by the standard leads

Table 4.3: Constant thermophysical material properties of the unalloyed S355J2+N steel [146–150, 152]

Material property	Symbol	Value	Unit
Melting temperature	T_{melt}	1750	K
Melting interval	$T_{\mathrm{melt}} \pm \Delta T$	1750 ± 50	K
Evaporation temperature	T_{ev}	3100	K
Linear coeff. of thermal expansion	β'	$1.5 \cdot 10^{-5}$	K^{-1}
Volumetric coeff. of thermal expansion	β	$4.5 \cdot 10^{-5}$	K^{-1}
Latent heat of solidification	H_{f}	$2.47 \cdot 10^{5}$	$\mathrm{J\,kg}^{-1}$
Marangoni coefficient	$\mathrm{d}\gamma'/\mathrm{d}T$	$-4.3 \cdot 10^{-4}$	$\mathrm{N\,m}^{-1}\,\mathrm{K}^{-1}$
Mass density at liquidus temperature	ρ_{liq}	7700	$\mathrm{kg\,m}^{-3}$
Mass density (heat conduction)	ρ_{hc}	7300	$\mathrm{kg\,m}^{-3}$

to local alterations in the weld pool dynamics, resulting in a more pronounced bulging region. Nonetheless, as the sulfur amount in the material used in the present work is lower than 100 ppm, see Section 3.1, the dependence of the surface tension on the thermodynamic activity, and thus on the numerically predicted weld pool geometry is neglected and a constant temperature coefficient of the surface tension is used instead, see Table 4.3.

All phase or material-specific properties were taken from the literature [102, 146, 149, 150, 152], and if these were not available, which was the case for the dynamic viscosity, the values for pure iron were used due to the close chemical composition [147, 148].

4.6.2 Thermomechanical Material Properties

According to [106], the material models used in computational welding mechanics to predict the temporal and residual stresses, as well as the distortion of the welded components, include the temperature-dependent material properties and the material responses induced by temperature changes, such as strain hardening and SSPTs. The strain hardening in the monotonic flow stress-strain curve of the ferritic S355 steel has been found to be significant, see [154]. Furthermore, the SSPTs are shown to play a crucial role in the formation of residual stresses for low-alloyed and unalloyed ferritic steels, such as the S355J2+N steel used in the present work, see [103]. Therefore, the material model used in the mechanical simulation considers both the strain hardening and the SSPTs.

Temperature-Dependent Material Properties

The material properties, which depend only on the temperature and not on the solution of the mechanical model are Poisson's ratio, the mass density, Young's modulus, and the thermal strain. However, for steel, the mass density decreases, and the Poisson's ratio increases only slightly with increasing temperature [155]. Therefore, it is a common practice

to use constant values in the mechanical simulation [156]. Here, a Poisson's ratio of 0.3 is used and the change of the mass density with temperature is considered by the thermal strain, see Figure 4.11. The values of the thermal strain have been determined at heating and cooling rates typical for LBW of thick S690QL steel sheets [6]. Since there are only minor differences between the Young's modulus of the considered phases [102, 146], in the current model, the Young's modulus of the ferrite phase is used. This has been implemented as temperature-dependent and is shown in Figure 4.11.

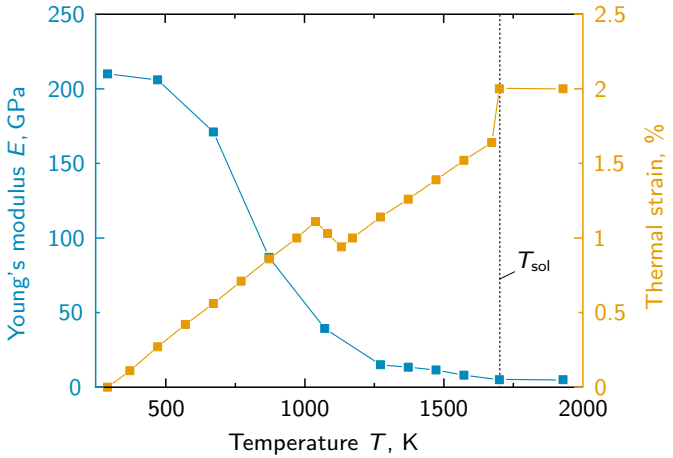

Figure 4.11: Young's modulus and thermal strain of the unalloyed S355J2+N steel [146, 149, 150]

Strain Hardening

An isotropic strain hardening is assumed in the material model of the unalloyed structural S355J2+N steel. This is modeled as temperature-dependent and phase-specific, as shown in Figure 4.12, using stress-strain curves of the ferrite and austenite phases taken from [102, 146]. It is well-known that metals begin to soften at elevated temperatures. For example, the softening temperature for mild steel is around 600 °C. At this temperature, the material reaches a stage where the flow stress approaches zero. Therefore, stress-strain curves with an assumed constant flow stress of 5 MPa for $T > 1100\,°C$, i.e., representing perfect plasticity, are used in the mechanical simulation.

In addition, as recommended in [146], the Young's modulus is further reduced in the high-temperature range to emulate that material is structurally absent and obtain a converging solution in the soft liquid metal, see Figure 4.11. However, this adaption alone does not lead to realistic results since it only allows the material around the weld pool to deform freely without being influenced by the structurally weaker liquid metal. Once the material

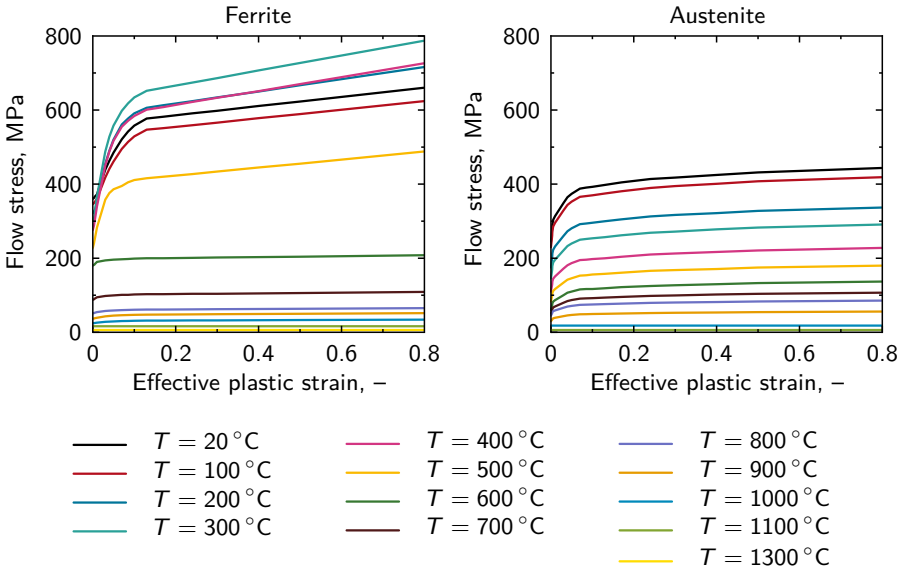

Figure 4.12: Stress-strain curves of the unalloyed S355J2+N steel [102, 146]

cools below the melting temperature, its elastic stiffness increases again, leading to a sudden increase in the stresses. In reality, the material should start solidifying in a state of zero stress since the crystal lattice is destroyed during melting. Therefore, all melted elements are "deactivated" with the feature "activation" available in the commercial finite element analysis software COMSOL Multiphysics 5.4® [122]. Thereby, to emulate that the material is not present, the entries of the corresponding melted elements in the elasticity matrix are lowered by a scale factor of 10^{-6}. Furthermore, the initial stresses are set to zero at the instant of activation, and the elastic strain is removed from the total strain. Note that the inelastic and effective plastic strains are generally not removed by the "activation" feature. Nevertheless, the material is always activated in a state of zero stress, even if it undergoes multiple activation or deactivation events [128].

Solid-State Phase Transformations

With regard to Section 4.6.1, the microstructure of the unalloyed structural steel S355J2+N undergoes transformations during heating and cooling, resulting in a final mixed microstructure consisting of different phases, and thus having locally different mechanical properties. Typically, the $\Delta t_{8/5}$ in LBW processes is very short and, according to measurements performed on 15 mm thick unalloyed steel sheets, S460NH, lies in the range of 1 s to 2 s [6, 157]. Hence, diffusion-controlled transformations do not or hardly occur, and the material

transforms diffusionless into martensite as seem in the continuous cooling transformation diagram shown in Figure 4.13 [145]. This allows using a comparatively simple SSPTs model in the mechanical simulation, in which the base metal transforms completely to austenite during heating, and subsequently, the austenite transforms completely into martensite during cooling. Thereby, the $\alpha \rightarrow \gamma$ transformation occurring during heating is determined only by A_3 as in the weld pool simulation, see Section 4.6.1. Furthermore, the study of the influence of the temporal strain and stress evolution in the bulging region on solidification cracking, which occur at high temperatures [7, 35], does not require the consideration of the transformation to martensite, as this starts at approximately $M_s = 410\,^{\circ}C$ [145]. In other words, when the cracks are formed, there is either no or only a very narrow, and therefore negligible region of the martensite phase. Hence, the metallurgical strain due to the martensite phase transformation is set to zero in Equation (4.20). Note, however, that when the goal is to predict the welding residual stresses, these simplifications can not be made [158, 159], and the non-diffusion transformation to martensite needs to be considered in the material model.

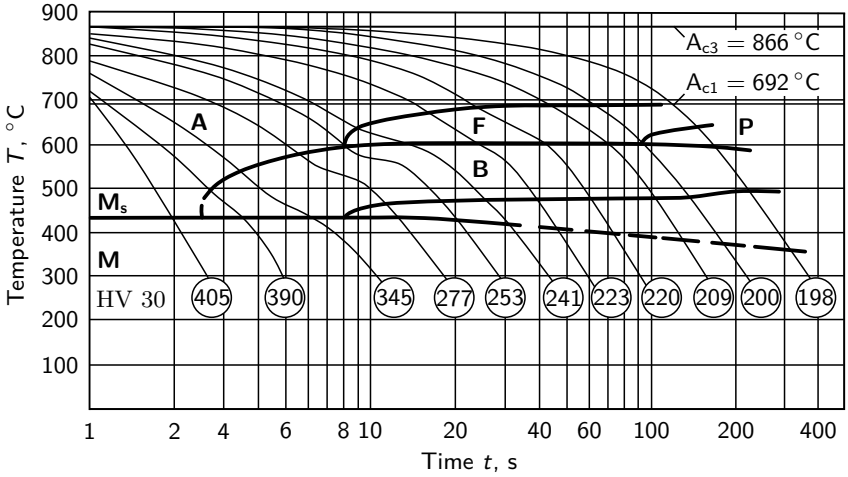

Figure 4.13: Continuous cooling transformation diagram ($T_{peak} = 1350\,^{\circ}C$) of the unalloyed St 355 T steel, according to [145]

5 Results

This chapter summarizes all experimental, analytical, and numerical results. In the following sections, it is distinguished between results supporting the presence of the bulging region during complete penetration LBW, results used for verification and validation of the developed multiphysics mathematical framework presented in Chapter 4, and results obtained with the framework for the analysis of the influence of the bulging region on the susceptibility to centerline solidification cracking.

5.1 Real-Time Visualization of the Bulging Region

In Figure 5.1, two frames obtained with a high-speed camera at different positions along the steel-glass interface are shown. The experiments were performed with the 15 mm thick S355J2+N steel sheets based on the parameters given in Table 3.3. The bright region seen in the figures was visualized in real-time. This region contains a mixture of liquid metal and metallic vapor, giving a qualitative representation of the geometry of the keyhole and the weld pool, marked in the figure by the red and yellow lines, respectively. The keyhole's position and geometry were found and approximated from the known position of the laser beam and the dark solid areas, assumed to be visible through the metallic vapor filling the keyhole. Moreover, a bulging region was observed in the longitudinal section, occurring approximately at half of the sheet thickness. The bulging region was located at the outer boundary of the weld pool, and its size and exact position varied with time.

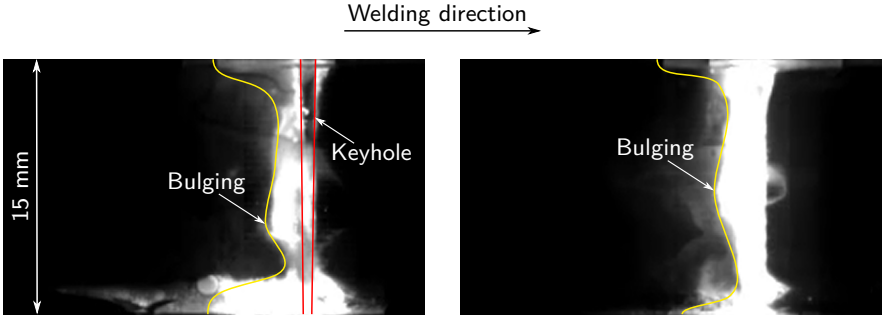

Figure 5.1: View of the longitudinal section through the quartz glass recorded at different times with a high-speed camera

To support the high-speed camera observations, additional measurements were performed using an infrared camera and a thermal camera recording simultaneously from the glass side. Based on the measured intensities shown in Figure 5.2, a bulging region was recognized with both cameras. By comparing the locations of the bulging region recorded with the different cameras, see Figures 5.1 and 5.2, it can be seen that these corresponded well with each other, being located approximately in the middle of the weld pool. Moreover, also an observation of a bulging region located outside the weld pool was made, as depicted in Figure 5.2. This observation gives further evidence for the occurrence of a bulging region during high power LBW since a bulging of the weld pool is expected to lead to a bulging of the isotherms of lower temperatures located behind it.

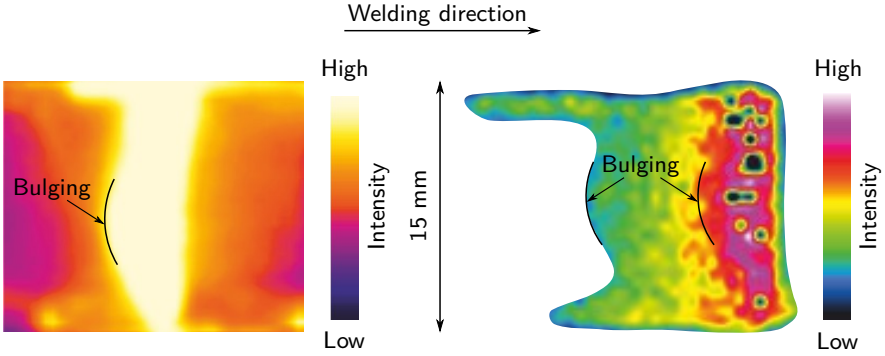

Figure 5.2: View of the longitudinal section through the quartz glass recorded with (left) a thermal camera and (right) an infrared camera

5.2 Experimental Measurements for Validation of the Models

5.2.1 Measurements on 12 mm Thick Unalloyed S355J2+N Steel Sheets

In Figure 5.3, an exemplary metallographic cross-section and recorded thermal cycles, corresponding to the case of 12 mm thick laser beam welded unalloyed S355J2+N steel sheets, are shown. The thermal cycles were measured on the top and bottom surfaces of the processed steel sheets and their positions were A(47 ± 5 mm, 1.42 ± 0.2 mm, 0 mm) at the top surface and B(47 ± 5 mm, 2.3 ± 0.2 mm, 12 mm) at the bottom surface.

5.2.2 Measurements on 2 mm Thick Austenitic 316L Steel Sheets

In Figure 5.4, the final weld seam of the 2 mm thick laser beam welded austenitic 316L steel sheets from which the metallographic cross-sections and the weld end crater were extracted, are shown. An exemplary metallographic cross-section and an additional horizontal section

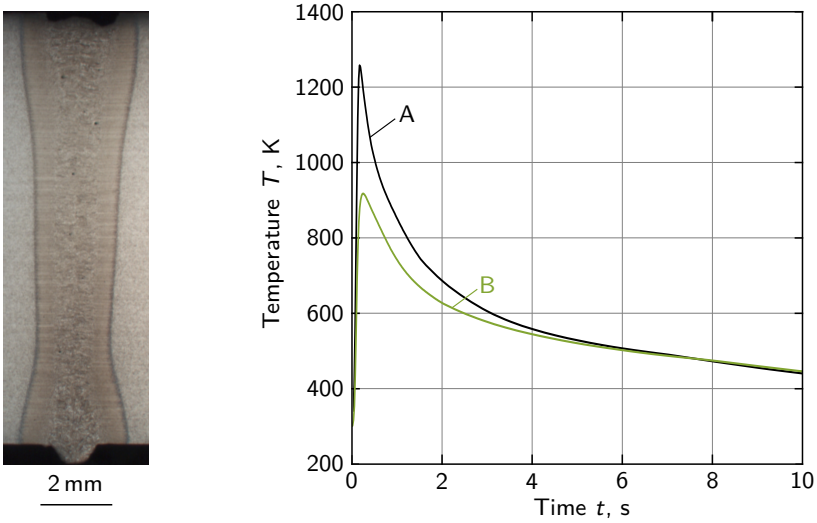

Figure 5.3: (left) Metallographic cross-section of the 12 mm thick S355J2+N steel sheets, extracted at the middle of the weld seam; (right) temperature measurements on the top (A) and bottom (B) surfaces of the specimen

taken from the top surface can be seen in Figure 5.5. According to the assumptions made in Section 4.3, the shape and size of the rear part of the weld end crater, see enlarged view in Figure 5.4, determine the solidification direction of the columnar crystals. As seen in Figure 5.5, the metallographic cross-section shows parallel flanks of the FZ, thus indicating a two-dimensional temperature field, which does not change in the thickness direction. Furthermore, it can be seen from the horizontal section on the top surface that the crystals grow nearly parallel to each other, intersecting the fusion line and the weld centerline at a constant angle. In addition, the weld pool rear part can also be recognized in the macro section by the so-called ripples, i.e., solidification lines representing the local weld pool geometry at the time of solidification.

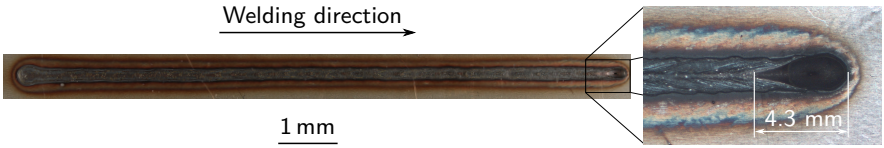

Figure 5.4: (left) Weld seam on the top surface of the 2 mm thick 316L steel sheets before extraction of macro sections; (right) an enlarged view of the weld end crater

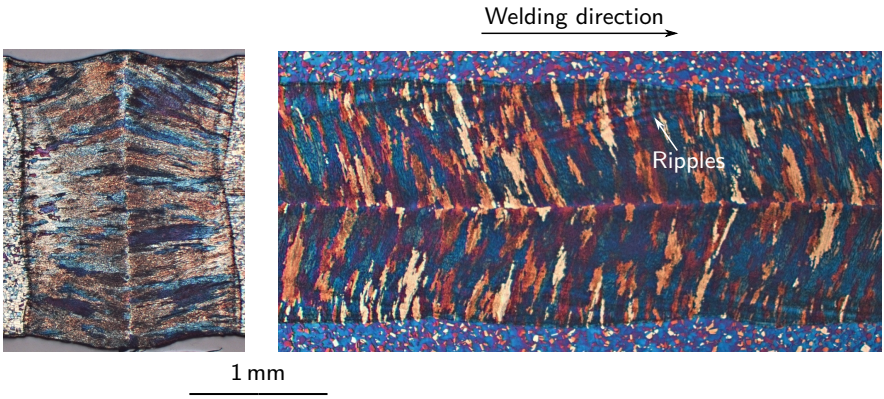

Figure 5.5: (left) Metallographic cross-section of the 2 mm thick 316L steel sheets, extracted at the middle of the weld seam; (right) horizontal section extracted from slightly below the top surface

5.3 Weld Pool Simulation

In Figure 5.6, a side, front, and top view of the numerically predicted three-dimensional weld pool geometry, described by the isosurface of the solidus temperature, $T_{sol} = 1700\,K$, are illustrated. The weld pool geometry corresponds to the case of 12 mm thick laser beam welded unalloyed S355J2+N steel sheets. According to Figure 5.6a, the weld pool geometry can be characterized by five regions based on to their dimensions. In particular, three of these regions, namely the top, bulging, and bottom regions, are longer in the welding direction compared to the two regions located between them. The front view of the three-dimensional weld pool geometry is shown in Figure 5.6b. A closer look at the solidus isotherm, i.e., the outer contour line of the FZ, indicates that the differences in length along the thickness direction correlate strongly with the differences in width. Specifically, the regions with higher weld pool lengths are wider than those with shorter weld pool lengths. As depicted in the figure, the maximum weld pool length is found on the top surface of the welded steel sheets. This is estimated from the top view of the weld pool geometry depicted in Figure 5.6c to approximately 5.2 mm. Accordingly, the maximum weld pool width is found on the top surface as well, being approximately 1.35 mm. By combining the different views of the weld pool geometry, it can be seen that the dimensions of the FZ gradually decrease between the bulging and the two narrow regions located above and below it and increase in the neighboring top and bottom regions. Furthermore, it is observed that all regions narrow near the rear part of the weld pool, forming two narrow channels connecting the larger top and bottom regions to the bulging region.

In addition to the solidus isotherm, the numerically calculated melting and liquidus isotherms, where $T_{melt} = 1750\,K$ and $T_{liq} = 1800\,K$, are shown in Figure 5.7. Moreover,

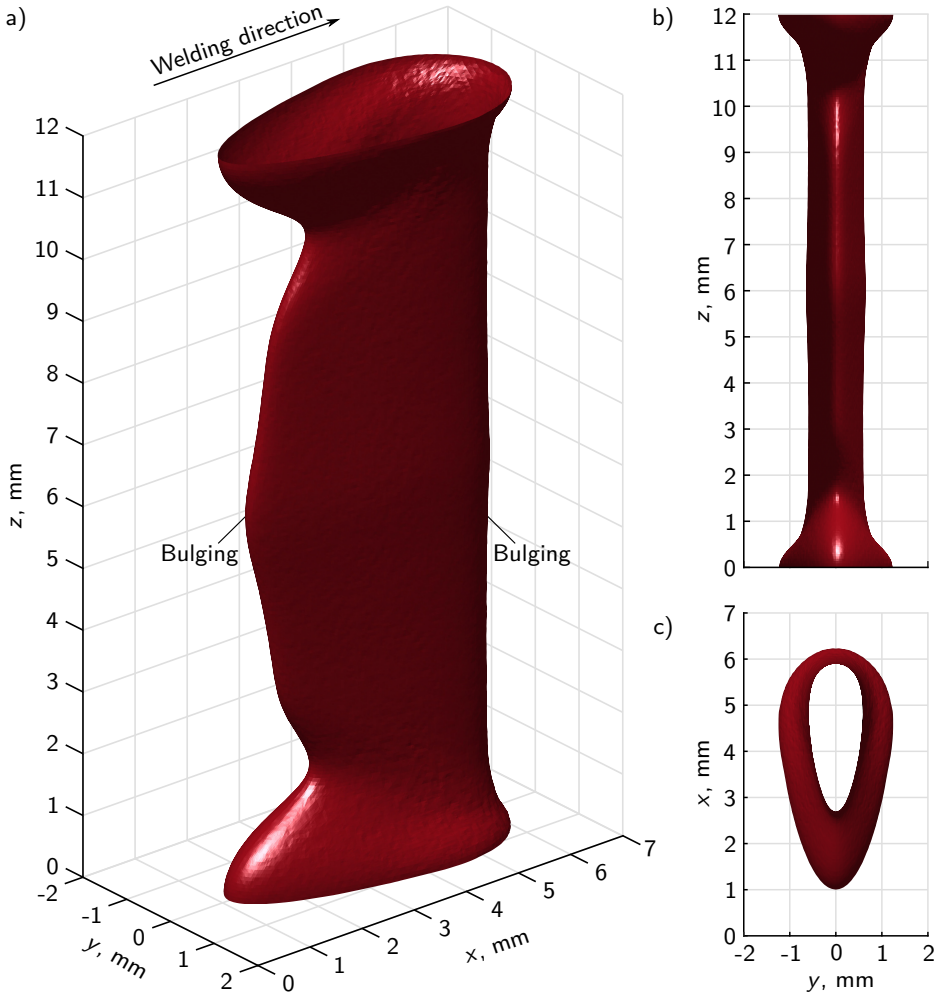

Figure 5.6: Calculated weld pool geometry, defined by the solidus isosurface: a) three-dimensional side view, b) front view, and c) top view

the corresponding predicted temperature distribution in the longitudinal section represented by several isotherms, including the isotherms shown in the cross-section, is illustrated in Figure 5.8. As seen in the figures, the five weld pool regions can be determined by following

the solidus isotherm from the top to the bottom surface along the thickness of the steel sheet and marking the local extremes, i.e., the positions of the local maximum and minimum length or width of the FZ. The distance between the solidus and liquidus isotherm determines the dimensions of the mushy zone. Furthermore, this distance is directly related to the magnitude of the local temperature gradient, and hence to the amount of energy transferred through the solidus isosurface of the weld pool to the solid metal around it by conduction, see Figure 5.6a. According to the numerical results, the width of the mushy zone in the cross-section is nearly zero above and below the bulging region located at approximately 6 mm penetration depth. In contrast, the width grows in the top and bottom regions of the weld pool, reaching up to 20% of the local width of the FZ, thus indicating more homogeneous temperature distribution in these regions.

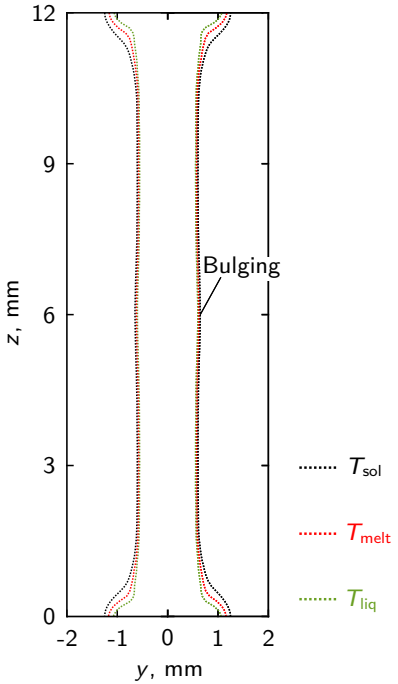

Figure 5.7: Calculated fusion zone, defined by the solidus, melting, and liquidus isotherms

A closer look at the isotherms in the longitudinal section depicted in Figure 5.8 indicates that the length of the mushy zone in the front part of the weld pool changes in the same way along the thickness of the steel sheet as observed for the mushy zone width in the cross-section shown in Figure 5.7. The longest mushy zone region is found in the rear part of

the weld pool at approximately 1.2 mm below the top surface, see Figure 5.8. This increase in the mushy zone length is due to the energy released by the phase transformation from liquid to solid, i.e., the latent heat of solidification. The longer mushy zone indicates that the temperature is homogeneously distributed in the top and bottom regions, as already recognized by the isotherms in the cross-section.

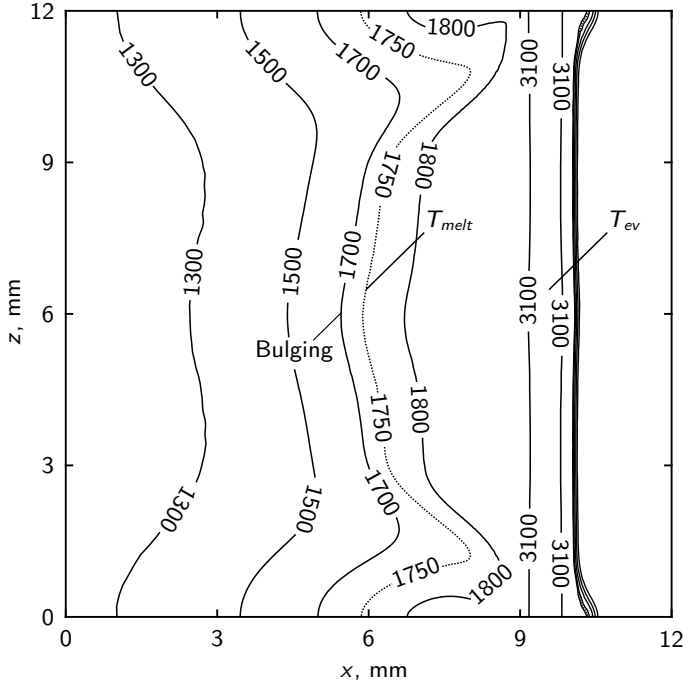

Figure 5.8: Calculated temperature isotherms in the longitudinal section

To obtain further insights into the weld pool dynamics leading to the numerically estimated three-dimensional steady-state weld pool geometry shown in Figure 5.6a, the corresponding calculated velocity fields are analyzed. The velocity fields are given relative to the solid metal, i.e., the difference between the computed fluid velocity and the welding velocity, in the longitudinal section as well as in three exemplary horizontal sections of the weld pool geometry, i.e., sections parallel to the top surface of the welded steel sheets, see Figures 5.9 and 5.10. According to the velocity distributions depicted in the figures, the highest velocities lie in the top and bottom weld pool regions, with the maximum velocity of approximately 869 mm s^{-1} found on the top surface in the vicinity of the keyhole rear surface. The top and bottom regions are strongly influenced by the thermo-capillary convection, which induces

large-scale circulation flows, and thus leads to locally stronger heat and mass transport from the keyhole surface to the solidus isosurface of the weld pool. Consequently, the amount of heat and liquid metal in these regions increases, resulting in the elongation and widening of the solidus isotherm, and hence in the predicted larger steady-state dimensions of these regions. Moreover, the maximum velocities are found not right behind the keyhole rear surface but approximately 0.5 mm behind it. In contrast, the bulging and the narrow regions are rather slow-flowing regions. The maximum velocity in these regions are also found close to the keyhole surface, resulting from the acceleration of liquid metal around it. However, these are one order of magnitude lower than the maximum velocities reached on the top and bottom surfaces of the welded steel sheets. According to Figure 5.10, there is a second main flow in the horizontal sections of the bulging and the narrow regions, which is forward-directed and starts from the rear weld pool end. In the bulging region, the forward-directed flow is a pure result of the movement of the keyhole relative to the solid metal around it. Hence, it has much lower momentum than the backward-directed flow around the keyhole.

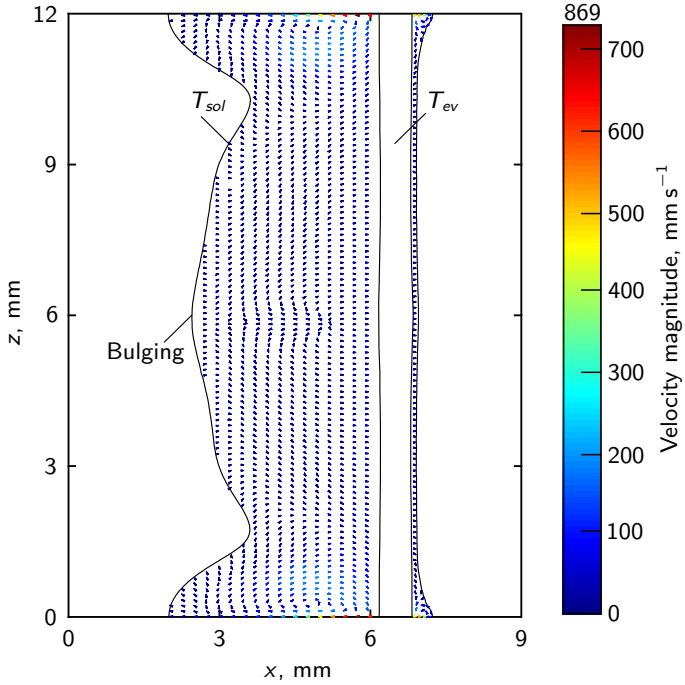

Figure 5.9: Calculated velocity field in the longitudinal section relative to the solid, $\mathbf{u} - \mathbf{v}_{\mathbf{weld}}$

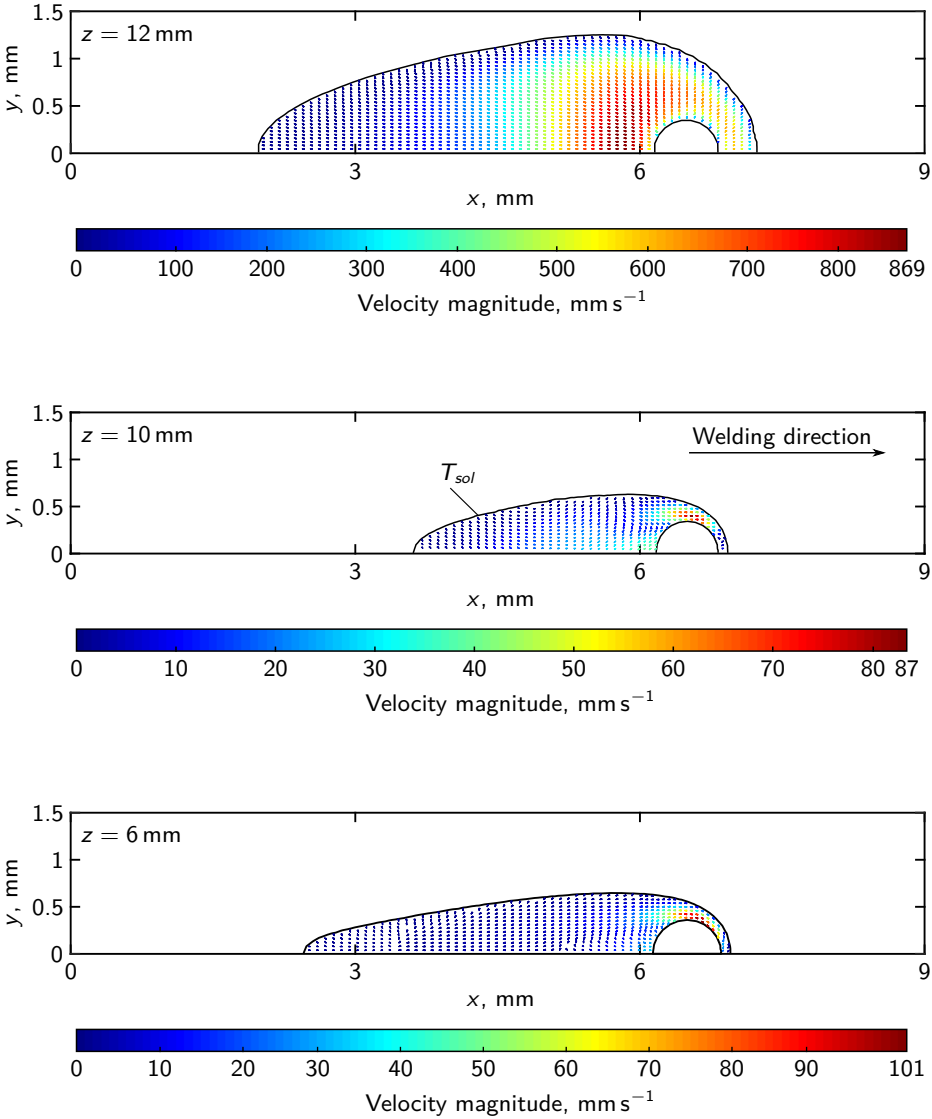

Figure 5.10: Calculated velocity fields in three horizontal sections of the weld pool, defined at $z = 12\,\mathrm{mm}$, $z = 10\,\mathrm{mm}$, and $z = 6\,\mathrm{mm}$, relative to the solid, $\mathbf{u} - \mathbf{v}_{\mathbf{weld}}$

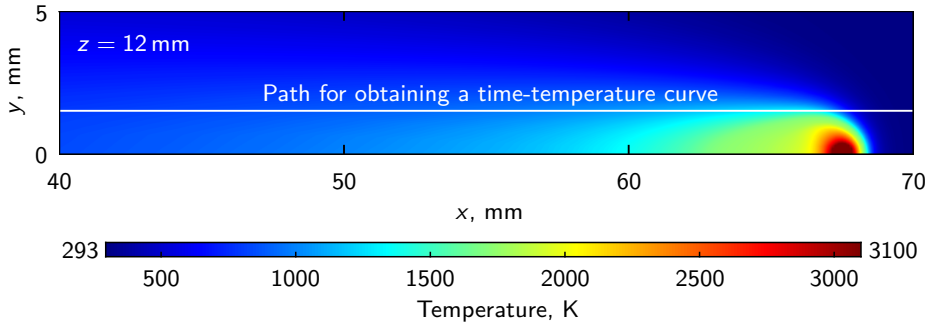

Figure 5.11: Calculated temperature distribution on the top surface and exemplary path used to obtain a time-temperature curve

To validate the calculated temperature distribution, several thermal cycles are computed based on the obtained numerical results. For this purpose, paths parallel to the welding direction are defined along the top and bottom surfaces of the computational domain, as exemplarily depicted in Figure 5.11. The paths have different distances from the weld

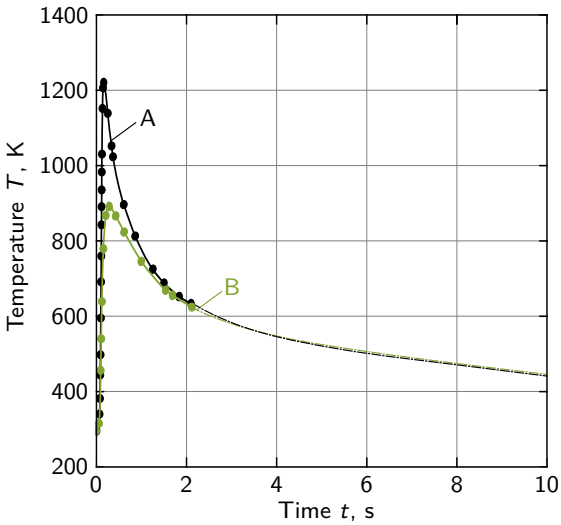

Figure 5.12: Calculated thermal cycles on the top (A) and bottom (B) surfaces of the 12 mm *thick S355J2+N steel sheets*

centerline, i.e., the x-axis. Although the obtained numerical results represent a steady-state solution to the thermo-fluid dynamics problem, a transient thermal cycle can be computed by defining the time as $t = x/v_{\mathrm{weld}_x}$. Here, two thermal cycles are computed, one on the top surface at a distance A = 1.58 mm and one on the bottom surface at a distance B = 2.1 mm, see Figure 5.12. Considering that the length of the computational domain is 70 mm, see Section 4.1.2, the total time of the calculated thermal cycles is around 2 s. This is sufficiently long for the analysis since the temperature at $t = 2\,\mathrm{s}$ is approximately 600 K, and thus the γ-phase transformation has already occurred.

5.4 Lamé Curves Approximation of the Weld Pool Geometry

5.4.1 Derivation of the Lamé Curves Approximation

As described in Section 4.2, discretized data points defining the solidus isosurface are extracted from the solution of the thermo-fluid dynamics problem and subsequently utilized to approximate the three-dimensional weld pool geometry. In the first step, the data is divided into K total levels, i.e., horizontal sections taken along the height, h, of the weld pool, as schematically represented in Figure 4.5. Thereby, the number of horizontal sections must be sufficient to obtain a good approximation. Therefore, it is recommended to take at least one horizontal section at any z-coordinate where the solidus lines in the longitudinal section and the cross-section have a turning point. Then, for each local level, k, two Lamé curves are used to approximate the data points, one for the front and one for the rear part of the weld pool. Here, it is required that at each level the two approximating curves have the same maximum width, b. In the general case, each two Lamé curves are determined by eight parameters and given as follows:

$$\left(\frac{|x - x_{\mathrm{c}}(z)|}{a_{\mathrm{r}}(z)}\right)^{m_{\mathrm{r}}(z)} + \left(\frac{|y|}{b(z)}\right)^{n_{\mathrm{r}}(z)} = 1 \quad \text{for } x < x_{\mathrm{c}};\ m_{\mathrm{r}}, n_{\mathrm{r}} > 1, \tag{5.1}$$

$$\left(\frac{|x - x_{\mathrm{c}}(z)|}{a_{\mathrm{f}}(z)}\right)^{m_{\mathrm{f}}(z)} + \left(\frac{|y|}{b(z)}\right)^{n_{\mathrm{f}}(z)} = 1 \quad \text{for } x \geq x_{\mathrm{c}};\ m_{\mathrm{f}}, n_{\mathrm{f}} > 1, \tag{5.2}$$

where $x_{\mathrm{c}}(z)$ is the center of the corresponding Lamé curve, $m_{\mathrm{r,f}}(z)$ and $n_{\mathrm{r,f}}(z)$ are the shape parameters, $a_{\mathrm{r,f}}(z)$ are the semi-major axes, representing the approximated length of the rear and front parts of the weld pool, denoted by the subscripts r and f, respectively, and $b(z)$ is the semi-minor axis, representing the approximated half-width of the weld pool. It is important to note that the parameters vary along the z-axis and are therefore expressed as functions of the z-coordinate. Nevertheless, for the sake of simplicity, the dependence of the shape parameters on the z-coordinate is not explicitly given in the following equations, i.e., m_{r} is used instead of $m_{\mathrm{r}}(z)$ for example. In addition, to guarantee symmetry and smoothness of the approximated weld pool geometry, both Lamé curves at each local level, k, must be

continuous. If the Lamé curves are mathematically defined as functions of the x-coordinate, this requirement is met when the following conditions are fulfilled:

$$\begin{aligned} \mathrm{d}y/\mathrm{d}x &= 0 \qquad && \text{at } y = \pm b \,(\text{points B and D}), \\ \mathrm{d}y/\mathrm{d}x &= \pm\infty \qquad && \text{at } x = -a_\mathrm{r} \,(\text{point A});\ x = a_\mathrm{f} \,(\text{point C}). \end{aligned} \tag{5.3}$$

Note that the conditions given in Equation (5.3) can be also defined for the derivative $\mathrm{d}x/\mathrm{d}y$ when the Lamé curves are mathematically defined as functions of the y-coordinate.

In theory, to obtain all eight parameters $(a_\mathrm{r}, a_\mathrm{f}, b, x_\mathrm{c}, m_\mathrm{r}, n_\mathrm{r}, m_\mathrm{f}, n_\mathrm{f})$, at least eight data points are needed. Here, the Lamé curves are fitted to the discretized data points using the least square method. The two-dimensional contours at each depth, $z_k = \text{const.}$, are obtained by minimizing the following objective function:

$$F\left(a_i(z), b(z), x_\mathrm{c}(z), m_i(z), n_i(z)\right) = \sum_{l=1}^{L_{\mathrm{tot}_i}} w_l \left(y_l - b\left(1 - \left(\frac{|x_\mathrm{l} - x_\mathrm{c}|}{a_i}\right)^{m_i}\right)^{\frac{1}{n_i}} \right)^2 \to \min \quad \text{for } i = \mathrm{f}, \mathrm{r}, \tag{5.4}$$

where i is an index variable used to switch between the front and rear part of the weld pool, L_tot is the total number of data points at the corresponding level, k, l is the index variable of the data points at this level, and w_l is a weighting factor. The minimum error is determined by equating the partial derivatives of Equation (5.4) with respect to each of the eight parameters to zero:

$$\frac{\partial F}{\partial a_i} = \frac{-2bm_i}{L_{\mathrm{tot}_i} n_i a_i^{m_i+1}} \sum_{l=1}^{L_{\mathrm{tot}_i}} w_l \left[y_l - b\left(1 - \left(\frac{|x_\mathrm{l} - x_\mathrm{c}|}{a_i}\right)^{m_i}\right)^{\frac{1}{n_i}} \right] \times \times \left(1 - \left(\frac{|x_\mathrm{l} - x_\mathrm{c}|}{a_i}\right)^{m_i}\right)^{\frac{1-n_i}{n_i}} |x_\mathrm{l} - x_\mathrm{c}|^{m_i} \stackrel{!}{=} 0, \tag{5.5}$$

$$\frac{\partial F}{\partial b} = \frac{-2}{L_{\mathrm{tot}_i}} \sum_{l=1}^{L_{\mathrm{tot}_i}} w_l \left[y_l - b\left(1 - \left(\frac{|x_\mathrm{l} - x_\mathrm{c}|}{a_i}\right)^{m_i}\right)^{\frac{1}{n_i}} \right] \times \times \left(1 - \left(\frac{|x_\mathrm{l} - x_\mathrm{c}|}{a_i}\right)^{m_i}\right)^{\frac{1}{n_i}} \stackrel{!}{=} 0, \tag{5.6}$$

$$\frac{\partial F}{\partial x_\mathrm{c}} = \frac{-2bm_i}{L_{\mathrm{tot}_i} n_i a_i^{m_i}} \sum_{l=1}^{L_{\mathrm{tot}_i}} w_l \left[y_l - b \left(1 - \left(\frac{|x_\mathrm{l} - x_\mathrm{c}|}{a_i} \right)^{m_i} \right)^{\frac{1}{n_i}} \right] \times \\ \times \left(1 - \left(\frac{|x_\mathrm{l} - x_\mathrm{c}|}{a_i} \right)^{m_i} \right)^{\frac{1-n_i}{n_i}} |x_\mathrm{l} - x_\mathrm{c}|^{m_i - 1} \stackrel{!}{=} 0, \quad (5.7)$$

$$\frac{\partial F}{\partial m_i} = \frac{2b}{L_{\mathrm{tot}_i} n_i a_i^{m_i}} \sum_{l=1}^{L_{\mathrm{tot}_i}} w_l \left[y_l - b \left(1 - \left(\frac{|x_\mathrm{l} - x_\mathrm{c}|}{a_i} \right)^{m_i} \right)^{\frac{1}{n_i}} \right] \times \\ \times \left(1 - \left(\frac{|x_\mathrm{l} - x_\mathrm{c}|}{a_i} \right)^{m_i} \right)^{\frac{1-n_i}{n_i}} |x_\mathrm{l} - x_\mathrm{c}|^{m_i} \log \left(\frac{|x_\mathrm{l} - x_\mathrm{c}|}{a_i} \right) \stackrel{!}{=} 0, \quad (5.8)$$

$$\frac{\partial F}{\partial n_i} = \frac{2b}{L_{\mathrm{tot}_i} n_i^2} \sum_{l=1}^{L_{\mathrm{tot}_i}} w_l \left[y_l - b \left(1 - \left(\frac{|x_\mathrm{l} - x_\mathrm{c}|}{a_i} \right)^{m_i} \right)^{\frac{1}{n_i}} \right] \times \\ \times \left(1 - \left(\frac{|x_\mathrm{l} - x_\mathrm{c}|}{a_i} \right)^{m_i} \right)^{\frac{1}{n_i}} \log \left(1 - \left(\frac{|x_\mathrm{l} - x_\mathrm{c}|}{a_i} \right)^{m_i} \right) \stackrel{!}{=} 0. \quad (5.9)$$

Equations (5.5) to (5.9) represent a non-linear system of equations, which has to be solved for each level, k, to obtain the corresponding required shape parameters, and thus has to be repeated K times. Once the values of all eight parameters at each level are known, the missing values between the levels can be estimated by either interpolating between the known values or by fitting these to polynomial functions. For the calculation of the crystal axis, it is necessary to determine the missing values using interpolation of at least second order, i.e., using three or more of the total levels, since the crystals have to be smooth and grow continuously between the levels. However, a first-order interpolation can be used by the description of the EHS in the second simulation sequence, see Figure 4.1, as long as a sufficient total number of levels, K, is used for the approximation of the weld pool geometry. If analytical expressions with continuous first-order derivatives are preferred or needed for the model, polynomial functions dependent on the z-coordinate, i.e., $\left(a_i(z), b(z), x_\mathrm{c}(z), m_i(z), n_i(z)\right)$, can be obtained by fitting a polynomial to the known values, e.g., a polynomial of the form:

$$f(z) = c_0 + c_1 z + c_2 z^2 + \cdots + c_j z^j \quad \text{with} \quad j \leq K - 1, \quad (5.10)$$

where $c_0, \ldots, c_j$ are constant coefficients. For the polynomial fitting, the least squares method can be applied again. In this case, the objective function to be minimized is:

$$F\left(f\left(z_k\right)\right) = \sum_{k=1}^{K} w_k \left(f\left(z_k\right) - \left(c_0 + c_1 z_k + c_2 z_k^2 + \cdots + c_j z_k^j \right) \right)^2 \rightarrow \min, \tag{5.11}$$

where w_k is a weighting factor.

The solution algorithm of the non-linear system of equations, Equations (5.5) to (5.9), as well as the polynomial fitting described above, have been implemented in the numerical computing environment and proprietary programming language MATLAB® [160].

5.4.2 Application of the Lamé Curves Approximation

The main task of the Lamé curves is to accurately approximate an arbitrary three-dimensional steady-state weld pool geometry, including geometrical particularities such as the bulging region. According to Chapter 2, the weld pool geometry enables the coupling of the models included in the developed multiphysics mathematical framework, see Figure 4.1, and thus also the study of the influence of the bulging region on the dominant factors controlling the susceptibility to solidification cracking, see Figure 2.2. Therefore, at first, the flexibility of the developed technique is demonstrated in Figure 5.13 by showing various theoretical weld pool geometries approximated with Lamé curves. As seen, for small m and n values, sharper weld pool geometries can be described. Conversely, for high m and n values, any weld pool geometry of a round or rectangular shape can be obtained.

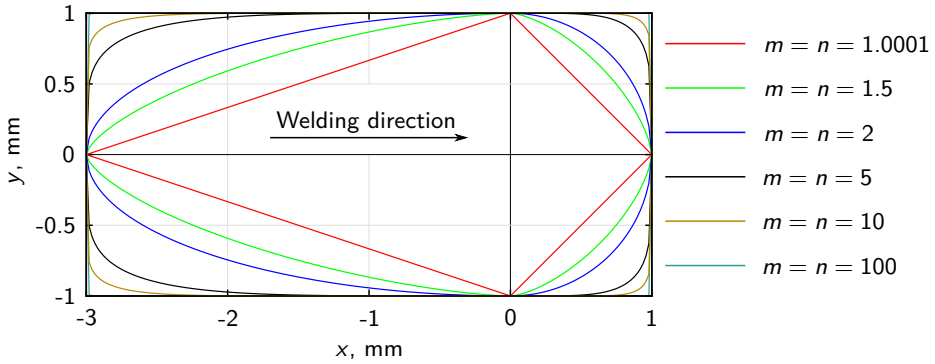

Figure 5.13: Theoretical weld pool geometries of identical dimensions ($a_f = b = 1\,\text{mm}$, $a_r = 3\,\text{mm}$) approximated with Lamé curves for different values of m and n

With regard to Section 4.3, the developed Lamé curves approximation technique is applied on the predicted weld pool geometries of the 2 mm thick austenitic 316L and 12 mm thick unalloyed S355J2+N laser beam welded sheets. According to Figure 5.5, the dimensions of

the FZ change only slightly along the thickness direction of the thin 316L sheets. Hence, the corresponding three-dimensional weld pool geometry can be approximated with only a single layer along the thickness, e.g., the top surface of the joined steel sheets. In the present work, the data points for the approximation are obtained from the ripples recognized in the macro section and from the geometry of the weld end crater depicted in Figure 5.4. The approximated weld pool rear part on the top surface and the corresponding shape parameters are shown in Figure 5.14. Here, the rear length, $a_r = 3.33\,\text{mm}$, and half-width, $b = 0.87\,\text{mm}$, of the weld pool are kept constant, and the values of the shape parameters are varied to find an optimal parameter combination. The values obtained for the shape parameters, $m_r = 1.5$ and $n_r = 1.03$, are comparatively small, indicating a sharp solidification front, which is typical for LBW of thin steel sheets at high process speeds, see Figure 5.5.

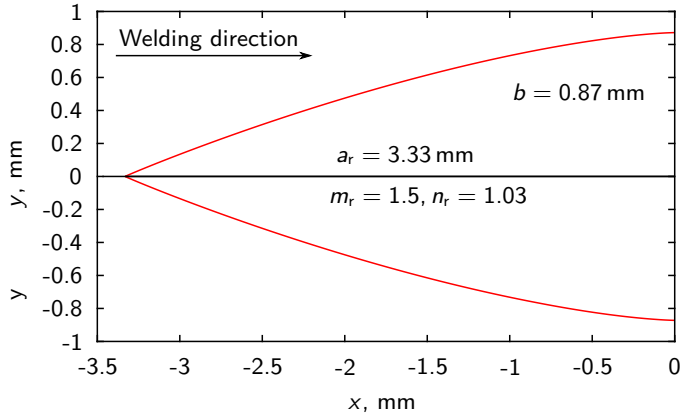

Figure 5.14: Approximation of the weld pool rear part at the top surface of the 2 mm thick 316L sheets, with a single Lamé curve

Furthermore, the three-dimensional steady-state weld pool geometry obtained with the thermo-fluid dynamics model is approximated with Lamé curves and subsequently used in both simulation chains. In the first simulation chain, the approximated weld pool geometry is used to calculate the solidification parameters, in particular, the crystal axis, the growth rate, and the corresponding cross-sectional area of the columnar crystal. In the second simulation chain, however, it is utilized as an EHS. In contrast to the thin 316L steel sheets, the weld pool geometry of the thick S355J2+N steel sheets can not be approximated with a single level along the thickness, see Section 5.3. Hence, the data points extracted from the solution of the weld pool simulation must cover the complete range between to top and bottom surfaces of the welded steel sheets. In Figure 5.15, exemplary projection of data points describing the solidus isosurface onto the $y - z$ plane is shown. The red dots in the figure represent the data points used to approximate the weld pool geometry in the horizontal section through the center of the bulging region. As depicted in the figure, instead

of using only data points lying exactly at $z = 6\,\text{mm}$, data points from slightly above and below were used as well. For the current data set, the thickness of the layer from which data points were taken was defined as 1/1000 of the sheet thickness. A total of 332,605 data points and 25 horizontal sections, distributed evenly between the top and bottom surfaces of the steel sheets, were used to approximate the three-dimensional weld pool geometry, including the bulging region.

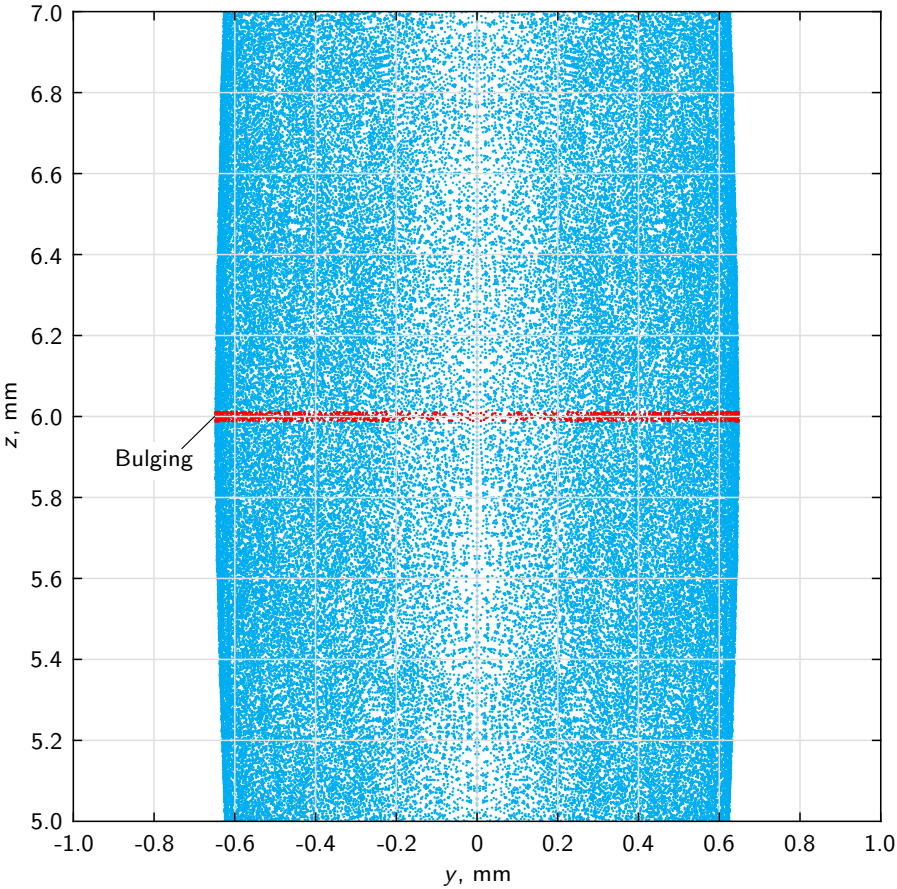

Figure 5.15: Exemplary projection of data points (blue dots) describing the solid isosurface of the three-dimensional weld pool geometry, for $5\,\text{mm} \leq z \leq 7\,\text{mm}$*, onto the* $y - z$ *plane. The red dots represent the data points used to approximate the weld pool geometry in the middle of the bulging region at* $z = 6\,\text{mm}$*.*

Here, the weighting factor, w_k, was set to one since a very high number of evenly distributed data points could be transferred from the weld pool simulation, thus allowing to approximate the weld pool geometry with high accuracy without additional calibration. The Lamé curves were fitted to the discretized data points by using the least square method. For each horizontal section, eight shape parameters describing the front and rear Lamé curves were determined. Subsequently, the missing values between the sections were estimated by fitting polynomial functions to the 25 calculated values. Sixth-degree polynomial functions of the z-coordinate were used for the fitting of the shape parameters since the weld pool geometry shows five extremes, i.e., positions of local maximum dimensions of the FZ, see Section 5.3. The polynomial functions are defined as follows:

$$f(z)_i = p_0 + p_1 z + p_2 z^2 + p_3 z^3 + p_4 z^4 + p_5 z^5 + p_6 z^6, \quad i = 1 \dots 8, \tag{5.12}$$

where $f(z)_i$ stands for each one of the shape parameters a_f, a_r, b, x_c, m_f, n_f, m_r, and n_r. The polynomial constants used to fit the polynomials to the calculated values of the shape parameters are given in Table 5.1. The fitted polynomial functions are illustrated in Figure 5.16.

Table 5.1: Constants used to fit the polynomials to the eight shape parameters

	p_0	p_1	p_2	p_3	p_4	p_5	p_6
a_f	1.7153	-0.6011	0.1672	-0.0108	-0.0013	1.7941e-4	-5.0323e-6
a_r	3.6744	-1.3472	0.4991	-0.0583	0.0012	1.0658e-4	-2.4541e-6
b	1.2597	-0.8417	0.4117	-0.1008	-0.0133	-9.2178e-4	2.5749e-5
x_c	4.4839	-0.1291	-0.0919	0.0577	-0.0108	8.4607e-4	-2.3591e-5
m_f	2.0739	-0.0774	0.3179	-0.1164	0.0173	-0.0011	2.8898e-5
n_f	1.9732	0.2214	-0.1569	0.0453	-0.0061	3.9719e-4	-9.9806e-6
m_r	1.5041	0.9653	-0.9778	0.3333	-0.0521	0.0038	-1.0544e-4
n_r	1.8974	0.1163	-0.0523	0.0102	-0.0012	8.8991e-5	-2.9458e-6

The results show that the five extremes of the corresponding solidus isosurface located at approximately $z = 12\,\mathrm{mm}$, $z = 10\,\mathrm{mm}$, $z = 6\,\mathrm{mm}$, $z = 2\,\mathrm{mm}$, and $z = 0\,\mathrm{mm}$, see Section 5.3, are accurately represented by the polynomial functions. It is also observed from the figures that the parameters a_f and a_r accurately reconstruct the front and rear part of the solidus isotherm in the longitudinal section shown in Figure 5.8. The same holds for the parameter b, which reconstructs the solidus isotherm in the cross-section, see Figure 5.7. Furthermore, exemplary approximation results at three horizontal sections are shown in Figure 5.17. According to the results, the parameters m_r and n_f remain nearly constant and vary slightly around 2 along the sheet thickness. In contrast, the parameters m_f and n_r

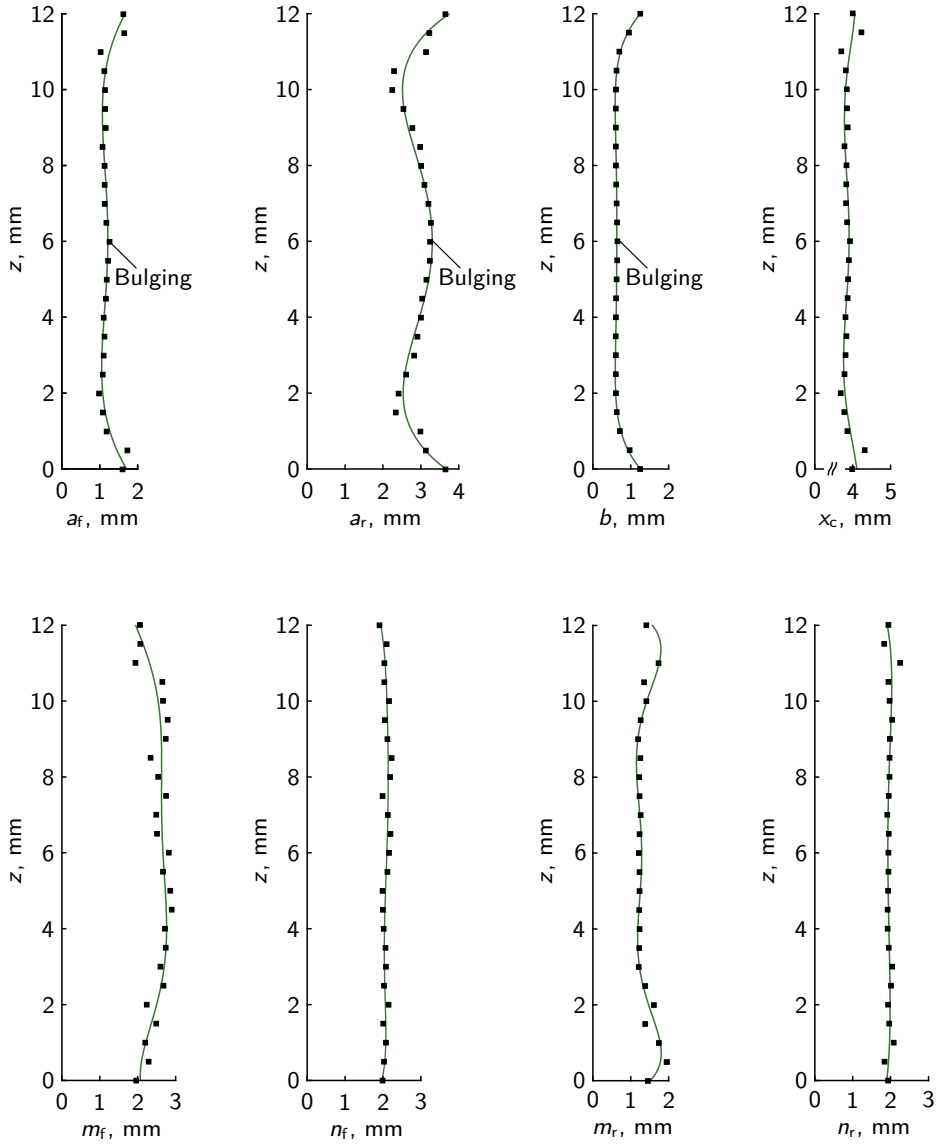

Figure 5.16: Calculated shape parameters for each of the 25 horizontal sections (black rectangles) and sixth-degree polynomial functions fitted to these (green lines)

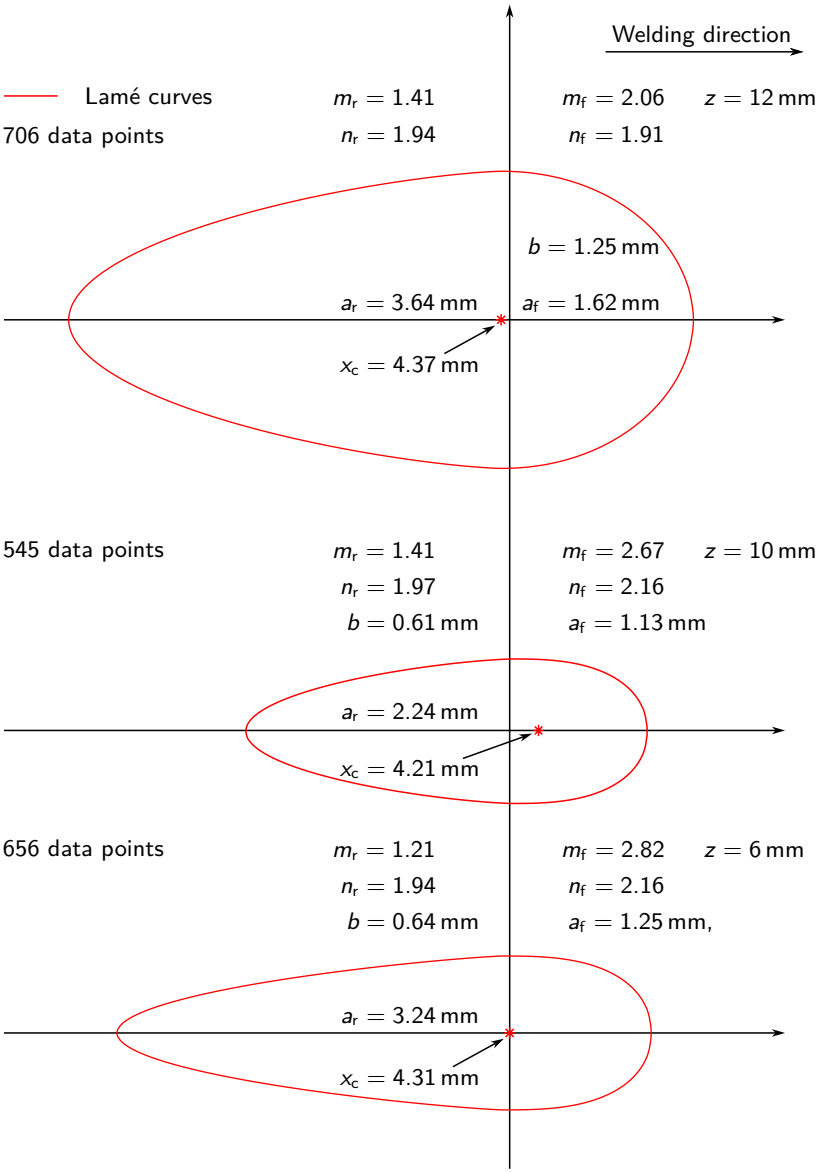

Figure 5.17: Approximation of the weld pool geometry in three horizontal sections of the 12 mm thick S355J2+N sheets, defined at (top) $z = 12\,\text{mm}$, (middle) $z = 10\,\text{mm}$, and (bottom) $z = 6\,\text{mm}$, with Lamé curves

take values in the range between 1 and 3, giving the final shape of the front and rear part of the two-dimensional solidus isotherms in the horizontal sections of the weld pool geometry, see Figure 5.17.

Another interesting observation is made about the parameter describing the center of the two Lamé curves. As illustrated in the figures, x_c varies along the sheet thickness as well. This allows to describe the local heating process more accurately since heating and cooling of the joined steel sheets starts at different times along the thickness direction, e.g., the top and bottom regions will be heated first, see Figure 5.6. Additionally, the various initial points along the welding trajectory from which the crystals start growing are automatically considered by x_c, as this represents their corresponding x-coordinates, see Figure 4.6.

5.5 Solidification of a Steady-State Weld Pool Geometry

5.5.1 Derivation of General Analytical Expressions for the Main Solidification Parameters in 2D

The solidification process is considered two-dimensional when the dimensions of the three-dimensional weld pool geometry change only slightly along the thickness direction of the steel sheet. Typically, this is the case for complete penetration LBW of thin steel sheets at high processing speeds. However, in the case of complete penetration LBW of thick steel sheets, this is also true in the middle of the bulging region and near the top and bottom surfaces of the joined steel components.

Referring to Figure 4.6 and the assumptions made in Section 4.3, the general analytical expressions for the three main solidification parameters are derived as follows:

- Columnar crystal axis

The movement of the solidification front can be described by a family of Lamé curves, $\phi(x, x_c, y)$, located along the x-axis:

$$\phi(x, x_c, y) = \left(\frac{x - x_c}{a_r}\right)^m + \left(\frac{y}{b}\right)^n - 1 = 0 \tag{5.13}$$

or

$$\frac{x - x_c}{a_r} = \left(1 - \left(\frac{y}{b}\right)^n\right)^{\frac{1}{m}} \rightarrow x_{Lamé}(y) = x_c + a_r \left(1 - \left(\frac{y}{b}\right)^n\right)^{\frac{1}{m}}. \tag{5.14}$$

Here, x_c is the center of the moving Lamé curve, accounting for the total distance along the x-axis by which the curve is moved from the origin of the Cartesian coordinate system; m and n are the shape parameters of the Lamé curve approximating the rear part of the weld pool; a_r and b are the semi-major axes corresponding to the length and the half-width of the weld pool rear part, respectively, see Section 4.2. As it is assumed that the crystal grows along the temperature gradient, i.e., in the normal inward direction to the solidification front,

the family of curves representing the crystal axes is composed of the orthogonal trajectories of the family of Lamé curves. Hence, both families constitute a double orthogonal system of curves, which in the general case can be analytically determined by solving the following PDE [161]:

$$\frac{\partial \phi}{\partial y}\mathrm{d}x = \frac{\partial \phi}{\partial x}\mathrm{d}y. \tag{5.15}$$

Substituting the partial derivatives of Equation (5.13) into Equation (5.15) results in:

$$\mathrm{d}x = \frac{mb}{na_\mathrm{r}}\left(1-\left(\frac{y}{b}\right)^n\right)^{\frac{m-1}{m}}\left(\frac{y}{b}\right)^{1-n}\mathrm{d}y. \tag{5.16}$$

An indefinite integration of Equation (5.16) on both sides and a rearrangement of the terms gives:

$$x_\mathrm{crystal}(y) = \frac{mb^{\frac{n}{m}}}{na_\mathrm{r}}\int\left(b^n - y^n\right)^{\frac{m-1}{m}} y^{1-n}\mathrm{d}y + \text{constant}. \tag{5.17}$$

The solution of Equation (5.17) yields the equation of the crystal axis for $n \neq 2$:

$$x_\mathrm{crystal}(y) = \frac{mb^n y^{2-n}}{na_\mathrm{r}(n-2)}\,{}_2F_1\left(\frac{1}{m}-1, \frac{2}{n}-1; \frac{2}{n}; \left(\frac{y}{b}\right)^n\right) + \text{constant}, \tag{5.18}$$

where ${}_2F_1$ is the hypergeometric function [162]. The constant in Equation (5.18) can be determined using the initial condition for the crystal axis, which requires that the crystal length at $y = \pm b$ is zero, see Figure 4.6. Hence, the final columnar crystal axis equation for $n \neq 2$ reads:

$$x_\mathrm{crystal}(y) = \frac{mb^n}{na_\mathrm{r}(n-2)}\left(y^{2-n}\,{}_2F_1\left(\frac{1}{m}-1, \frac{2}{n}-1; \frac{2}{n}; \left(\frac{y}{b}\right)^n\right) - \right.$$
$$\left. - b^{2-n}\,{}_2F_1\left(\frac{1}{m}-1, \frac{2}{n}-1; \frac{2}{n}; 1\right)\right). \tag{5.19}$$

It is worth mentioning that the general crystal axis equation derived above, see Equation (5.17), can be simplified to the solution derived using elliptical functions [39] by substituting $m = n = 2$:

$$x_\mathrm{crystal}(y) = \frac{b^2}{a_\mathrm{r}}\int\frac{\sqrt{1-\left(y/b\right)^2}}{y}\mathrm{d}y + \text{constant}. \tag{5.20}$$

Solving Equation (5.20) analogically to solving equation Equation (5.18) gives the columnar

crystal axis equation for a weld pool geometry with an elliptical rear part:

$$x_{\text{crystal}}(y) = \frac{b^2}{a_r}\left(\sqrt{1-\left(y/b\right)^2} - \ln\left|\left(1+\sqrt{1-\left(y/b\right)^2}\right)/\left(y/b\right)\right|\right). \tag{5.21}$$

- Crystal growth rate

The growth rate, R, of the columnar crystal is defined as the infinitesimal change in length, $\mathrm{d}l$, of the crystal with a total length, l, in the infinitesimal time interval, $\mathrm{d}t$, see Figure 4.6. However, $\mathrm{d}t$ can be determined using the welding speed vector, $\mathbf{v}_{\mathbf{weld}}$, and the distance, $\mathrm{d}x_0$, by which the solidification front moves, see Figure 5.18. Thus, the growth rate can be given as:

$$R = \frac{\mathrm{d}l}{\mathrm{d}t} = \frac{\mathrm{d}l}{\frac{\mathrm{d}x_0}{|\mathbf{v}_{\mathbf{weld}}|}} = |\mathbf{v}_{\mathbf{weld}}|\frac{\mathrm{d}l}{\mathrm{d}x_0} = |\mathbf{v}_{\mathbf{weld}}|\cos\alpha. \tag{5.22}$$

It can be seen in Figure 5.18 that the fraction $\mathrm{d}l/\mathrm{d}x_0$ equals $\cos\alpha$, where α is the angle between the temperature gradient (the normal inward direction to the solidification front) and the moving direction of the Lamé curves (the welding direction). Two methods to determine $\cos\alpha$ by using analytical geometry are described in the following.

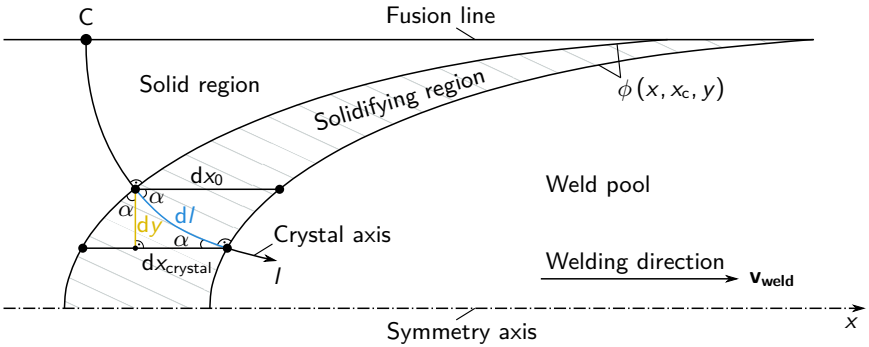

Figure 5.18: Schematic of a two-dimensional columnar crystal growth during movement of a steady-state weld pool geometry used to determine $\cos\alpha$

The first method makes use of the trigonometric relationships between the parameters. A closer look at Figure 5.18 and the relations derived above shows that the angle α is found in at least three triangles. Thus, $\cos\alpha$ can be expressed as:

$$\cos\alpha = \frac{\mathrm{d}l}{\mathrm{d}x_0} = \frac{\mathrm{d}x_{\text{crystal}}}{\mathrm{d}l} = \frac{\mathrm{d}y_{Lamé}}{\sqrt{\mathrm{d}x_{Lamé}^2 + \mathrm{d}y_{Lamé}^2}}. \tag{5.23}$$

Note that $dy = dy_{Lamé} = dy_{crystal}$. Nonetheless, the first two expressions in Equation (5.23) can not be determined analytically and the value of $\cos\alpha$ is obtained by making use of the last expression on the right-hand side and Equation (5.14):

$$\cos\alpha = \frac{1}{\sqrt{1+\left(\frac{dx_{Lamé}}{dy_{Lamé}}\right)^2}}. \tag{5.24}$$

Substituting Equation (5.24) into Equation (5.22) results in the growth rate equation of the columnar crystal:

$$R_{2D} = \frac{|\mathbf{v_{weld}}|}{\sqrt{1+\left(\frac{na_r}{mb}\right)^2\left(1-\left(\frac{y}{b}\right)^n\right)^{\frac{2-2m}{m}}\left(\frac{y}{b}\right)^{2n-2}}}. \tag{5.25}$$

A point worth stressing is that in the three-dimensional case, this approach leads to the following expression for $\cos\alpha$:

$$\cos\alpha = \frac{1}{\sqrt{1+\frac{dx_{Lamé}^2}{dy_{Lamé}^2+dz_{Lamé}^2}}}. \tag{5.26}$$

As noted from Equation (5.26), the denominator can not be evaluated analytically, and therefore no analytical solution for the growth rate of the three-dimensional columnar crystal, R_{3D}, can be derived using trigonometric relationships.

The second method uses the dot product of the normal inward vector to the solidification front, $\mathbf{n}$ (growth direction of the crystal), and the welding direction vector, $\mathbf{v_{weld}}$ (moving direction of the Lamé curves), to determine $\cos\alpha$. In contrast to the approach using trigonometry, this method enables the derivation of analytical expressions for the growth rate in both two and three dimensions. Here, the normal vector is obtained from the curve or surface equation describing the corresponding two-dimensional or three-dimensional weld pool geometry [126]. Thus, $\cos\alpha$ can be expressed as follows:

$$\cos\alpha = \frac{\mathbf{n}\cdot\mathbf{v_{weld}}}{|\mathbf{n}||\mathbf{v_{weld}}|} = \frac{\frac{\partial\phi}{\partial x}v_{\mathrm{weld}_x}+\frac{\partial\phi}{\partial y}v_{\mathrm{weld}_y}+\frac{\partial\phi}{\partial z}v_{\mathrm{weld}_z}}{\sqrt{\left(\frac{\partial\phi}{\partial x}\right)^2+\left(\frac{\partial\phi}{\partial y}\right)^2+\left(\frac{\partial\phi}{\partial z}\right)^2}\sqrt{v_{\mathrm{weld}_x}^2+v_{\mathrm{weld}_y}^2+v_{\mathrm{weld}_z}^2}}. \tag{5.27}$$

Substituting the partial derivatives of Equation (5.13) into Equation (5.27) and taking into account that in the present work $\mathbf{v_{weld}}$ has only a component in the x-direction, Equation (5.25) can be obtained again.

- Cross-sectional area of the crystal

As depicted in Figure 5.19, the cross-sectional area of the columnar crystal will decrease

along the crystal axis depending on its curvature. Thereby, the area at any given point can be calculated using the following relationship:

$$\omega_{cr} = \omega_{cr_0} \sin \alpha, \tag{5.28}$$

where ω_{cr_0} is the initial cross-sectional area of the crystal and α is again the angle between the normal inward direction to the solidification front and the welding direction, see Figure 5.19. To make use of the derived expressions for $\cos \alpha$, Equation (5.28) is reformulated as follows:

$$\omega_{cr} = \omega_{cr_0} \sqrt{1 - \cos^2 \alpha}. \tag{5.29}$$

The final equation of the cross-sectional area in 2D is derived by substituting Equation (5.24) into Equation (5.29):

$$\omega_{cr_{2D}} = \omega_{cr_0} \sqrt{1 - \frac{1}{1 + \left(\frac{na_r}{mb}\right)^2 \left(1 - \left(\frac{y}{b}\right)^n\right)^{\frac{2-2m}{m}} \left(\frac{y}{b}\right)^{2n-2}}}. \tag{5.30}$$

It is worth mentioning that as seen in Equations (5.22) and (5.29), both the growth rate and the cross-sectional area of the columnar crystal depend on $\cos \alpha$, which can be calculated with the two methods proposed above. Thereby, in 2D, both methods lead to the same analytical result. However, in 3D, only the second method can be used to obtain analytical expressions for R and ω_{cr}.

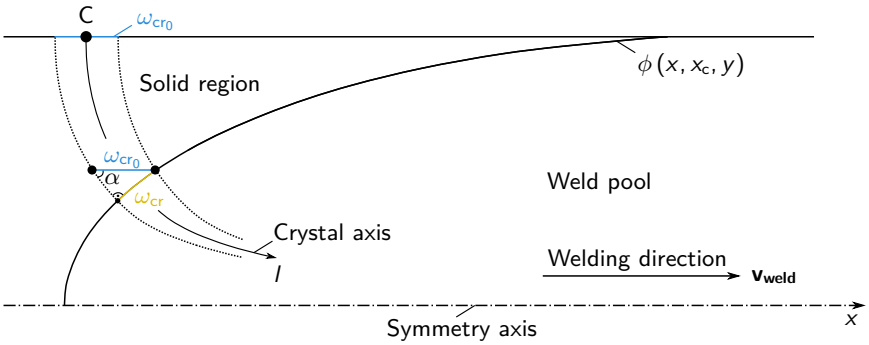

Figure 5.19: Schematic of a two-dimensional columnar crystal growth during movement of a steady-state weld pool geometry used to determine ω_{cr}

5.5.2 Numerical Procedure for the Main Solidification Parameters in 3D

In 3D, the weld pool geometry is approximated not by a single function but by a set of functions dependent on the z-coordinate, see Sections 4.2 and 5.4. Hence, the attempt to

obtain analytical expressions for the three main solidification parameters in 3D, analogically to the derivation in 2D, seems rather impractical compared to the straightforward numerical solution. Therefore, in 3D, the main solidification parameters are computed numerically based on the assumptions stated at the beginning of Section 4.3 and the relationships described in the previous section. The steps involved in the developed numerical procedure are given below.

- Columnar crystal axis

The three-dimensional crystal axis is obtained by determining the intersection points between the columnar crystal and the solidification front, see Figure 5.20. These are found as follows:

(1) Use the Lamé curve approach presented in Section 4.2 to approximate the solidification front (calculated rear part of the 3D weld pool geometry, see Section 4.1) with a function of the following form:

$$\phi\left(x, x_c, y, z\right) = \left(\frac{x - x_c\left(z\right)}{a_r\left(z\right)}\right)^{m(z)} + \left(\frac{y}{b\left(z\right)}\right)^{n(z)} - 1 = 0. \tag{5.31}$$

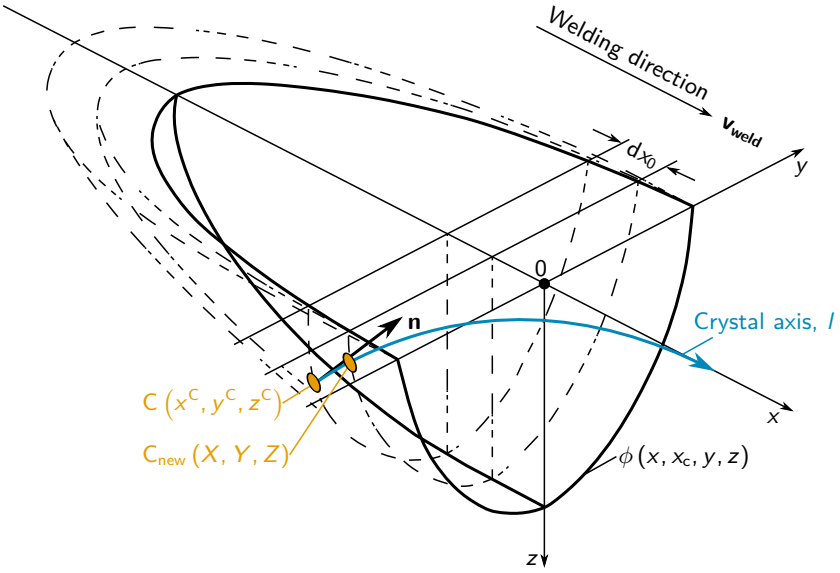

Figure 5.20: Schematic of a three-dimensional columnar crystal growth during movement of a steady-state weld pool geometry

(2) Initialize the computational domain by defining a point C $\left(x^{\mathrm{C}}, y^{\mathrm{C}}, z^{\mathrm{C}}\right)$ where the crystal growth starts, see Figure 5.20.

(3) Move the weld pool geometry along the welding direction by a distance $\mathrm{d}x_0$.

(4) Build the tangent plane at the moved point $\mathrm{C}_{\mathrm{moved}}$ $\left(x^{\mathrm{C}} + \mathrm{d}x_0, y^{\mathrm{C}}, z^{\mathrm{C}}\right)$, i.e., the projection of C onto the $y - z$ plane at $x^{\mathrm{C}} + \mathrm{d}x_0$. According to [126], the tangent plane can be defined as a function of the following form:

$$\phi'_x \left(x - \left(x^{\mathrm{C}} + \mathrm{d}x_0 \right) \right) + \phi'_y \left(y - y^{\mathrm{C}} \right) + \phi'_z \left(z - z^{\mathrm{C}} \right) = 0, \tag{5.32}$$

where ϕ'_x, ϕ'_y, and ϕ'_z are the partial derivatives of Equation (5.31) given as:

$$\phi'_x = \frac{m\left(z\right) \left(\frac{x - x_{\mathrm{c}}(z)}{a(z)} \right)^{m(z)-1}}{a\left(z\right)}, \tag{5.33}$$

$$\phi'_y = \frac{n\left(z\right) \left(\frac{y}{b(z)} \right)^{n(z)-1}}{b\left(z\right)}, \tag{5.34}$$

$$\phi'_z = \left(\frac{x - x_{\mathrm{c}}\left(z\right)}{a\left(z\right)} \right)^{m(z)} \left(\log\left(\frac{x - x_{\mathrm{c}}\left(z\right)}{a\left(z\right)} \right) m'\left(z\right) - m\left(z\right) \frac{a'\left(z\right)}{a\left(z\right)} - \right.$$

$$\left. - \frac{m'\left(z\right) x_{\mathrm{c}}\left(z\right)}{x - x_{\mathrm{c}}\left(z\right)} \right) + \left(\frac{y}{b\left(z\right)} \right)^{n(z)} \left(\log\left(\frac{y}{b\left(z\right)} \right) n'\left(z\right) - n\left(z\right) \frac{b'\left(z\right)}{b\left(z\right)} \right). \tag{5.35}$$

Here the $'$ symbol denotes the partial derivatives of the function, ϕ, and the total derivatives of the shape parameters of the Lamé curves.

(5) Find the coordinates X, Y, and Z of the intersection point $\mathrm{C}_{\mathrm{new}}$ at which a line passing through point C $\left(x^{\mathrm{C}}, y^{\mathrm{C}}, z^{\mathrm{C}}\right)$ passes the tangent plane defined at $\mathrm{C}_{\mathrm{moved}}$ $\left(x^{\mathrm{C}} + \mathrm{d}x_0, y^{\mathrm{C}}, z^{\mathrm{C}}\right)$ perpendicularly. According to [126], the coordinates can be found from the following symmetrical equations:

$$\frac{X - x^{\mathrm{C}} - \mathrm{d}x_0}{\phi'_x} = \frac{Y - y^{\mathrm{C}}}{\phi'_y} = \frac{Z - z^{\mathrm{C}}}{\phi'_z}. \tag{5.36}$$

Note that only two of the three equations are linearly independent. If any of the partial

derivatives is zero, the coordinates of the intersection point simplify to:

$$\phi'_x = 0 \qquad \rightarrow \qquad X = x^{\mathrm{C}} + \mathrm{d}x_0, \tag{5.37}$$

$$\phi'_y = 0 \qquad \rightarrow \qquad Y = y^{\mathrm{C}}, \tag{5.38}$$

$$\phi'_z = 0 \qquad \rightarrow \qquad Z = z^{\mathrm{C}}, \tag{5.39}$$

respectively. If $\phi'_x \neq 0$, $\phi'_y \neq 0$, or $\phi'_z \neq 0$, Equations (5.32) to (5.36) are used to obtain the coordinates of the intersection point:

$$X = x^{\mathrm{C}} + \frac{\phi'_x}{\phi'_z}\left(\frac{\phi'_x\phi'_z}{\phi'^2_x + \phi'^2_y + \phi'^2_z}\right)\mathrm{d}x_0, \tag{5.40}$$

$$Y = y^{\mathrm{C}} + \frac{\phi'_y}{\phi'_z}\left(\frac{\phi'_x\phi'_z}{\phi'^2_x + \phi'^2_y + \phi'^2_z}\right)\mathrm{d}x_0, \tag{5.41}$$

$$Z = z^{\mathrm{C}} + \left(\frac{\phi'_x\phi'_z}{\phi'^2_x + \phi'^2_y + \phi'^2_z}\right)\mathrm{d}x_0. \tag{5.42}$$

(6) Repeat steps 3 to 5 until the crystal axis reaches the weld centerline.

- Crystal growth rate

As described above, the crystal growth rate, R, is defined as the infinitesimal change in length, $\mathrm{d}l$, in the infinitesimal time interval, $\mathrm{d}t$. Numerically, $\mathrm{d}l$ can be determined from the coordinates of the new and the old intersection points. Note that $\mathrm{d}t$ is a model parameter, which must be sufficiently small to obtain converging solution. Hence, the growth rate in 3D is numerically approximated as:

$$R_{3\mathrm{D}} = \frac{\mathrm{d}l}{\mathrm{d}t} = \frac{\sqrt{\left(X - x^{\mathrm{C}}\right)^2 + \left(Y - y^{\mathrm{C}}\right)^2 + \left(Z - z^{\mathrm{C}}\right)^2}}{\mathrm{d}t}. \tag{5.43}$$

- Cross-sectional area of the crystal

The cross-sectional area of the crystal axis is numerically determined by approximating the analytical expression given in Equation (5.29) as follows, see also Equation (5.23):

$$\omega_{\mathrm{cr}_{3\mathrm{D}}} = \omega_{\mathrm{cr}_0}\sqrt{1 - \left(\frac{\mathrm{d}l}{\mathrm{d}x_0}\right)^2}, \tag{5.44}$$

where ω_{cr_0} is the initial cross-sectional area of the crystal. Making use of the previously

determined intersection points, Equation (5.44) is expressed as follows:

$$\omega_{\mathrm{cr}_{3\mathrm{D}}} = \omega_{\mathrm{cr}_0} \sqrt{1 - \left(\frac{\sqrt{\left(X - x^{\mathrm{C}}\right)^2 + \left(Y - y^{\mathrm{C}}\right)^2 + \left(Z - z^{\mathrm{C}}\right)^2}}{\mathrm{d}x_0} \right)^2} . \tag{5.45}$$

According to Equations (5.40) to (5.45), the accuracy of the numerically obtained solidification parameters depends on the distance, $\mathrm{d}x_0$, by which the solidification front is moved. Hence, to ensure numerical stability and independence of the obtained solutions on the algorithm, a suitably small $\mathrm{d}x_0$ must be used in the computations. The required value $\mathrm{d}x_0$ can be determined, for example, by performing a convergence analysis or by comparing the numerical solution with an experimental measurement or an analytical solution and reducing $\mathrm{d}x_0$ until the required accuracy is achieved.

5.5.3 Application of the General Expressions to 2D Crystal Growth

In the following, the crystal axis and the growth rate corresponding to the case of 2 mm thick laser beam welded austenitic 316L steel sheets are calculated. Considering the expressions derived in the previous sections and the experimental results presented in Section 5.2, in 2D, the crystal axis can be calculated explicitly by a function dependent on the dimensions and the shape parameters of a single Lamé curve approximating the weld pool rear part, see Section 5.4. For the sake of completeness, the weld pool rear part is described using both a Lamé curve and an elliptical function. However, the dimensions of the semi-major

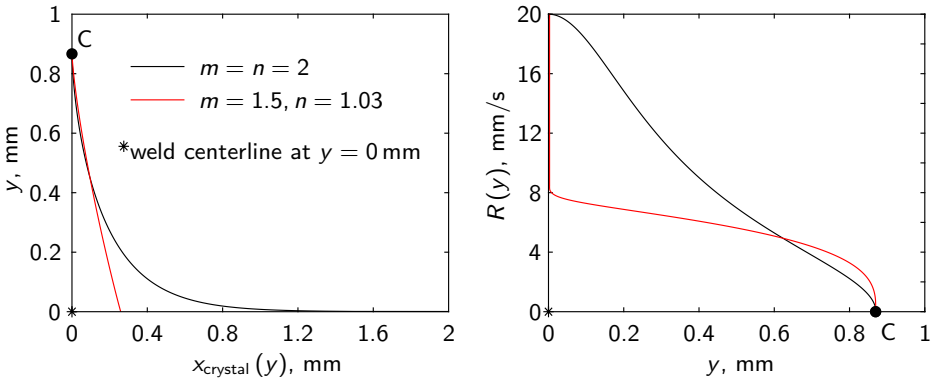

Figure 5.21: Calculated (left) crystal axes, $x_{\mathrm{crystal}}(y)$, and (right) growth rates, $R(y)$, for a two-dimensional weld pool rear part ($a_{\mathrm{r}} = 3.33\,\mathrm{mm}$, $b = 0.87\,\mathrm{mm}$) approximated with a Lamé curve and an elliptical function

and semi-minor axes are kept constant, see Figure 5.14. The calculated crystal axes are shown in Figure 5.21(left). Note that the point on the fusion line from which the crystal starts growing is denoted with "C", as illustrated in Figure 4.6. As seen, the sharper the weld pool rear part, i.e., the shape parameters m_r and n_r are close to one, the shorter the corresponding crystal axis. Hence, the total solidification time of the columnar crystal is shorter as well. This is clearly seen by comparing the x-coordinates at which both crystal axes reach the x-axis. The shorter crystal axis, highlighted by the red line, reaches the weld centerline at approximately $x = 0.26\,\text{mm}$, which is equivalent to approximately 13 ms for the welding speed of $1.2\,\text{m}\,\text{min}^{-1}$, see Chapter 3. On the other hand, when the solidification front is approximated with an elliptical function, the solidification time increases by about five times to approximately 65 ms.

In addition to the calculated crystal axes, the corresponding growth rates are illustrated in Figure 5.21(right). According to the computational results, in both cases, the growth rate increases continuously from $0\,\text{mm}\,\text{s}^{-1}$ at point C to its maximum value of $20\,\text{mm}\,\text{s}^{-1}$, i.e., the welding speed, at the weld centerline. Nonetheless, there are significant differences in the predicted growth rates between these locations. For an elliptical weld pool rear part, the growth rate increases nearly linearly between its minimum and maximum values, except for the regions near the vicinity of the fusion line and the weld centerline. In contrast, when the weld pool rear part is approximated with a Lamé curve, the growth rate increases more rapidly near the fusion line and the weld centerline but remains almost constant in between.

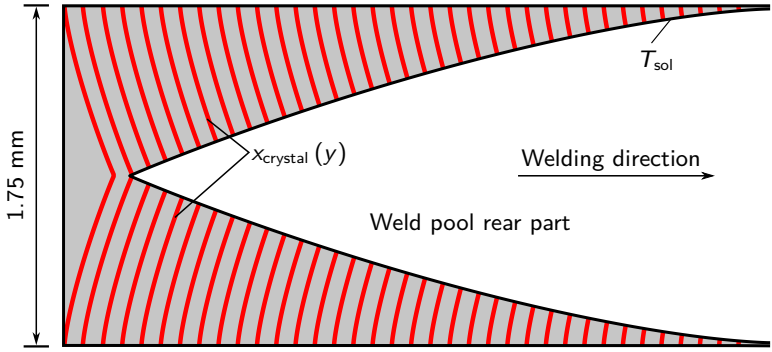

Figure 5.22: Grain structure growing behind the moving weld pool rear part, represented by the calculated crystal axis, $x_{crystal}\,(y)$

Furthermore, the crystal axis calculated for the weld pool rear part approximated with a Lamé curve is used to visualize the grain structure growing behind the moving weld pool as depicted in Figure 5.22. In the figure, the crystal axes are evenly distributed along the fusion line, and their length depends on to the local solidification time. Moreover, the distance between two neighboring crystal axes is defined as the averaged width of the grains observed in the horizontal macro section of the welded steel sheets shown in Figure 5.5.

5.5.4 Application of the Numerical Procedure to 3D Crystal Growth

Here, the developed numerical procedure is first applied to a theoretical case considering a steady-state solidification of a three-dimensional ellipse-shaped weld pool rear part with $a_r = 4\,\text{mm}$ and $b = h = 1\,\text{mm}$. In Figure 5.23, five exemplary crystal axes and the positions from where these start growing are illustrated. The corresponding start positions for the crystal axes 2, 3, 4, and 5 are defined by rotating counterclockwise the start position for the crystal axis 1 around the x-axis by 30°, 45°, 60°, and 90°, respectively. The results indicate that the crystal axes grow three-dimensionally, following the solidification front and converging to the same point located on the top surface of the joined steel sheets, independently on the location from which these start growing.

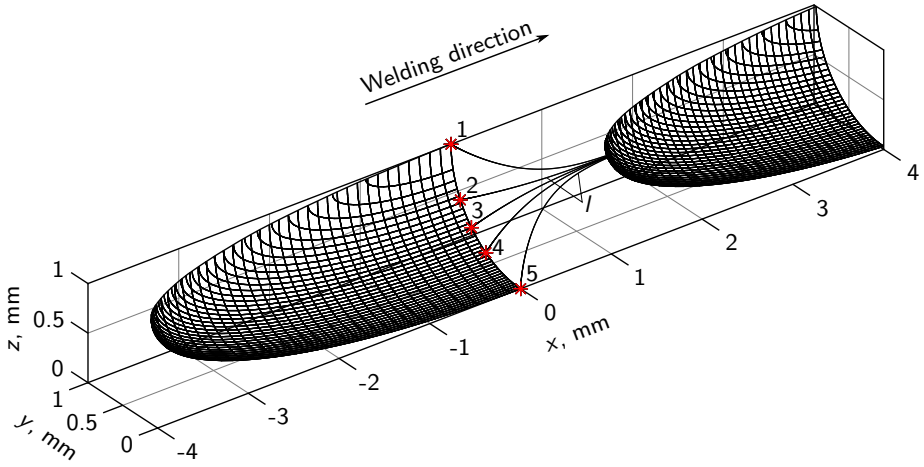

Figure 5.23: Five exemplary crystal axes, l, computed for a steady-state solidification of a three-dimensional ellipse-shaped weld pool rear part ($a_r = 4\,\text{mm}$, $b = 1\,\text{mm}$)

Following the theoretical case, the developed general numerical procedure is applied for the calculation of the three-dimensional crystal axes corresponding to the case of 12 mm thick laser beam welded unalloyed S355J2+N steel sheets. Therefore, the 3D weld pool geometry calculated and approximated with the models presented in Sections 4.1 and 4.2, respectively, has been used as an input parameter. As mentioned at the beginning of Section 5.5, the solidification process can be considered locally as two-dimensional when the width of the FZ remains nearly unchanged along the sheet thickness. By looking at the calculated weld pool geometry, see Figure 5.6, it can be seen that this is the case in the vicinity of the five turning points of the solidus isosurface seen in Figures 5.7 and 5.8, and located at approximately $z = 12\,\text{mm}$, $z = 10\,\text{mm}$, $z = 6\,\text{mm}$, $z = 2\,\text{mm}$, and $z = 0\,\text{mm}$. Since the bulging region is of main interest in the present work, the assumption of local two-dimensional crystal

growth is verified by calculating the crystal axis, *l*, which starts growing at $z = 6$ mm, see Figure 5.24. According to the obtained results, the crystal grows practically in the same horizontal section through the center of the bulging region, i.e., the z-component of the crystal axis changes only slightly from 6 mm to 5.996 mm during the solidification process. Furthermore, it is determined from the figure that during the initial solidification stage the crystal grows predominantly along the y-axis. Once reaching the vicinity of the $x - z$ plane, however, the crystal turns its growing direction into the welding direction.

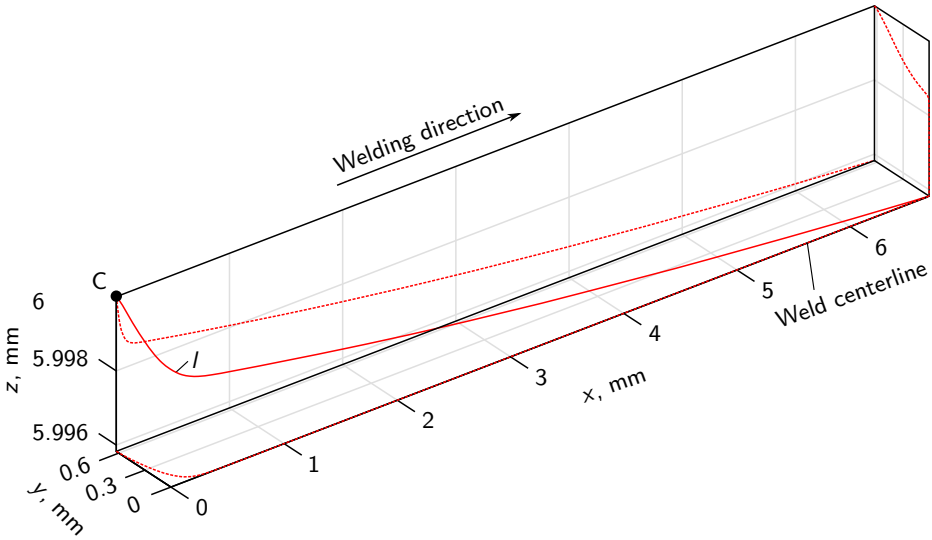

Figure 5.24: Calculated three-dimensional crystal axis, l (red line), with an initial point C located at $z = 6$ mm and corresponding projections onto the orthogonal planes $x - y$, $x - z$, and $y - z$ (red dashed lines). Note the z-axis scale factor of 300.

Two further crystal axes with initial points located above and below the bulging region are calculated and shown in Figures 5.25 and 5.26, respectively. As identified from the figures, both crystal axes grow three-dimensionally, converging into the center of the bulging region located at $z = 6$ mm. The z-component of the crystal axis growing from below the bulging region at $z = 5$ mm increases by approximately 0.6 mm to 5.6 mm. On the contrary, the z-component of the crystal axis growing from above the bulging region at $z = 7$ mm decreases by approximately 0.6 mm to 6.4 mm. Moreover, it is found that similar to the crystal growth in the horizontal section through the center of the bulging region, both crystals grow predominantly along the y-axis during the initial solidification stage. When the crystal axes reach the vicinity of the symmetry plane, however, these turn their direction and continue growing in the welding direction.

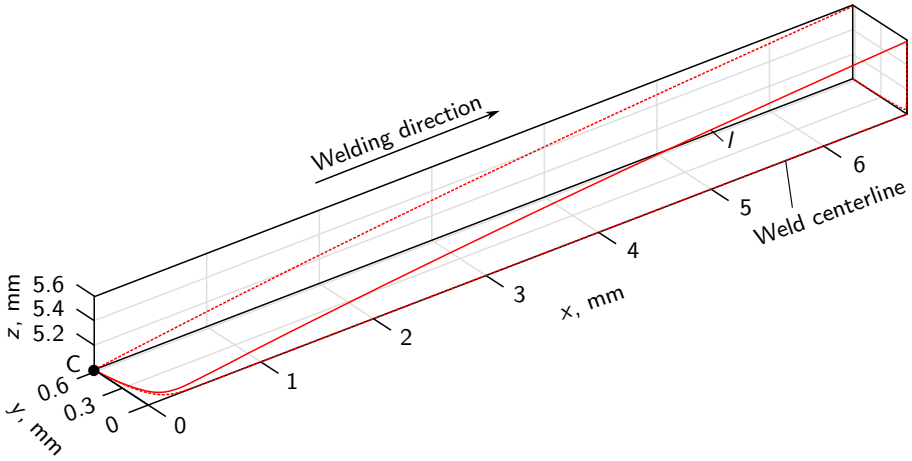

Figure 5.25: Calculated three-dimensional crystal axis, l (red line), with an initial point C located at $z = 5\,\mathrm{mm}$ and corresponding projections onto the orthogonal planes $x - y$, $x - z$, and $y - z$ (red dashed lines)

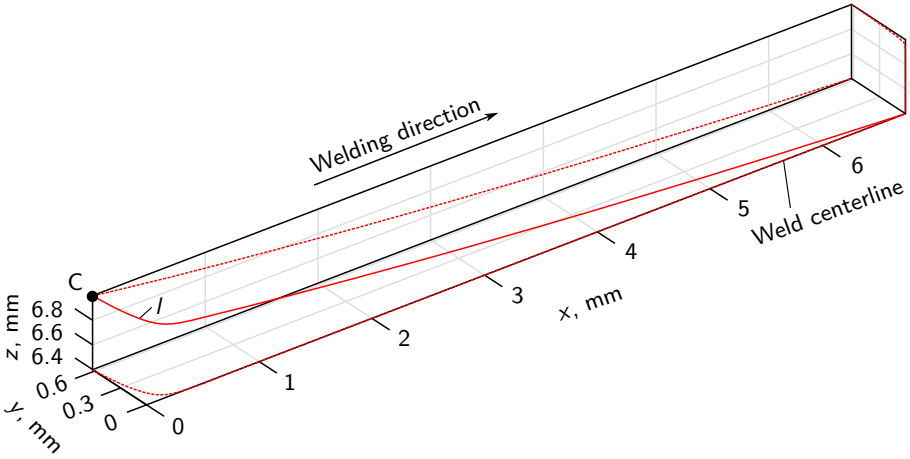

Figure 5.26: Calculated three-dimensional crystal axis, l (red line), with an initial point C located at $z = 7\,\mathrm{mm}$ and corresponding projections onto the orthogonal planes $x - y$, $x - z$, and $y - z$ (red dashed lines)

5.5.5 Dimensionless Analysis of the Main Solidification Parameters

In this section, dimensionless analysis is used to study the dependence of the main solidification parameters on the dimensions and shape of the bulging region, offering additional insights into its influence on the local dwell time of the liquid film residing on the grain boundaries. Therefore, the following dimensionless variables are defined:

$$\xi = \frac{x - x_c}{a_r}, \qquad \eta = \frac{y}{b}, \qquad \Lambda = \frac{a_r}{b}, \qquad \rho = \frac{R}{|\mathbf{v_{weld}}|}, \qquad \omega = \frac{\omega_{cr}}{\omega_{cr_0}}, \tag{5.46}$$

where ξ, η, Λ, ρ, and ω are the x-coordinate, y-coordinate, rear part length to half-width ratio of the bulging region, growth rate, and cross-sectional area of the columnar crystal, respectively. Additionally, for consistency, in this section the dimensionless crystal axis is denoted with l_{dim}.

First, the dependence of the solidification parameters on the dimensions of the bulging region is analyzed. This is done by employing the calculated shape parameters of the weld pool rear part, $m = 1.21$ and $n = 1.94$, see Figure 5.17, and by varying the dimensionless rear part length to half-width ratio, Λ, as depicted in Figure 5.27. Note that the point on the fusion line from which the crystals start growing is denoted with "C", as in Figure 4.6. According to Figure 5.27a, the length and curvature of the crystal axis strongly depend on the dimensions of the bulging region. The results indicate that the crystal axis is longer and less curved when the bulging region is shorter and wider, e.g., $\Lambda = 0.2$, and vice versa. Furthermore, it is seen in Figure 5.27b and Figure 5.27c that the growth rate, ρ, and the cross-sectional area of the crystal, ω, differ significantly for the different dimensions of the bulging region. For an elongated bulging region, ρ and ω experience the highest increase and decrease, respectively, near the weld centerline, i.e., when the dimensionless y-coordinate $\eta \approx 0$. Conversely, when the bulging region is short and wide, the highest increase of ρ and decrease of ω occur near the fusion line.

As next, the dependence of the solidification parameters on the shape of the bulging region is analyzed. This is achieved by varying the parameters m and n of the Lamé curve and keeping the calculated rear part length to half-width ratio of $\Lambda = 5$, see Figure 5.17, constant, as shown in Figure 5.28a. The results depicted in Figure 5.28b suggest that the sharper the solidification front in the bulging region, e.g., $m = n = 1.1$, the shorter the corresponding crystal axis and vice versa. Moreover, a bulging region with a sharp shape results in higher curvature of the crystal axis in the vicinity of the fusion line. Additionally, Figure 5.28c and Figure 5.28d indicate that a sharply shaped bulging region leads to a rapid increase in ρ and decrease in ω near the weld centerline. Conversely, when the shape of the bulging region is smooth and round, e.g., m = n = 2.5, ρ increases approximately linearly between its minimum and maximum values, except for the regions near the fusion line and the weld centerline, whereas ω initially slowly decreases near the fusion line and increases as it approaches the weld centerline.

All results described in this and in the the previous sections have been implemented and evaluated in the numerical computing environment and proprietary programming language MATLAB® [160].

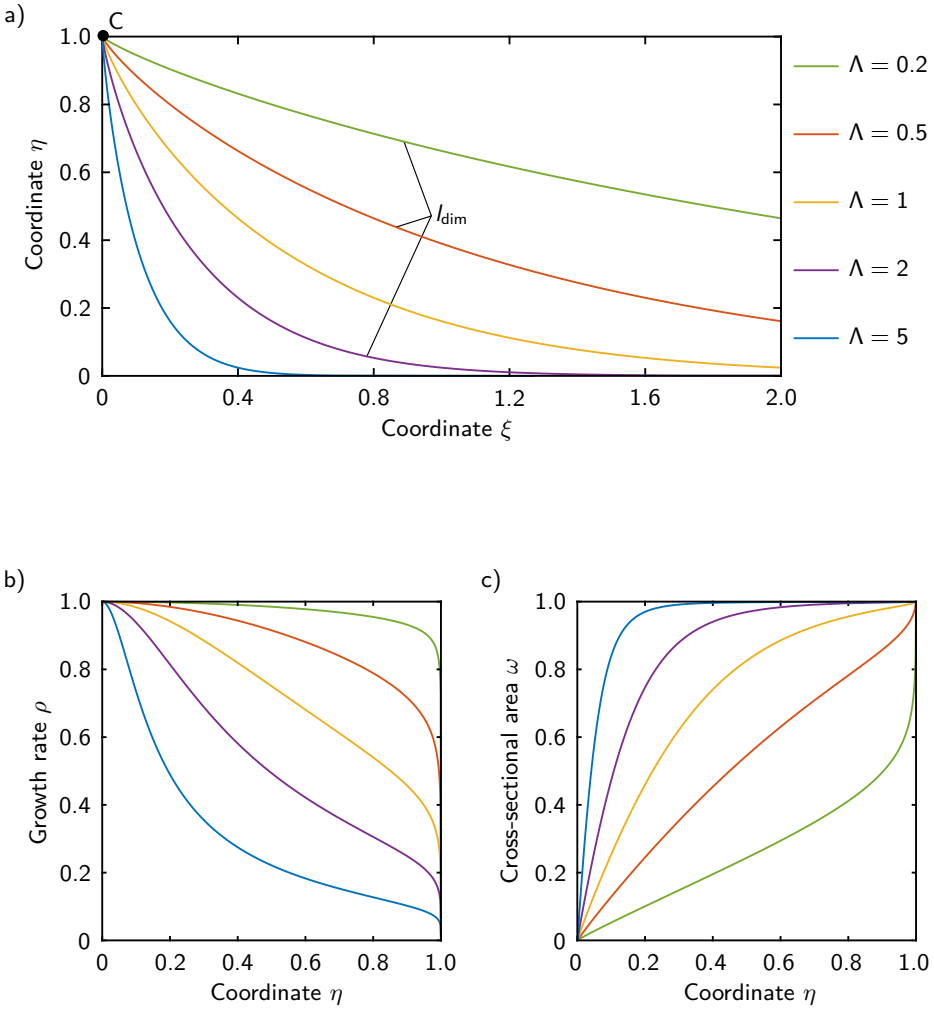

Figure 5.27: Calculated dimensionless solidification parameters for $m_r = 1.21$ and $n_r = 1.94$, and different rear part length to half-width ratios of the bulging region, $\Lambda = a_r/b$: a) crystal axis l_{dim}, b) growth rate ρ, and c) cross-sectional area ω

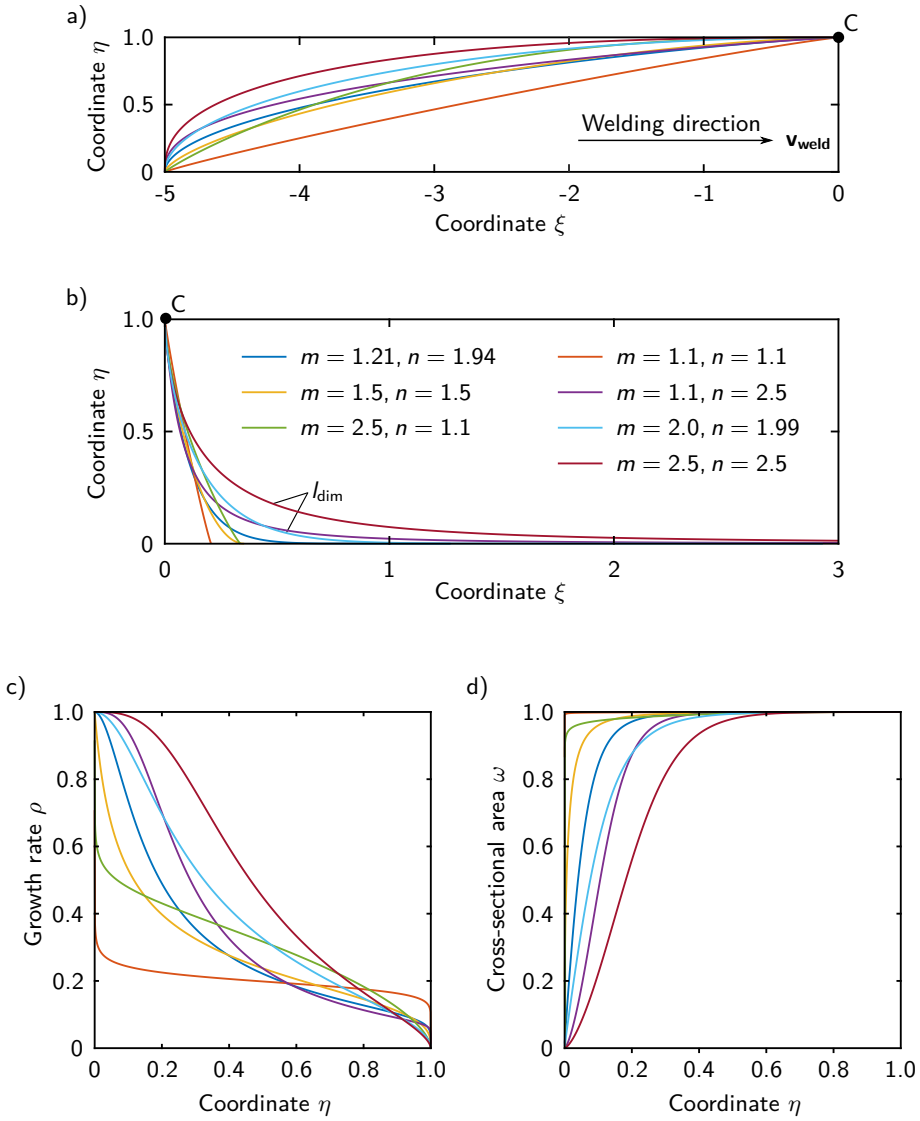

Figure 5.28: Calculated dimensionless solidification parameters for different shapes of the bulging region, i.e., different m and n values, and a constant rear part length to half-width ratio $\Lambda = a_r/b = 5$: a) dimensions and shape of the bulging region, b) crystal axis l_{dim}, c) growth rate ρ, and d) cross-sectional area ω

5.6 Global Heat Conduction Simulation with an Equivalent Heat Source

In the global heat conduction simulation, the approximation of the three-dimensional steady-state weld pool geometry is utilized as an EHS to calculate the transient global temperature field in the plane orthogonal to the welding direction, as described in Section 4.4. In Figure 5.29, the regions identified by the developed algorithm and applied as an EHS, i.e., the temperature of these regions is set to the solidus temperature of the material, are exemplarily illustrated at three points in time. In the present model, the EHS intersects the 2D cross-section for the first time at $t \approx 90\,\text{ms}$. The region found at $t \approx 190\,\text{ms}$ is similar to the FZ obtained numerically by the weld pool simulation, see Figures 5.6 and 5.7. As seen in the figure and described in Section 5.3, the three larger regions of the weld pool, i.e., the top, bulging, and bottom regions, contain the last solidifying liquid metal. The last point in time at which liquid metal is found in the bulging region is at $t \approx 235\,\text{ms}$. By comparing the results at $t \approx 225\,\text{ms}$ and $t \approx 235\,\text{ms}$ shown in Figure 5.29, it can be seen that the algorithm accurately reproduces the high cooling rates typical for the LBW process.

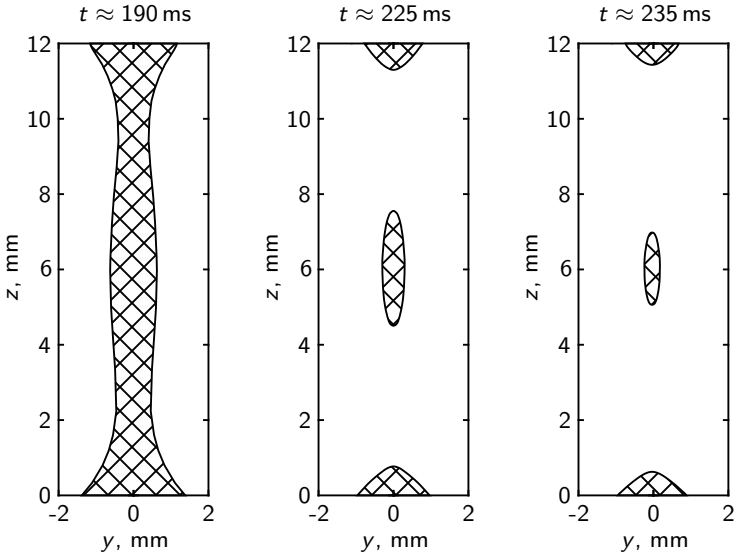

Figure 5.29: Regions found by the algorithm and used as a transient equivalent heat source in the global heat conduction simulation

In addition, the transient two-dimensional temperature distribution is calculated for the time steps analyzed above and shown in Figure 5.30. A closer look at the results confirms the accurately detected regions of the EHS. Moreover, it can be seen that the temperature

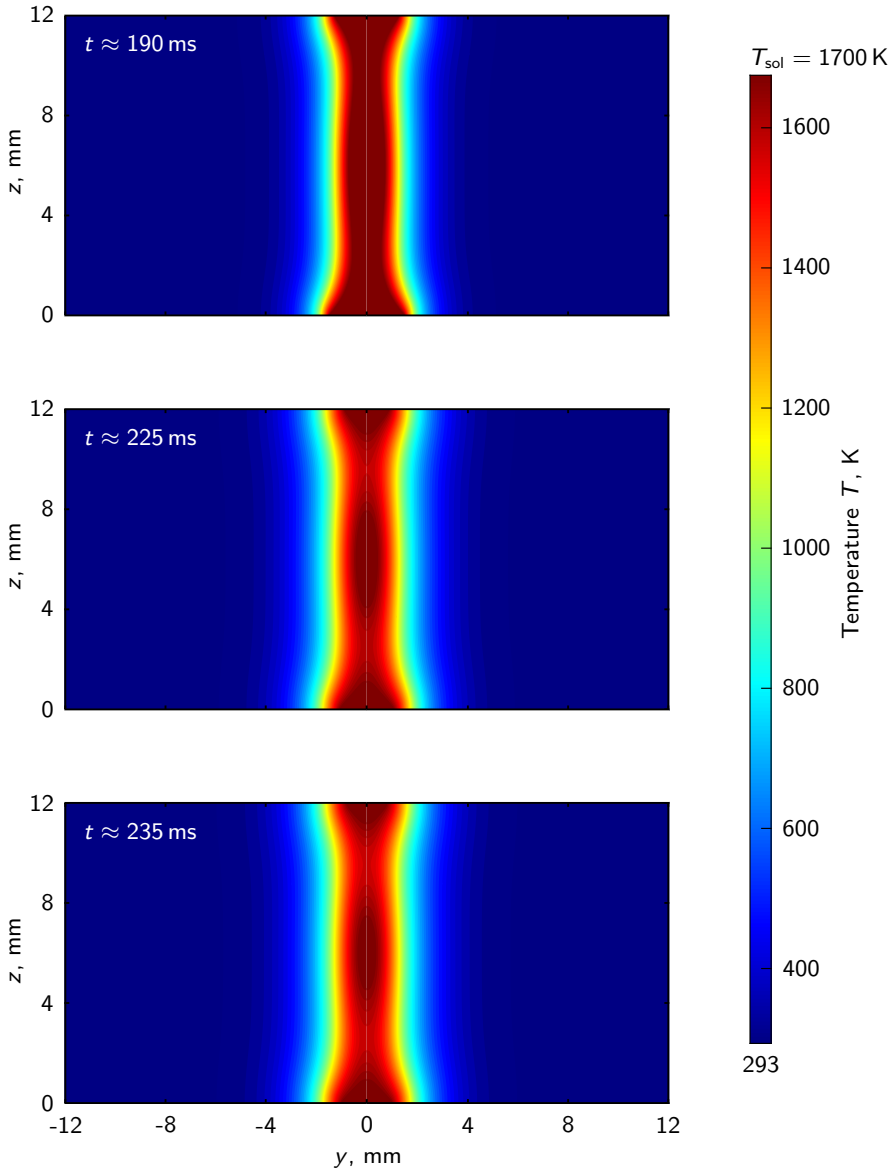

Figure 5.30: Transient temperature distribution in the two-dimensional computational domain calculated with a three-dimensional equivalent heat source

in these regions is correctly set by the algorithm and equals the solidification temperature of the material, $T_{sol} = 1700\,K$. The last solidifying liquid metal in the three larger regions of the weld pool can as well be recognized in the calculated temperature field at $t \approx 235\,ms$.

For the visualization of the heating and cooling stages of the metal during the LBW process, two thermal cycles are calculated on the top and bottom surfaces of the 12 mm thick unalloyed S355J2+N steel sheets, as illustrated in Figure 5.31. The corresponding distances from the weld centerline are A = 1.6 mm on the top and B = 2 mm on the bottom surface of the welded steel sheets. It is worth mentioning that in contrast to the weld pool simulation, see Section 5.3, the thermal cycles calculated with the EHS are transient, thus providing complete information about the temperature field independent of the size of the computational domain.

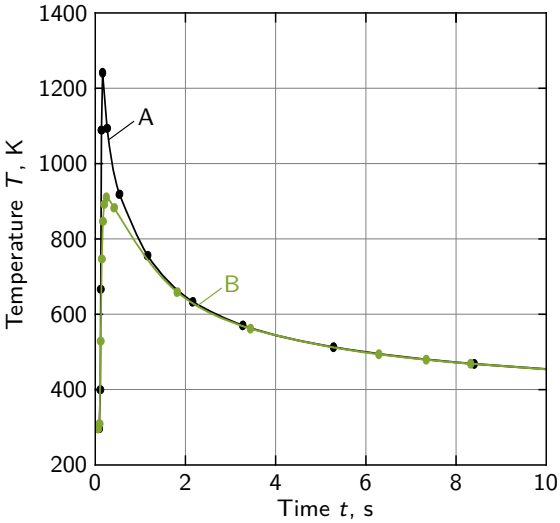

Figure 5.31: Calculated thermal cycles on the top (A) and the bottom (B) surfaces of the 12 mm thick S355J2+N steel sheets using an equivalent heat source

5.7 Mechanical Simulation

Figures 5.32 to 5.34 represent the calculated distribution of the σ_x, σ_y, and σ_z components of the stress generated in the 12 mm thick S355J2+N steel sheets during the LBW process. These act in all three spatial directions. Here, σ_x corresponds to the transversal, σ_y to the horizontal, and σ_z to the vertical direction. The stress components are given at $t \approx 235\,ms$, which is the last point in time at which liquid metal is found in the bulging region, see Sections 5.3 and 5.6, assuming that the local solidification temperature of the material

remains $T_{sol} = 1700\,K$. The corresponding temperature distribution depicted in Figure 5.30 indicates that at this point in time, only the two narrow regions located between the three larger regions of the weld pool, which are the top, bulging, and bottom regions, are completely solid. As a consequence, the liquid metal in the larger regions remains stress-free, whereas the solid metal in the narrow regions experiences tensile stress. Nevertheless, the stress distributions of the three components outside the FZ show several regions of high compressive or tensile stress. Considering the σ_x stress component acting in the welding direction, it is found that the solid material around the FZ experiences high compressive stress throughout the sheet thickness, reaching up to $-384\,MPa$. Further away from the HAZ, the region of compressive stress is followed by a larger region of tensile stress, which reaches a maximum of 60 MPa at the current point in time, as shown in Figure 5.32. Conversely, the σ_y stress component, which acts perpendicularly to the centerline crack, is tensile almost everywhere except for two small regions on the top and bottom surfaces, see Figure 5.33. Here, the maximum value of the compressive stress is similar to this of the σ_x stress component, reaching $-398\,MPa$. The value of the maximum tensile stress, on the other hand, nearly doubles and reaches 118 MPa. The σ_z stress component depicted in Figure 5.34 acts in the thickness direction of the welded steel sheets. As observed in the figure, σ_z is zero on the top and bottom surfaces, thus satisfying the physical condition of the free surface. Moreover, similar to the distribution of σ_x, the material in the HAZ experiences high compressive stress, followed by an even larger region of tensile stress. However, for σ_z, the maximum compressive stress of $-260\,MPa$ is approximately 30% lower, and the maximum tensile stress of 182 MPa is about three times higher.

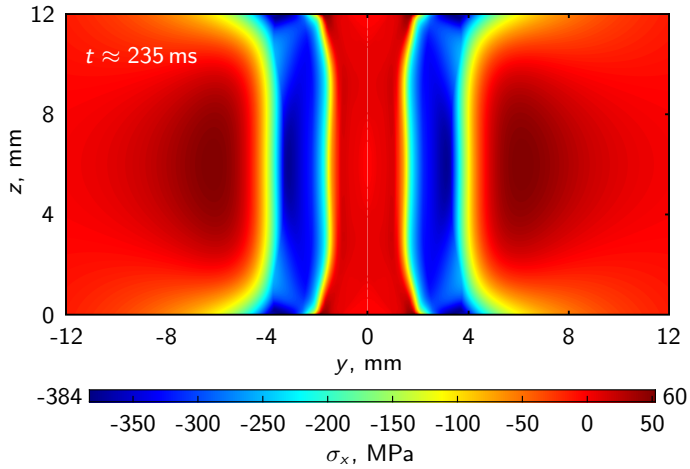

Figure 5.32: Calculated transversal stress field, σ_x, at the final solidification stage in the bulging region, assuming a local solidification temperature of $T_{sol} = 1700\,K$

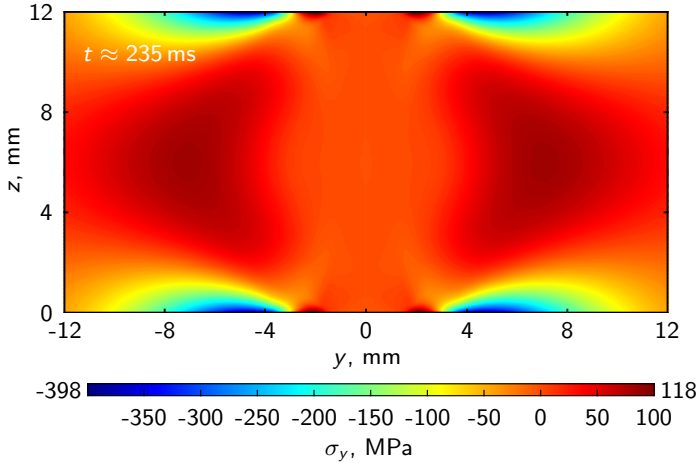

Figure 5.33: Calculated horizontal stress field, σ_y, at the final solidification stage in the bulging region, assuming a local solidification temperature of $T_{sol} = 1700\,K$

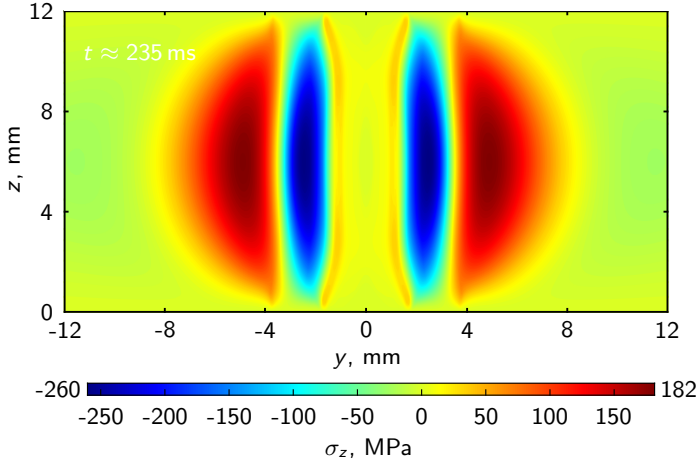

Figure 5.34: Calculated vertical stress field, σ_z, at the final solidification stage in the bulging region, assuming a local solidification temperature of $T_{sol} = 1700\,K$

In Figures 5.35 to 5.37, a metallographic cross-section of the 12 mm thick laser beam welded S355J2+N steel sheets with a centerline solidification crack in the bulging region as well as the temporal evolution of the calculated stress components, σ_x, σ_y, and σ_z, and the temperature, T, are shown. The corresponding evaluation points are highlighted by colored dots in the metallographic cross-section and set in the regions where the liquid metal solidifies at last, namely at the top and bottom surfaces of the steel sheets and at the center of the bulging region. According to the obtained results the bulging region is the only region subjected to tensile stress. Moreover, tensile stresses develop there in all three spatial directions simultaneously. Thereby, the transversal stress, σ_x, is the highest, reaching approximately 77 MPa at $t = 0.4$ s, followed by the vertical stress, $\sigma_z \approx 70$ MPa, and the horizontal stress, $\sigma_y \approx 40$ MPa. In contrast, the stresses developing in the top and bottom regions, see Figures 5.36 and 5.37, are tensile only during the initial cooling stage, with exception of σ_z, which remains 0 MPa during the entire cooling period of the welded steel sheets. However, as the processed material in the top and bottom regions continues cooling, σ_y decreases to 0 MPa at $t = 0.4$ s, and σ_x changes from tensile to compressive. Similar to the center of the bulging region, σ_x has the highest magnitude of all stress components in both the top and the bottom region as well. Nevertheless, its maximum absolute value is several times smaller than in the bulging region, reaching approximately 25 MPa at $t = 0.4$ s.

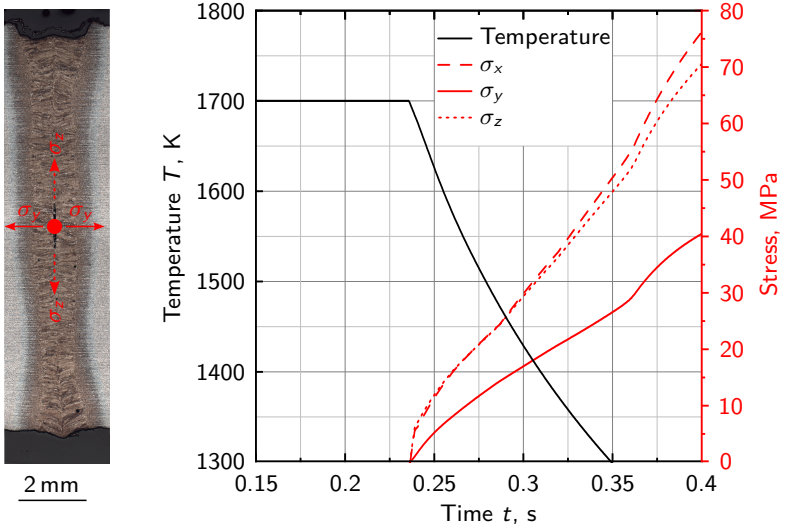

Figure 5.35: (left) Exemplary metallographic cross-section of the 12 mm *thick S355J2+N steel sheets showing a centerline crack in the center of the bulging region; (right) stress components and temperature versus time*

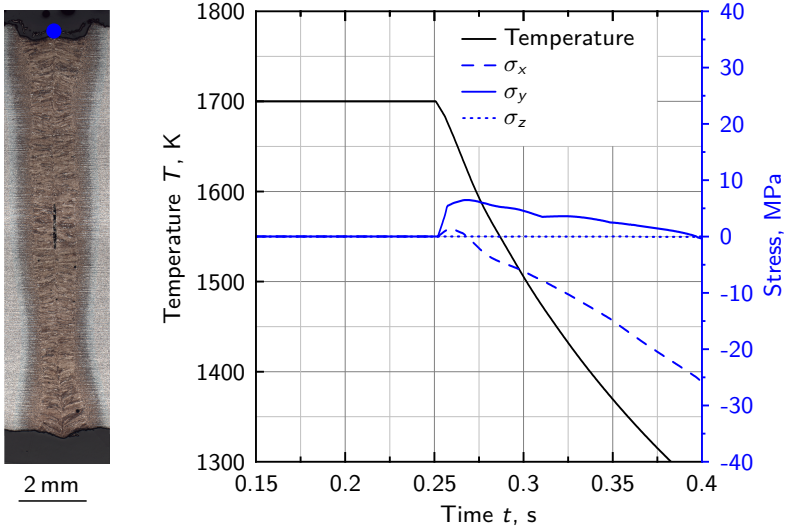

Figure 5.36: (left) Exemplary metallographic cross-section of the 12 mm *thick S355J2+N steel sheets; (right) stress components and temperature versus time*

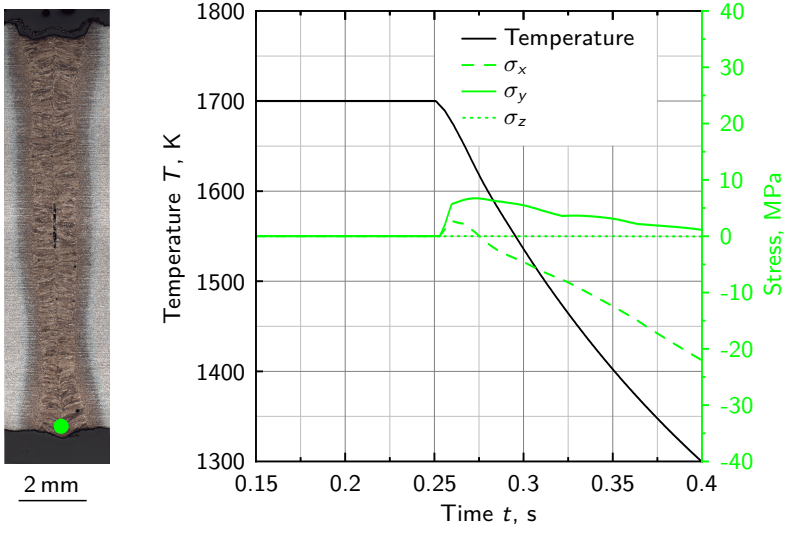

Figure 5.37: (left) Exemplary metallographic cross-section of the 12 mm *thick S355J2+N steel sheets; (right) stress components and temperature versus time*

6 Discussion

This chapter focuses on the results obtained with the developed multiphysics mathematical framework and the methodical analysis of the influence of the bulging region on the three most critical factors for the formation of solidification cracks, namely the thermal, metallurgical, and mechanical factors.

6.1 Verification and Validation

Before analyzing and discussing the theoretical results, it is essential to verify and validate these. The validation is conducted by comparing the numerical results to experimental measurements. Additionally, the derived general analytical solutions and the developed numerical procedure used to calculate the main solidification parameters are verified against known analytical solutions and a specially designed benchmark case, see Section 5.5.

6.1.1 Weld Pool Simulation

The main goal of the weld pool simulation presented in Section 4.1 is to obtain an accurate steady-state solution for the three-dimensional weld pool geometry, including the experimentally observed bulging region, see Section 5.1. A qualitative comparison of the real-time observations shown in Figures 5.1 and 5.2 and the numerically predicted weld pool geometry given in Figure 5.6, indicates that the thermo-fluid dynamics model can closely reproduce the geometrical characteristics of the weld pool, including the bulging region in the cross-section and the longitudinal section seen in Figures 5.7 and 5.8, respectively. Furthermore, to fully validate the numerical results corresponding to the case of the 12 mm thick laser beam welded S355J2+N steel sheets, these are compared to experimentally obtained metallographic cross-sections and thermal cycles. In Figure 6.1, an exemplary comparison of a metallographic cross-section extracted from the middle of the weld seam as indicated in Figure 3.2, and the numerically calculated cross-section, is shown. It is well known that the metallographic cross-sections extracted at different positions along the weld seam show deviations of up to several percent [101]. Moreover, these are not perfectly symmetrical, showing minor asymmetries on both sides of the weld centerline. As observed in Figure 6.1, this is also the case for the 12 mm thick S355J2+N steel sheets. Nevertheless, the obtained experimental and numerical fusion lines show a good agreement over the entire sheet thickness except for the deviations in the top and bottom regions, which are slightly overestimated by the thermo-fluid dynamics model.

Subsequently, the calculated thermal cycles are validated by comparing these to thermocouple measurements obtained during the LBW process, as illustrated in Figure 3.2. The

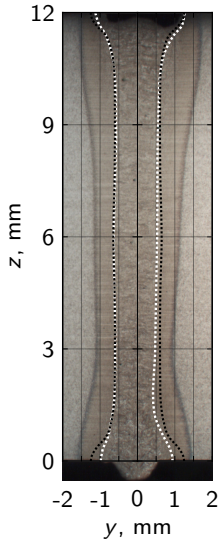

Figure 6.1: Exemplary comparison of calculated (black dashed line) and experimentally obtained (white dashed line) fusion lines

transversal distances of the measurement positions to the weld centerline used in the experiment, the three-dimensional weld pool simulation, and the two-dimensional heat conduction simulation are listed in Table 6.1. In the experiment, the distances were measured from the weld centerline to the middle of the corresponding hot junction. The comparison of the measured and calculated time-temperature curves can be seen in Figure 6.2. Here, the time-temperature curves are aligned according to the peak temperatures, i.e., the maximum temperature values for both thermal cycles correspond to the same point in time. According to Figure 6.2, the thermo-fluid dynamics model captures well the thermal history of the welded steel sheets, having minor discrepancies of approximately 50 K.

Table 6.1: Distances of the measurement positions of the thermal cycles to the weld centerline used in the experiment and the mathematical framework

Position	A	B
Experiment ± 0.2 mm	1.42 mm	2.30 mm
Weld pool simulation	1.58 mm	2.10 mm
2D Heat conduction simulation	1.60 mm	2.00 mm

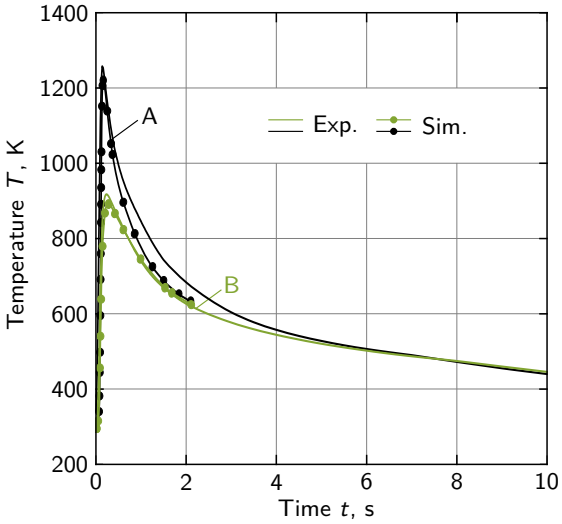

Figure 6.2: Comparison of calculated and experimentally obtained thermal cycles on the top (A) and bottom (B) surfaces of the 12 mm *thick S355J2+N steel sheets*

In the final validation step, the thermal process efficiency, η_{LBW}, is calculated and compared to experimental values from the literature obtained for similar process conditions. This is numerically estimated by relating the total amount of energy absorbed from the welded steel sheets through the keyhole surface to the laser power, P_{L}, used in the experiment:

$$\eta_{\mathrm{LBW}} = \frac{\iint_A \mathbf{n} \cdot (-\lambda \cdot \nabla T)\, \mathrm{d}A}{P_{\mathrm{L}}}. \tag{6.1}$$

Here A is the keyhole surface, $\mathbf{n}$ the unit normal inward vector of A, λ the thermal conductivity of the processed material, and T the temperature. Using Equation (6.1) and $P_{\mathrm{L}} = 14\,\mathrm{kW}$, see Table 3.4, a thermal process efficiency of approximately 83% is obtained. This value agrees well with the experimental range of 65% to 85% reported in the literature [75].

6.1.2 Lamé Curves Approximation of the Weld Pool Geometry

The validity of the Lamé curves approximation technique described in Sections 4.2 and 5.4 is first demonstrated on the 2 mm thick laser beam welded austenitic 316L steel sheets. For completeness, the weld pool rear part is approximated with a Lamé curve and an elliptical function, as depicted in Figure 6.3. Thereby, the data points (blue dots) used for the approximation, as well as the length and width of the weld pool rear part, are estimated from

the ripples, i.e., solidification lines, recognized in Figure 5.5 as well as from the geometry of the weld end crater shown in Figure 5.4. It is worth mentioning, however, that although the geometry of the ripples correlates strongly with the geometry of the weld end crater, the weld end crater dimensions must be corrected, as described in [AJ7], [AJ13] before extracting the data points. By comparing the results obtained with the different functions, it becomes clear that using an elliptical function for the approximation leads to an overestimation of the weld pool dimensions. As a result, the subsequently calculated solidification parameters, i.e., crystal axis, growth rate, and cross-sectional area, will also differ significantly. Conversely, the Lamé curve approximates the geometry of the ripples very accurately.

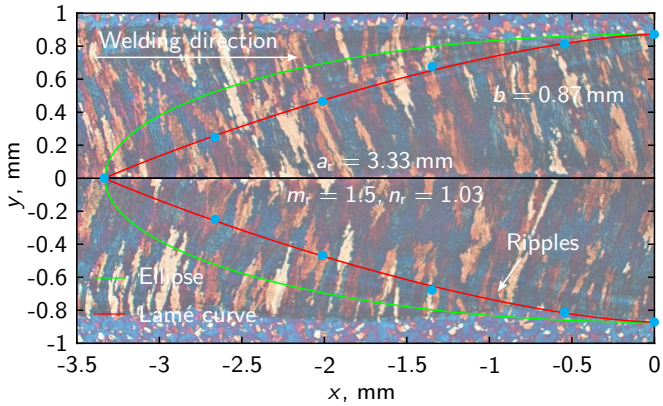

Figure 6.3: Comparison of the approximated weld pool rear part at the top surface of the 2 mm thick 316L steel sheets with a Lamé curve and an elliptical function to experimental data points (blue dots) taken along the ripples seen in Figure 5.5.

Furthermore, the validity of the developed approximation technique is demonstrated on the three-dimensional weld pool geometry of the 12 mm thick S355J2+N steel sheets. For this purpose, the two-dimensional contours of the solidus isosurface are approximated in the three horizontal sections characterized by the three main flow patterns in the weld pool described in Section 5.3. The horizontal sections are located at $z = 12$ mm, $z = 10$ mm, and $z = 6$ mm. The comparison of the approximated weld pool geometry and the data points extracted from the weld pool simulation can be seen in Figure 6.4. The shape parameters and number of data points corresponding to the six Lamé curves are given next to these. In addition, the data points are approximated with elliptical functions, as for the two-dimensional case described above. By comparing the approximated Lamé curves to the data points, it can be seen that the algorithm developed in the present work describes the numerically estimated weld pool geometry with very high accuracy, having a total error of less than 1%. Conversely, the approximation of the two-dimensional contours by elliptical functions, which are widely used in the literature [39, 79, 88], is rather insufficient, and thus may result in an EHS

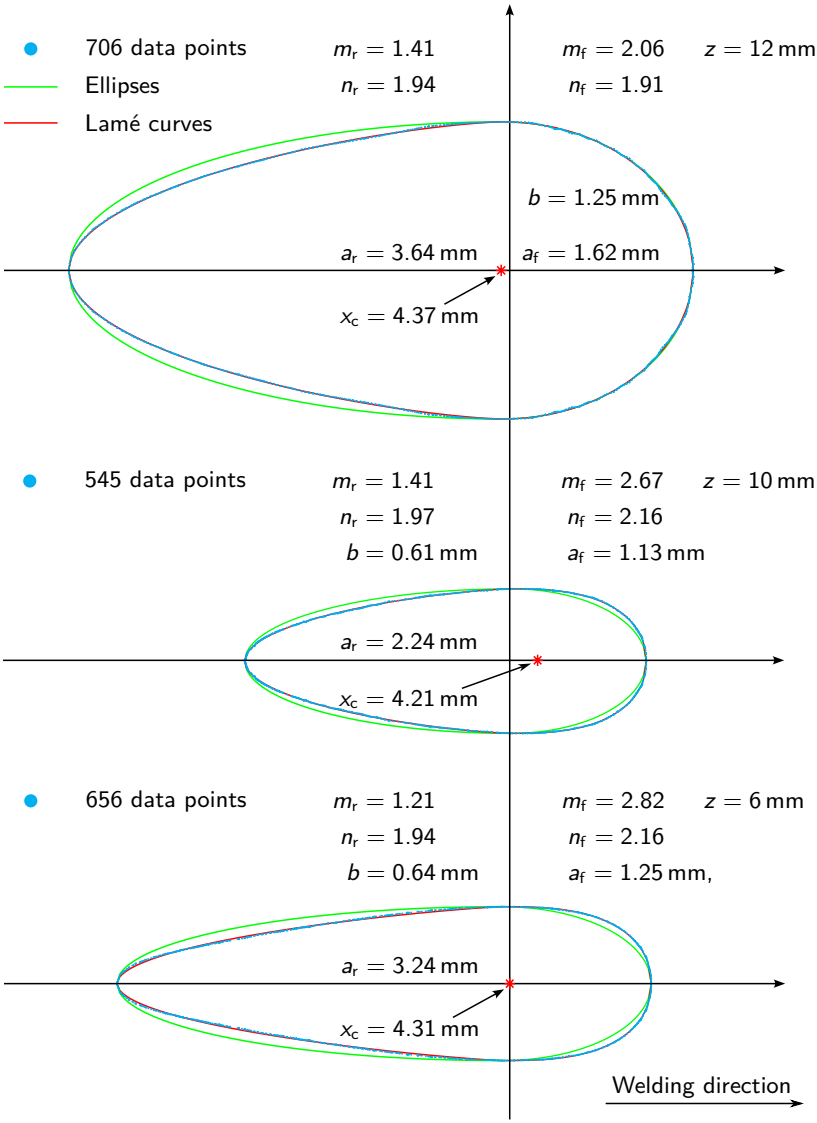

Figure 6.4: Comparison of the approximated weld pool geometry in three horizontal sections of the 12 mm thick S355J2+N sheets, defined at the (top) $z = 12\,\text{mm}$, (middle) $z = 10\,\text{mm}$, and (bottom) $z = 6\,\text{mm}$, with Lamé curves and elliptical functions to data points (blue dots) extracted from the weld pool simulation.

containing either more or less energy when compared to the solution of the thermo-fluid dynamics model. Another important consequence of the inaccurate approximation of the weld pool geometry by elliptical functions is the change in the shape and dimensions of the bulging region, and thus of the main solidification parameters, see Sections 4.3 and 5.5. In contrast, the developed approximation technique enables the one-way coupling of the process simulation to both the mechanical and the material simulation by using the same three-dimensional weld pool geometry as the input parameter, see Chapter 4. This results in a more consistent coupling of the main physical domains, allowing for an accurate study of the bulging-cracking relationship. Hence, the Lamé curves approximation technique has to be used when critical geometrical particularities of the weld pool geometry, such as the bulging region and their corresponding effects on further factors, need to be studied in-depth.

6.1.3 Solidification of a Steady-State Weld Pool Geometry

According to Section 4.3, a two-dimensional general analytical solution and a three-dimensional numerical procedure are derived and developed, respectively, to determine the main solidification parameters during the steady-state solidification of an arbitrary weld pool geometry, namely the crystal axis, the growth rate, and the cross-sectional area of the columnar crystal. Furthermore, as shown in Section 5.5, the growth rate and the cross-sectional area are dependent on the crystal axis. Therefore, by verifying and validating the predicted crystal axis, the validation of the other two solidification parameters is implicitly achieved. However, since the measurement and visualization of a crystal with a complex three-dimensional shape represents an experimentally challenging task, in practice the predicted microstructure is often validated using two-dimensional metallographic macro sections extracted from the top and bottom surfaces of the welded steel sheets.

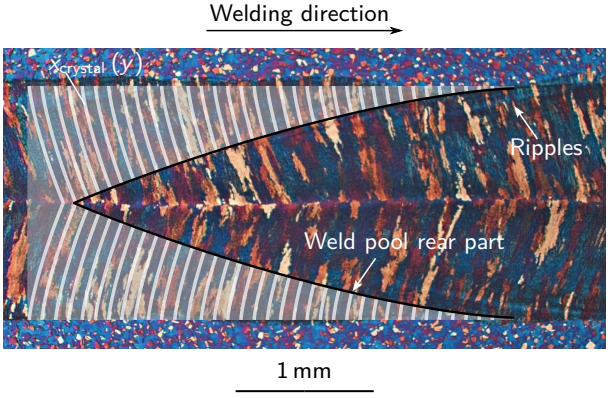

Figure 6.5: Comparison of the experimentally determined and analytically calculated grain structure on the top surface of the 2 mm thick 316L steel sheets

Regarding section Section 3.1, the austenitic 316L steel sheets are chosen for the validation of the calculated crystal axis due to the higher contrast between the grains when color etching is used to visualize the weld microstructure. For the experiments, a low sheet thickness and high welding speed were selected, resulting in nearly constant temperature distribution along the thickness direction, i.e., parallel seam flanks, see Figure 5.5. Consequently, the crystals grew predominantly in the horizontal direction. Therefore, the crystal axis determined with the derived analytical expressions for two-dimensional columnar crystal growth can be validated by comparing this to the crystals found in the horizontal section taken directly underneath the top surface of the welded 316L steel sheets. As observed in Figure 6.5, all crystals, highlighted in white, intersect the weld pool rear part, highlighted by the black line, at an angle of 90°. Moreover, both the length and the direction of solidification of the calculated crystals agree well with the experimental observations.

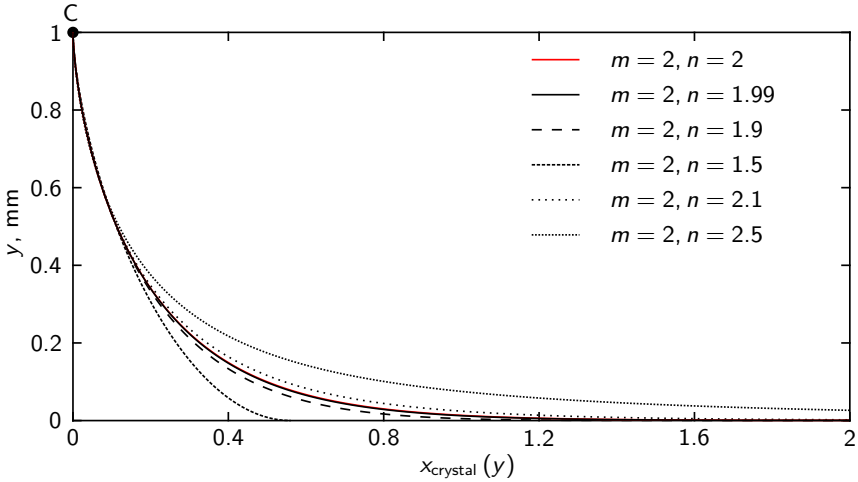

Figure 6.6: Comparison of the crystal axes, $x_{\text{crystal}}(y)$, calculated for a weld pool rear part approximated with elliptical functions ($m = n = 2$), and Lamé curves ($m = 2$, $n \neq 2$); "C" – start position of the crystal growth

In addition, the derived analytical expression for the crystal axis is verified by comparing this to a known analytical solution for the special case of an ellipse-shaped weld pool rear part, i.e., $m = n = 2$ [39]. Since the derived solution represents a general solution of the two-dimensional solidification problem, this can be evaluated for an arbitrary combination of shape parameters, except for $n = 2$, where the solution has a singularity, see Equation (5.19). Therefore, it can be expected that the general solution must converge to the known solution given in Equation (5.21) when $m = 2$ and $n \approx 2$. In Figure 6.6, the calculated crystal axes obtained for various combinations of $m = 2$ and $n \neq 2$ are shown. For simplification,

the half-width of the weld pool is set to $b = 1\,\text{mm}$ and the length of the weld pool rear part to $a_r = 4\,\text{mm}$. However, the ratio $a_r/b = 3.33/0.87 \approx 4$ obtained for the laser beam welded 316L steel sheets is preserved. By comparing the presented graphs, the crystal axis calculated with the general solution for $m = 2$ and $n = 1.99$ is practically identical to the solution obtained with elliptical functions, highlighted in red, thus confirming the plausibility of the derived solution given in Equation (5.19). Moreover, it is seen that a slight variation of the shape parameters, e.g., for $n = 1.9$ or $n = 2.1$, leads to adequate results, as these bound the solution obtained for the special case $m = n = 2$. Considering bigger variations of the shape parameters, however, e.g., $n = 1.5$ or $n = 2.5$, leads to rather significant changes in the calculated crystal axis, and consequently, to different growth rates, and cross-sectional areas, emphasizing once more the importance of the derived general analytical solutions.

Since the calculated three-dimensional crystal axes can not be validated by a direct comparison to experimental results, the numerical procedure described in Section 5.5 is verified by making use of the validated two-dimensional results presented above. For this purpose, the crystal axis and the growth rate corresponding to the case of 2 mm thick laser beam welded austenitic 316L steel sheets are computed once more using the developed numerical procedure. Thereby, the distance, $\mathrm{d}x_0$, by which the solidification front is moved, is iteratively reduced until the corresponding root-mean-square error (RMSE) of the difference between the analytical and numerical results is sufficiently small for both the crystal axis and the growth rate. The obtained results are illustrated in Figure 6.7, indicating that the RMSE is relatively high for a step size bigger than 0.1 mm. Nevertheless, for small $\mathrm{d}x_0$ values, e.g., for $\mathrm{d}x_0 = 0.01$, the RMSE is approximately 1%. Hence, a step size of $\mathrm{d}x_0 = 0.001$ was used in the computations, ensuring algorithm-independent and highly accurate results.

To further verify the developed numerical procedure, this was applied to compute crystal axes corresponding to a steady-state solidification of a three-dimensional ellipse-shaped weld pool rear part, see Figure 5.23. Notably, the half-width and the depth of the weld pool were intentionally set equal, resulting in rotational symmetry around the x-axis. Consequently, the calculated crystal axes must grow in different two-dimensional planes going through the weld centerline on the top surface of the steel sheets. Furthermore, these must be identical, independent on the position from where their growth starts, see Sections 4.3 and 5.5. In other words, although the weld pool geometry is three-dimensional, due to the rotational symmetry, the crystal axes must converge to the same point on the top surface, and have the same shape and length. As seen in Figure 5.23, the former requirement is fulfilled and all five crystal axes meet at the top surface. To compare the geometries of the crystal axes, these were rotated around the x-axis until the corresponding two-dimensional planes in which these grow coincided with the $x - y$ plane, see Figure 6.8. A closer look at results reveals that the computed crystal axes have identical shape and length, agreeing fully with the theory and the assumptions made in Section 4.3. In addition to the rotational symmetry, the weld pool half-width to rear part length ratio of 4, obtained for the austenitic 316L steel sheets, was kept constant for all computations. Therefore, the numerically estimated three-dimensional crystal axes, shown in Figure 5.23, must be identical to the analytically calculated two-dimensional crystal axis seen Figure 6.6. This is confirmed by the comparison depicted in Figure 6.8, and therefore is the validity of the developed solidification model.

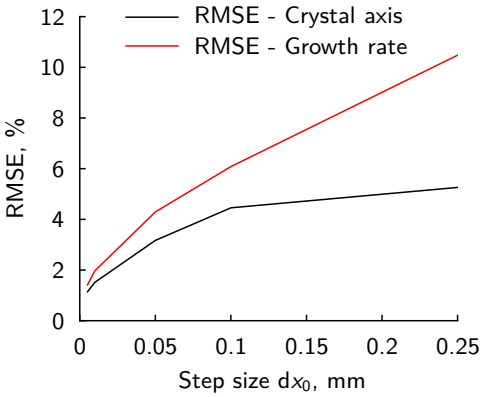

Figure 6.7: Root-mean-square error of the difference between the analytical and numerical results of the crystal axis and the growth rate, calculated for an ellipse-shaped weld pool rear part ($a_r = 4\,\text{mm}$, $b = 1\,\text{mm}$), as a function of the step size, dx_0

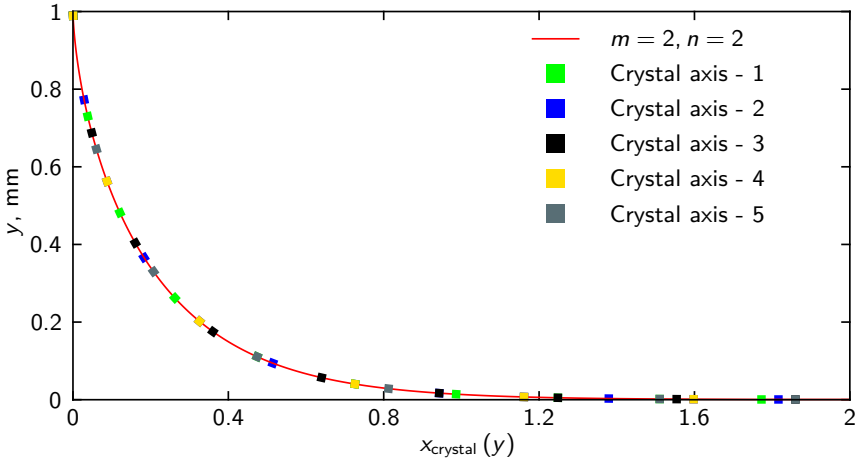

Figure 6.8: Comparison of calculated crystal axes for a 2D (red line, taken from Figure 6.6) and 3D (five crystal axes taken from Figure 5.23 and rotated to the $x - y$ plane) ellipse-shaped weld pool rear part ($a_r = 4\,\text{mm}$, $b = 1\,\text{mm}$)

6.1.4 Global Heat Conduction Simulation with an Equivalent Heat Source

In the following, the validation of the two-dimensional transient temperature distribution obtained with the EHS, see Section 5.6, is presented. In Figure 6.9, the FZ of the 12 mm thick laser beam welded S355J2+N steel sheets is exemplary compared to the solidus isotherms predicted by the thermo-fluid dynamics model and extracted from the metallographic cross-section, shown in Figure 5.7 and Figure 6.1, respectively. The comparison indicates that there is a good correlation between the FZ defined by the EHS, i.e., the region where the temperature equals the solidus temperature of the steel used, $T_{sol} = 1700\,K$, and the experimentally obtained and numerically determined solidus isotherms. Nonetheless, minor deviations are found in the bottom region, where the EHS is slightly wider. These are caused by the elemental approach employed in the model, i.e., the temperature of the element instead of the corresponding nodes found by the EHS algorithm is set to the solidus temperature. This means that even if a single node is detected as part of the EHS, the temperatures in all nodes of the corresponding element are set to T_{sol}. Consequently, the algorithm tends to overestimate the size of the approximated EHS by the length of two elements. The second reason contributing to the deviations is the two-dimensional formulation of the heat conduction problem, which results in slightly overestimated heat fluxes.

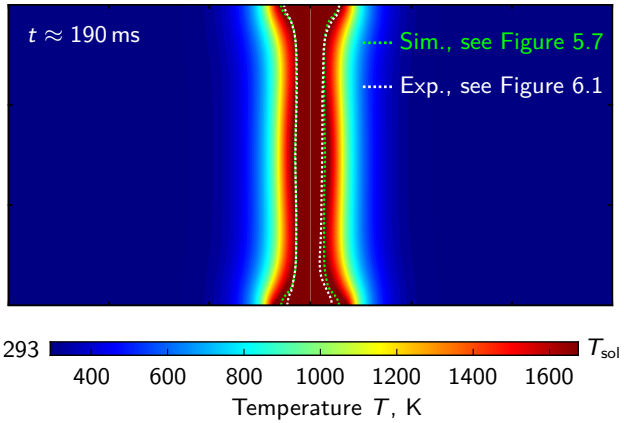

Figure 6.9: Comparison of calculated fusion lines of the 12 mm *thick S355J2+N steel sheets using an equivalent heat source and the solidus isotherms extracted from the weld pool simulation (green dashed line) and the metallographic cross-section (white dashed line)*

To validate the temporal evolution of the two-dimensional temperature field, the numerically calculated and experimentally measured thermal cycles are compared in Figure 6.10. The corresponding transversal distances of the measurement positions on the top and bottom surfaces of the welded steel sheets to the weld centerline are given in Table 6.1. According

to the obtained results, the 2D heat conduction simulation with the EHS captures well the thermal history at both measurement positions and accurately predicts the maximum temperatures. It is worth mentioning that there are small discrepancies between the results in the later cooling stage. However, at this point in time, the temperature in the bulging region lies below the theoretically lowest eutectic temperature of the Fe-S system of approximately 988 °C (1261 K) [130] at which solidification cracking can occur [5], see Section 5.6. Therefore, these do not influence the predictions made by the developed multiphysics mathematical framework regarding the transient evolution of the stresses and the microstructure in the bulging region, see Chapter 5.

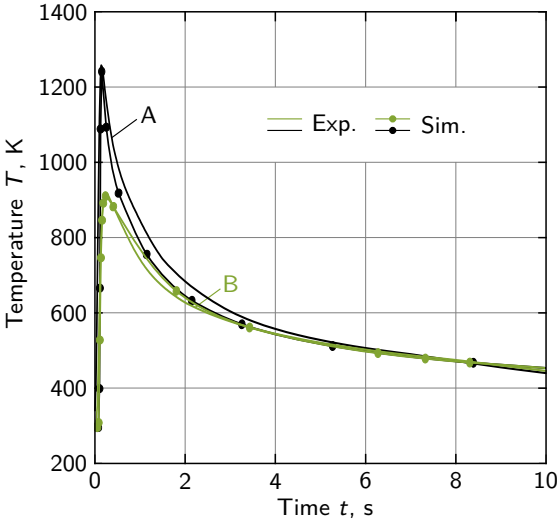

Figure 6.10: Comparison of calculated and experimentally obtained thermal cycles on the top (A) and bottom (B) surfaces of the 12 mm *thick S355J2+N steel sheets*

A further comparison to the state-of-the-art methods of EHS modeling, see Chapter 2, including the moving mesh approach proposed in [AJ1], and the boundary element method described in [AJ9], reveals that the developed EHS based on the Lamé curves approximation technique does not share their limitations. For example, the moving mesh approach is limited to simpler piece-wise-linear welding trajectories. On the other hand, the boundary element method has limited coupling options to other simulations, e.g., to the mechanical simulation. In contrast, the developed EHS offers great flexibility, allowing to consider complex welding trajectories, and to be coupled to both the metallurgical and the mechanical models. Hence, the EHS developed in the present work represents the only method enabling the study of the thermo-metallurgical and thermo-mechanical interactions, and thus the influence of the bulging region on the three dominant factors controlling solidification cracking.

6.2 Influence of the Bulging Region on the Thermal Factor

According to the current state of the art, the first critical condition for the formation of solidification cracks is the presence of liquid metal regions at the final solidification stage. This condition, as depicted in Figure 2.2, is directly determined by the thermal factor [5, 14, 26]. On the other hand, the change of the liquid metal distribution with time is governed by the geometrical characteristics of the weld pool. Hence, solidification cracking can be considered strongly dependent on the dimensions and shape of the steady-state weld pool geometry. Accordingly, to estimate the influence of the bulging region on the thermal factor, the liquid metal regions solidifying at the final solidification stage, have to be determined. In the context of Chapter 5, the results obtained from both, the weld pool simulation, see Section 5.3, and the two-dimensional transient heat conduction simulation with an EHS, see Section 5.6, can be used to study this influence. For the following analysis, however, the results from the weld pool simulation are preferred since these are three-dimensional and include additional information from the interior of the weld pool, such as temperature gradients and flow velocities of the liquid metal.

In Figure 6.11a, the three-dimensional steady-state weld pool geometry of the 12 mm thick laser beam welded unalloyed S355J2+N steel sheets is shown. In addition, the corresponding longitudinal section and three cross-sections, calculated with the thermo-fluid dynamics model presented in Section 4.1, are given in Figure 6.11b and Figure 6.11c, respectively. Thereby, the cross-sections represent three consecutive stages of the steady-state solidification process of the weld pool. As depicted in the figures, a bulging region can be recognized in both the cross-section and the longitudinal section. A closer look at the solid and liquid metal regions in the different cross-sections, highlighted in gray and red, respectively, reveals that as a consequence of the elongated top, bulging, and bottom regions, see Figure 6.11b, the region of liquid metal seen in cross-section A-A separates into three isolated liquid metal regions during the solidification process, see cross-section B-B in Figure 6.11c. As solidification progresses, see cross-section C-C in Figure 6.11c, the dimensions of the three regions containing liquid metal continue to decrease due to the narrowing of the weld pool geometry at its rear end, see Figure 6.11a. This results in a non-uniform distribution of isolated liquid metal, and hence an increased susceptibility to solidification cracking. The numerically obtained results are supported by experimental measurements published in the literature [12, 14], where the critical regions susceptible to solidification cracking are identified to experience a local solidification delay, i.e., isolated liquid metal residing on the grain boundaries and solidifying at last.

Based on the analysis of the steady-state solidification process of the three-dimensional weld pool geometry presented above, the top, bulging, and bottom regions are regarded as critical for the occurrence of solidification cracking. Thereby, the amount of liquid metal in the bulging region decreases much faster than in the top and bottom regions, thus indicating higher susceptibility to solidification cracking. However, since all three regions are isolated and contain liquid metal at the final solidification stage, these are considered in the further analysis of the influence of the bulging region on the metallurgical and mechanical factor, discussed in the following sections.

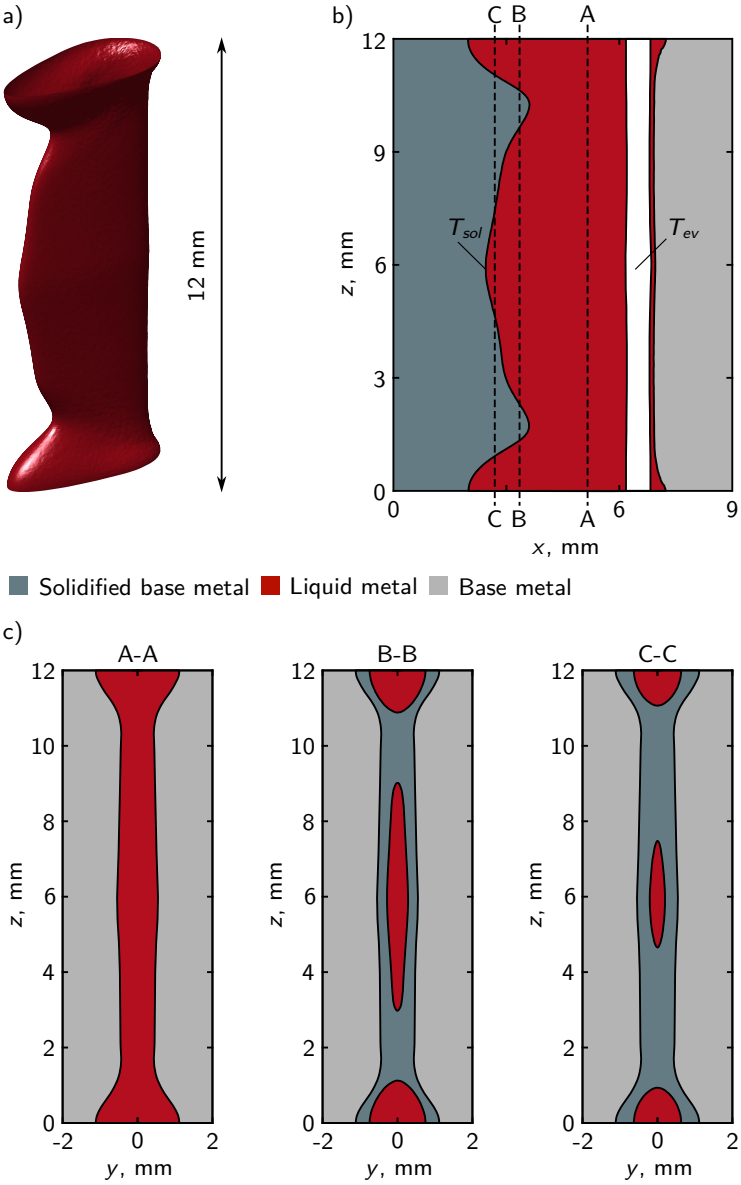

Figure 6.11: Calculated liquid metal distribution in the a) longitudinal section and the cross-sections b) A-A, c) B-B, and d) C-C

6.3 Influence of the Bulging Region on the Metallurgical Factor

The metallurgical factor represents the second part of the thermo-metallurgical interactions, which determine the dwell time of the liquid film residing on the grain boundaries. In the following, the main solidification parameters in the top, bulging, and bottom regions, identified as critical in terms of the thermal factor, are analyzed to provide a qualitative estimation of the influence of the bulging region on the metallurgical factor, and hence on the local susceptibility to solidification cracking.

6.3.1 Dependence of the Dwell Time on the Columnar Crystal Axis

The influence of the three-dimensional crystal axes on the local solidus temperature, and thus on the dwell time of the liquid film, is qualitatively estimated by making use of the results obtained with the solidification model for the 12 mm thick laser beam welded unalloyed S355J2+N steel sheets, see Section 5.5. Based on the calculated three-dimensional crystal axes shown in Figures 5.24 to 5.26, schematic projections of several exemplary crystal axes on the longitudinal section and the cross-section of the weld pool are drawn in Figure 6.12. As observed in Figure 6.12a, due to the bulging region and the two narrow regions located above and below it, the crystals growing in the three critical regions tend to converge into

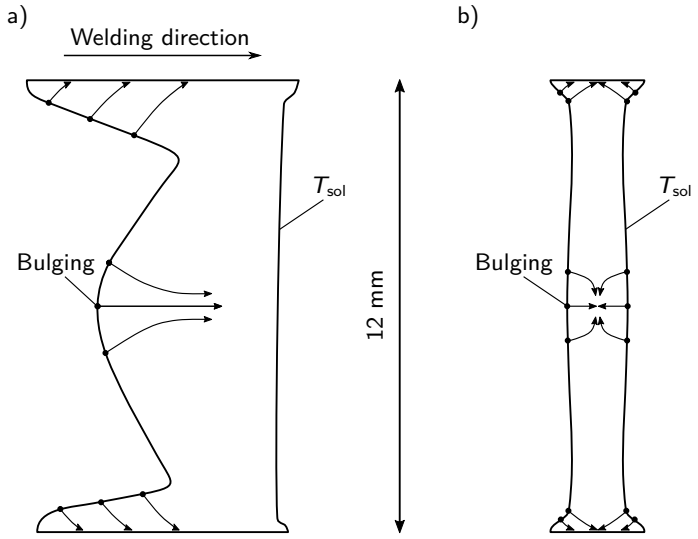

Figure 6.12: Schematic projection of exemplary crystal axes growing in the three critical regions susceptible to solidification cracking onto the a) longitudinal section and b) cross-section of the weld pool

small areas. In the top and bottom regions, the crystal axes converge toward the top and bottom surfaces of the weld pool, respectively. In contrast, the crystal axes growing in the bulging region converge to its center. Consequently, the accumulated impurities ahead of the solidification front are pushed to the same area, further increasing the local impurity concentration. As a result, the local dwell time increases, and so does the susceptibility to solidification cracking. This finding is confirmed by recent experimental studies on solidification cracking in LBW of thick unalloyed steel sheets published in [7, 15].

A closer look at the crystal axes illustrated in Figure 6.12b reveals another important consequence of the widening of the solidus isotherm in the cross-section. At the beginning of the solidification process, the crystals start growing from the cold seam flanks into the weld pool in opposite directions to each other. As the solidification process advances, the first dendrite tips coalesce where the distance between the seam flanks is smallest. However, the distance between the seam flanks in the center of the bulging region is greater compared to the corresponding distances above and below it. This can negatively influence the local susceptibility to solidification cracking for two reasons. On the one hand, the crystals need a longer time to reach the weld centerline, i.e., the dwell time of the liquid metal residing on the grain boundaries increases. On the other hand, if solidification ends before the crystal axes coalesce, i.e., locally the cooling rate is higher than the crystal growth rate, there will be a void in the center of the bulging region, which may form or initiate the centerline crack, as hypothesized in [13, 14].

6.3.2 Dependence of the Dwell Time on the Growth Rate and the Cross-Sectional Area of the Columnar Crystal

With regard to the state of the art, the dwell time of the liquid metal is determined by the non-uniform distribution of liquating elements, which in turn depends on the growth rate and the cross-sectional area of the columnar crystal. Using the analytical solution derived in [78] for the calculation of the impurity concentration, which assumes a constant growth rate and cross-sectional area of the columnar crystal, i.e., $\mathrm{d}R/\mathrm{d}t = 0$ and $\mathrm{d}\omega_{\mathrm{cr}}/\mathrm{d}t = 0$, it can be shown that the peak value and the width of the region of chemical inhomogeneity continuously increase during the solidification process. However, after a short time, the concentration of impurities ahead of the solidification front approaches its maximum represented by the asymptotic value of $1/k$, where k is the distribution coefficient defined as the ratio of the concentration of impurity in the solidified melt to the concentration in the melt from which it forms [130]. In this case, the equilibrium condition at the solidification front, i.e., equality of the chemical potentials of components in each phase, is fulfilled. In reality, nonetheless, there is no equilibrium at the solidification front due to the varying growth rate and cross-sectional area of the crystal [39]. Considering the case of an increasing growth rate and a decreasing cross-sectional area of the crystal, i.e., $\mathrm{d}R/\mathrm{d}t > 0$ and $\mathrm{d}\omega_{\mathrm{cr}}/\mathrm{d}t < 0$, for example, the impurity concentration ahead of the solidification front may exceed the theoretical asymptotic value. Under these conditions, due to the growth rate acceleration, more liquid metal will solidify, and thus, more impurities will be rejected into the weld pool. On the other hand, due to the decreasing cross-sectional area of the columnar crystal, these

impurities will be distributed over a smaller area, resulting in a further increase in the local impurity concentration. Consequently, the dwell time of the liquid film residing on the grain boundaries will drastically increase, leading to a corresponding increase in the local susceptibility to solidification cracking [33, 38]. In addition, the steel becomes more brittle as the concentration of impurities increases. This aspect is particularly critical for BCC steels, such as the unalloyed S355J2+N steels studied here, which are ductile at elevated temperatures, and thus considered more resistant to cracking in general.

In order to provide further insights into the influence of the bulging region on the dwell time, the dependence of the growth rate and the cross-sectional area of the columnar crystal on the dimensions and shape of the bulging region is studied by dimensionless analysis.

Dependence of the Growth Rate and the Cross-Sectional Area of the Columnar Crystal on the Dimensions of the Bulging Region

Here, the dependence of the growth rate and the cross-sectional area of the columnar crystal on the dimensions of the bulging region is analyzed by varying the dimensionless rear part length to half-width ratio $\Lambda = a_r/b$, as described in Section 5.5.5. Thereby, an elliptical shape of the bulging region is assumed, i.e., $m = n = 2$. Concerning the results depicted in Figure 5.27b and Figure 5.27c, it is evident that although the calculated solidification parameters differ from each other, these show similar behavior. As seen in the figures, the growth rate starts from zero at the fusion line ($\eta = 1$) and continues increasing as the crystal axis grows, reaching its maximum value of $\rho = 1$ or $R = |\mathbf{v}_{\mathbf{weld}}|$ at the weld centerline ($\eta = 0$), independently of the dimensions of the considered bulging region. Conversely, the cross-sectional area starts from its initial maximum value $\omega = 1$ at the fusion line ($\eta = 1$) and decreases continuously until reaching its theoretical minimum value $\omega = 0$ at the weld centerline. Nevertheless, a closer look at the results shows that for small values of Λ, the growth rate acceleration, $\mathrm{d}\rho/\mathrm{d}\eta$, is highest near the fusion line, where the crystal axis is most curved. In contrast, when the bulging region is elongated, e.g., $\Lambda = 5$, which corresponds to the results obtained for the 12 mm thick laser beam welded S355J2+N steel sheets ($a_r = 3.24\,\mathrm{mm}$, $b = 0.64\,\mathrm{mm}$), see Figure 5.17, the growth rate acceleration increases near the weld centerline. Furthermore, according to Figure 5.27c, for $\Lambda = 0.2$, the cross-sectional area decreases faster near the fusion line, whereas for $\Lambda = 5$, it remains nearly constant and starts decreasing close to the weld centerline at the end stage of the solidification process. Therefore, an elongated bulging region is expected to have a negative effect on the susceptibility to centerline solidification cracking.

Dependence of the Growth Rate and the Cross-Sectional Area of the Columnar Crystal on the Shape of the Bulging Region

In the following, the dependence of the growth rate and the cross-sectional area of the columnar crystal on the shape of the bulging region is analyzed by varying the parameters m and n of the Lamé curve approximating it, see Section 5.4. As shown in the previous section, due to its dimensions ($a_r = 3.24\,\mathrm{mm}$, $b = 0.64\,\mathrm{mm}$) the numerically estimated

bulging region is regarded as critical for the occurrence of solidification cracking. Hence, the dimensionless rear part length to half-width ratio of $\Lambda = 5$ is kept constant for the subsequent analysis. In Figure 5.28a, the bulging region calculated for different m and n values is represented by the dimensionless coordinates ξ and η. Thereby, the shape of the bulging region recognized in the calculated three-dimensional weld pool geometry, see Section 5.3, is considered as well. This is approximated with the shape parameters $m = 1.21$ and $n = 1.94$, see Figure 5.17, and represented in Figure 5.28 by dark blue curves. The analysis of the results illustrated in Figure 5.28c and Figure 5.28d suggests that the shape of the bulging region has a strong influence on the growth rate and the cross-sectional area of the columnar crystal. The comparison of the graphs indicates that a bulging region of a round shape, e.g., $m = n = 2.5$, results in a smoother acceleration of the growth rate and a smoother decrease in the cross-sectional area along the crystal axis. Conversely, a bulging region of a sharp shape, i.e., m and n close to 1, results in a much stronger acceleration of the growth rate and a decrease in the cross-sectional area near the weld centerline. Therefore, it can be suggested that a bulging region of a sharp shape significantly increases the susceptibility to centerline solidification cracking.

6.4 Influence of the Bulging Region on the Mechanical Factor

The mechanical factor represents the second part of the thermo-mechanical interactions determining the strains and stresses acting on the liquid film residing on the grain boundaries in the critical liquid metal regions at the final solidification stage. As demonstrated and discussed in Sections 6.2 and 6.3, the bulging region negatively influences the susceptibility of the laser beam welded steel sheets to solidification cracking by resulting in isolated liquid metal regions of extended dwell time. Nonetheless, there are many experimental and numerical studies available in the literature suggesting that the presence of isolated liquid metal regions at the final solidification stage is not a sufficient condition for the formation of solidification cracks [13, 14]. According to [5, 6], solidification cracking is rather much more the consequence of isolated liquid metal regions subjected to sufficiently high tensile strain. Here, the analysis of the influence of the bulging region on the mechanical factor is based on the localized stress, i.e., locations where the stresses experience significant increases. Generally, both the localized strain and the localized stress can be used for the analysis. Considering the two-dimensional plane strain formulation of the mechanical problem used in the developed mathematical framework and the high thickness of the welded steel sheets, however, the stress is preferred as the evaluation variable.

In reference to the above discussions and the fact that all solidification cracks observed in the present work occurred in the bulging region, it can be assumed that only the liquid metal in the center of the bulging region is subjected to sufficiently high tensile stress for the centerline crack to form. This assumption is confirmed by the results presented in Figure 5.35. According to the figure, no stress develops as long as the temperature in the bulging region equals the solidus temperature of the unalloyed S355J2+N steel sheets, $T_{sol} = 1700\,\mathrm{K}$. During this heating stage ($t \leq 235\,\mathrm{ms}$), the temperature in the weld region rises from the

room temperature to the solidus temperature leading to the expansion of the weld volume. This expansion is restrained by the base metal and the additional clamping of the specimen, see Section 5.7, causing compressive stresses in the surrounding solid metal. However, once the temperature decreases below the solidus temperature ($t > 235\,\text{ms}$), the weld volume starts shrinking and tensile stresses develop in all three spatial directions simultaneously. Due to the low material strength in the high-temperature range, as described in Section 4.6.2, the presence of a highly triaxial stress state in the grain boundaries, where a thin liquid film resides during the final stages of solidification, can be considered critical for the occurrence of solidification cracking in high power LBW of thick steel components [5, 6, 36]. By looking at the temperature fields shown in Section 5.6, it can be recognized that the tensile stresses acting in the center of the bulging region are due to the surrounding colder metal, which hinders the thermal shrinking of the weld metal therein [106, 141]. According to Figure 5.35, at $t \approx 350\,\text{ms}$ the local temperature in the center of the bulging region is close to the theoretically lowest solidus temperature of the Fe-S system, i.e., the eutectic temperature of $988\,^{\circ}\text{C}\,(1261\,\text{K})$ [130], at which solidification cracking can occur [5]. The corresponding values of the numerically estimated stresses at this point in time are approximately 51 MPa, 49 MPa, and 27 MPa for the transversal, vertical, and horizontal stress, respectively, with the assumed theoretical yield strength of the material being around 25 MPa. Although the localized horizontal stress is lower in magnitude than the transversal and vertical stresses, this is considered to be the stress component causing the centerline solidification cracking in the bulging region. The reason for this is that the horizontal stress acts in the opposite direction to the growth direction of the crystals axes, as indicated in the metallographic cross-section shown on the left-hand side in Figure 5.35, and thus possibly leads to the rupture of the liquid film residing on the grain boundaries. Furthermore, by analyzing the stress evolution at the critical top and bottom surfaces with time, see Figures 5.36 and 5.37, the above assumption stating that the absence of solidification cracks in these regions is due to the absence of tensile stress can be confirmed. According to the graphs, at the points in time corresponding to the beginning of the solidification process in the top and bottom regions (at approximately $t \approx 250\,\text{ms}$), slight transversal and horizontal tensile stresses develop on both surfaces. Nevertheless, as the solidification process continues, the transversal stress turns into compressive stress, and the horizontal stress slowly decreases, converging to zero at the point in time when the temperature is close to the eutectic temperature (at $t \approx 400\,\text{ms}$).

The obtained results suggest that the bulging region is the only weld pool region in which the critical conditions required for solidification cracking to occur, namely the presence of an isolated liquid film of extended dwell time subjected to sufficiently high tensile stress acting in the opposite direction to the growth direction of the crystals, are fulfilled. It is important to note that the tendency of the obtained results indicating increasing tensile stress in the center of the bulging region during solidification agrees well with numerical computations performed for similar welding conditions and materials [6]. Nonetheless, the predicted maximum values of the stresses at the point in time corresponding to the eutectic temperature are about 30% to 50% lower in the present analysis. These differences may arise for several reasons. On the one hand, in the developed mathematical framework, the temperature at which the liquid material starts solidifying is set to the solidus temperature rather than to the liquidus

temperature of the material, which is used in [6] instead. This results in longer solidification times, and thus higher stresses, as indicated by the results discussed above. Moreover, according to Sections 4.4 and 5.6, using the isothermal surface of the solidus temperature as a three-dimensional EHS in the two-dimensional transient heat conduction simulation provides higher accuracy. This approach automatically accounts for the influence of the latent heat of solidification on the temperature field, which directly affects the accuracy of the subsequent mechanical simulation applying the calculated temperature field as a transient thermal load. A further reason for the lower values predicted by the mechanical model is the very fine mesh size of 0.03 mm used for the spatial discretization of the FZ and the HAZ. From a numerical point of view, coarse mesh elements are stiffer, leading to overestimation of the predicted stress [106, 141]. In addition, it should be mentioned that often the discrepancies between the numerically obtained results are due to different values of the material properties used in the simulations, e.g., Young's modulus, or due to simplifications, e.g., reduction of the real size of the steel sheet by replacing part of the base metal by theoretically equivalent spring elements, as done in [6]. Therefore, the complete length of the laser beam welded steel sheets was accounted for in the current model.

6.5 Centerline Solidification Cracking in Terms of the Bulging Region

With respect to the literature review, the formation of solidification cracks is governed by the complex interactions of the thermal, metallurgical, and mechanical factors. Thereby, the thermo-metallurgical interactions determine the local solidification microstructure, whereas the thermo-mechanical interactions determine the local strains and stresses. Nonetheless, most of the published theories and experimental methods developed to assess the critical conditions required for a solidification crack to occur are focused either on thermo-metallurgical or thermo-mechanical interactions. Moreover, to the best of the author's knowledge, the influence of the bulging region on the local susceptibility to solidification cracking has not been explicitly studied yet. Therefore, based on the results obtained in the present work, see Chapter 5, as well as the corresponding analysis and discussion of these, presented in Sections 6.2 to 6.4, two possible mechanisms for the formation of centerline solidification cracking in terms of the bulging region are proposed.

The first mechanism is related to the crystal growth in the bulging region. As discussed at the end of Section 6.3.1 and illustrated in Figure 6.13, the numerically estimated columnar crystal axes growing in the horizontal section through the center of the bulging region need a longer time to reach the weld centerline due to the widening of the FZ. Hence, considering the high cooling rates on the order of $10^3\,\mathrm{K\,s^{-1}}$, see Sections 5.2, 5.3 and 5.6, which are typical for LBW of thick steel components, it is reasonable to assume that when locally the cooling rate is higher than the crystal growth rate, the dendrite tips do not coalesce at all, thus possibly leading to the formation or initiation of the centerline solidification crack, as hypothesized in [13, 14]. Indeed, if this assumption is correct, it can be expected that the weld fracture surfaces will be smooth, the dendrites regularly arranged, and the dendrite tips free of deformation. These expectations are confirmed by experimental studies

on solidification cracking in laser beam and hybrid welding of thick unalloyed steel sheets. Thereby, the centerline solidification cracks observed in the experiments were fracture opened, and their surfaces were examined with a SEM, showing that the surfaces of the cracks are predominantly smooth and the dendrite tips well-rounded [7].

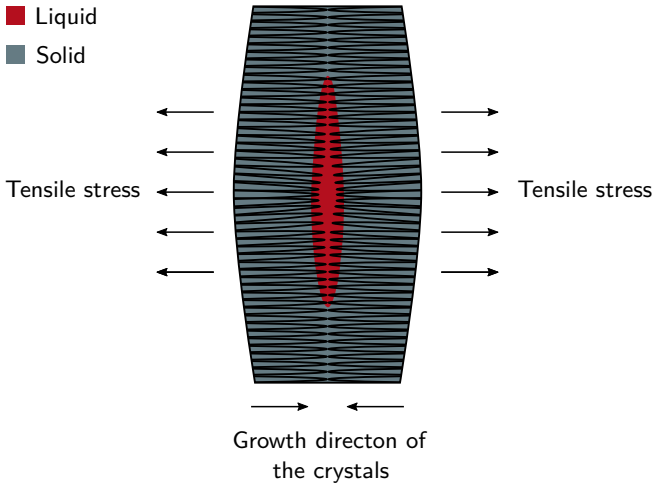

Figure 6.13: Schematic of centerline solidification cracking in the bulging region during deep penetration laser beam welding of low-alloyed and unalloyed steels

In [7], it was also discovered that the contours of the corresponding crack surfaces fit well together, suggesting that only a thin liquid film separated these during cracking and that the centerline crack formed at the final solidification stage. Furthermore, bridges of solid metal were discovered at the boundary between the fracture surfaces and the centerline crack, indicating that the faces of the crack have moved apart from each other during solidification. Since these experimental findings correlate well with the numerical results of the present work, the second formation mechanism is related to the rupture of the liquid film residing on the grain boundaries in the bulging region by localized tensile stresses, as schematically illustrated in Figure 6.13. However, as described in Section 5.7, at the last point in time at which liquid metal is found in the bulging region, the stresses in or around the bulging, and thus the cracking region, are nearly zero. Moreover, even when considering the theoretically lowest eutectic temperature of the Fe-S system at which solidification cracking can occur, the tensile stress in the center of the bulging region acting opposite to the growth direction of the crystals, increases to only 27 MPa. The interpretation of these results can be twofold. On the one hand, the results suggest that centerline solidification cracking may be caused by much lower tensile forces than previously reported [6]. On the other hand, if this is not the case, a sufficient increase in the local dwell time of the liquid film residing on the grain

boundaries is required to allow the tensile force to increase to a critical value leading to the rupture of the liquid film. Hence, considering that the laser beam welded S355J2+N steel sheets contain very low amount of impurities, see Table 3.1, it can be suggested that the segregation process may play a more decisive role in the formation of solidification cracks in deep penetration high power LBW of low-alloyed and unalloyed steel components than generally acknowledged.

Based on the experimental and theoretical results, along with their corresponding discussions presented in the previous chapters and sections, it can be concluded that the bulging region negatively influences all three dominant factors, and thus contributes to solidification cracking by leading to:

- The presence of liquid metal in the region where the centerline solidification cracks occurred in the laser beam welded steel sheets.
- A predominant crystal growth into the center of the bulging region, accompanied by an increasing growth rate and a decreasing cross-sectional area of the columnar crystal near the weld centerline, as a result of which the dwell time of the liquid film residing on the grain boundaries increases.
- Highly localized tensile stresses, acting opposite to the growth direction of the crystal axes, in the cracking region.

7 Summary

The present work deals with the methodical experimental and theoretical analysis of the bulging-cracking relationship in LBW of thick unalloyed steel sheets. Thereby, the focus is on the experimental proof of the existence of the bulging region as well as on the development of a coupled multiphysics mathematical framework allowing to study the influence of the bulging region on the three dominant factors controlling the susceptibility to solidification cracking, namely, the thermal, metallurgical, and mechanical factor.

The experimental inaccessibility of the LBW process was overcome by utilizing a butt joint configuration of a transparent quartz glass and a 12 mm thick S355J2+N steel sheet. This allowed the real-time recording of the geometrical characteristics of the liquid metal distribution in the longitudinal section by an infrared, a thermal, and a high-speed camera. The high-speed camera observations showed that the weld pool is elongated near the top and bottom surfaces of the steel sheet. Furthermore, a bulging region was observed, located directly behind the keyhole at approximately half of the sheet thickness. This region was separated from the elongated top and bottom regions by two narrow regions, and its location along the thickness direction varied slightly during the LBW process. Moreover, based on the recordings of the infrared and the thermal camera, it was discovered that the bulging region observed behind the keyhole influences the temperature distribution in the longitudinal section, leading to the bulging of the isotherms of lower temperatures located behind it, including the solidus isotherm, which defines the weld pool geometry.

Due to the experimental limitations, including the unknown and hardly determinable influence of the quartz glass plate on the observed weld pool geometry and liquid metal flow therein, a coupled multiphysics mathematical framework comprising a series of subsequent analyses was developed to provide further insights into the influence of the bulging region on the three dominant factors. The framework consists of two simulation chains designed for the methodical study of the thermo-metallurgical and thermo-mechanical interactions, respectively. The first model is a thermo-fluid dynamics model, which aims at the phenomenological reproduction of the experimentally observed geometrical characteristics of the weld pool. Thereby, a fixed keyhole geometry was adapted as an EHS. Moreover, to account for the effects of the focal position and the multiple reflections on the energy absorption, which are assumed to be decisive for the formation of a bulging region, the horizontal cross-sectional area of the keyhole in the middle of the steel sheet was slightly increased. This influences the numerically estimated dimensions and shape of the weld pool since the surface of the keyhole is assumed to be impermeable to heat and mass flow, and thus acts as an obstacle to the liquid metal flow in the weld pool. Consequently, the liquid metal flows around the keyhole surface, where it is accelerated to the rear weld pool boundary, resulting in the elongation and widening of the weld pool geometry, i.e., a bulging region.

The phenomenologically reproduced weld pool geometry was validated by comparing the predicted FZ and temperature evolution with time at different locations to experimental measurements. Once validated, the weld pool geometry was used to estimate the influence of the bulging region on the thermal factor, i.e., the presence of liquid film at the grain boundaries at the final solidification stage, which is the first condition for the formation of solidification cracks. Therefore, the estimated weld pool geometry was moved through a plane orthogonal to the welding direction at the welding speed, and the liquid metal distribution in the plane was analyzed. It was found that due to the complex geometry of the weld pool rear part, the two narrow regions located above and below the bulging region solidify earlier, so that liquid metal remains only in the elongated top, bulging, and bottom regions. As solidification progresses, the amount of liquid metal in these regions decreases further, indicating a local increase in the susceptibility to solidification cracking.

Concerning the three critical regions of increased cracking susceptibility in terms of the thermal factor, the first simulation chain was designed to study the influence of the bulging region on the metallurgical factor, i.e., the local decrease in the solidus temperature (up to the theoretically lowest solidus temperature at which solidification cracking can occur, i.e., the eutectic temperature of 988 °C (1261 K) of the Fe-S system), caused by the rise of the impurity concentration due to segregation. In the first step, the three-dimensional weld pool geometry was mathematically described with a single expression using the proposed Lamé curves approximation technique. Subsequently, this was applied as an input parameter for the solidification model, assuming that the crystals grow along the local temperature gradient, following the solidification front and not intersecting each other. The solidification model comprises two methods for calculating the three main solidification parameters: the crystal axis, the growth rate, and the corresponding cross-sectional area of the columnar crystal. The first method represents a general analytical solution derived for the case of two-dimensional columnar crystal growth, as observed on the top and bottom surfaces of the 2 mm thick laser beam welded austenitic 316L sheets and in the horizontal plane through the center of the bulging region. In contrast, the second method represents a general numerical procedure that allows considering an arbitrary weld pool geometry and calculating the main solidification parameters in the cases of two-dimensional and three-dimensional columnar crystal growth. Nonetheless, the measurement and visualization of a crystal of a complex three-dimensional shape are rather experimentally challenging. Therefore, the obtained analytical and numerical results were validated using two-dimensional metallographic macro sections extracted from the thin 316L steel sheets with predominant solidification in the horizontal plane. Moreover, the numerical procedure was verified by reproducing the validated two-dimensional results obtained with the analytical solutions and by a specially designed three-dimensional benchmark case. According to the simulation results, due to the bulging region and the two narrow regions located above and below it, the columnar crystals growing in the three critical regions converge into the top and bottom surfaces of the welded steel sheets, as well as into the center of the bulging region. Thereby, the accumulated impurities ahead of the solidification front are pushed together, leading to a further increase in the impurity concentration at these locations. As a result, the local solidus temperature decreases, i.e., the dwell time of the liquid film residing on the grain

boundaries increases, and therewith decreases also the resistivity of the processed material to solidification cracking. Furthermore, it was found that the greater distance between the seam flanks in the center of the bulging region has a negative influence on the local susceptibility to solidification cracking. Assuming that the crystals growing from the cold seam flanks into the weld pool in opposite directions to each other reach the weld centerline, i.e., the dendrite tips coalesce, the greater distance leads to a longer dwell time of the liquid metal residing on the grain boundaries, thus increasing the local susceptibility to solidification cracking. However, when the case in which the crystals do not reach the weld centerline is considered, which means that locally the cooling rates are higher than the crystal growth rate, the dendrite tips do not coalesce at all, leaving a void in the center of the bulging region, which may form or initiate the crack. Additionally, the influence of the dimensions and shape of the bulging region on the growth rate and the cross-sectional area of the columnar crystals was studied by dimensionless analysis. It was shown that the more elongated (high rear part length to half-width ratio) and sharper the bulging region, the lower the local resistivity to cracking. On the one hand, such geometry of the bulging region leads to higher growth rate acceleration near the weld centerline. Consequently, more liquid metal solidifies, and thus a higher amount of impurities is rejected into the liquid metal at the final solidification stage. On the other hand, it leads to a faster decrease in the cross-sectional area of the columnar crystal near the weld centerline. As a result, the higher amount of rejected impurities is distributed over a smaller area ahead of the solidification front, leading to an increase in the local impurity concentration, adversely affecting the susceptibility to solidification cracking in the bulging region.

The second simulation chain was applied to study the influence of the bulging region on the mechanical factor, i.e., the local and global strains and stresses in the three liquid metal regions identified as critical in terms of the thermal and material factors. Since all solidification cracks observed in the laser beam welded S355J2+N steel sheets were centerline cracks located in the middle of the bulging region, it was assumed that the remaining liquid metal in this region has to be subjected to sufficiently high tensile stress acting in the opposite direction to the growth direction of the crystals axes to cause the rupture of the liquid film residing on the grain boundaries, and thus the formation of a centerline crack. In contrast, such stresses were not expected to develop in the top and bottom regions as no cracks were found there. Therefore, a two-dimensional mechanical model was used to estimate the localized transversal stresses acting on the liquid metal in the critical regions. The transient thermal load for the mechanical simulation was computed with a two-dimensional heat conduction model in which the computational domain was defined as a plane orthogonal to the welding direction. Moreover, the approximated weld pool geometry was adapted as an EHS, thus considering the influence of the bulging region on the temperature evolution. The temperature distribution was calculated by moving the weld pool geometry through the plane at the welding speed and assigning the solidus temperature to all mesh elements located within the weld pool or on its surface, ensuring an equivalent heat input. According to the results, the bulging region is the only critical region subjected to localized transversal tensile stresses. In addition, it was also found that the stress state in the bulging region at the final solidification stage is triaxial, and all stress components are tensile. Consequently,

the stress level acting on the liquid film can only be partially relieved by yielding, significantly increasing the probability for a solidification crack to occur.

To summarize, the main contributions of the present research are the following:

- A specially designed experimental set up was successfully utilized for the real-time recording of the bulging region.
- An approximation technique based on Lamé curves has been developed, allowing an arbitrary three-dimensional weld pool geometry, including geometrical particularities such as the bulging region, to be described with a single analytical expression.
- General analytical solutions and a numerical procedure have been derived and developed, respectively, to enable the calculation of the main solidification parameters, namely, the crystal axis, the growth rate, and the cross-sectional area of the columnar crystal. Both methods use the weld pool geometry approximated with Lamé curves as an input parameter, and thus consider the one-way coupling of the process and material simulation, i.e., the thermo-metallurgical interactions.
- A numerical method based on the Lamé curves approximation technique has been proposed and used to one-way couple the physical domains of the process and structure simulation, i.e., to account for the thermo-mechanical interactions, by applying the calculated weld pool geometry as a three-dimensional EHS.
- All experimental, analytical, and numerical results obtained in this thesis indicate that an elongated bulging region of a sharp shape negatively influences the three dominant factors controlling the cracking behavior of the processed material, namely the thermal, metallurgical, and mechanical factors. Therefore, the bulging region of the weld pool is considered highly susceptible to solidification cracking.

Nomenclature

Abbreviations

Abbreviation	Meaning
BCC	Body-Centered Cubic
DFG	Deutsche Forschungsgemeinschaft
EBW	Electron Beam Welding
EHS	Equivalent Heat Source
FCC	Face-Centered Cubic
FZ	Fusion Zone
HAZ	Heat Affected Zone
HPC	High-Performance Computing
laser	Light Amplification by Stimulated Emission of Radiation
LBW	Laser Beam Welding
MWIR	Medium Wavelength Infrared
Nd:YAG	Neodymium Doped Yttrium Aluminum Garnet
PDE	Partial Differential Equation
RMSE	Root-Mean-Square Error
SEM	Scanning Electron Microscope
SSPTs	Solid-State Phase Transformations
VIS	Visible Light Spectrum
wt. %	Weight Percent
Yb:YAG	Ytterbium Doped Yttrium Aluminum Garnet

Greek letters

Symbol	Meaning	Unit
α	Angle between G and the welding direction; ferrite	°
β	Volumetric thermal expansion coefficient	K^{-1}
β'	Mean linear thermal expansion coefficient	K^{-1}
γ	Austenite	
γ'	Surface tension of the Fe-S system	$\mathrm{N\,m}^{-1}$
ϵ	Turbulent dissipation rate	$\mathrm{m}^2\,\mathrm{s}^{-3}$
C_{ϵ_1}	Turbulent model constant	$\mathrm{m}^2\,\mathrm{s}^{-3}$
C_{ϵ_2}	Turbulent model constant	$\mathrm{m}^2\,\mathrm{s}^{-3}$
$\varepsilon_{\mathrm{el}}$	Elastic strain	
$\varepsilon_{\mathrm{pl}}$	Plastic strain	
$\varepsilon_{\mathrm{th}}$	Thermal strain	
$\varepsilon_{\mathrm{tr}}$	Transformation strain	
$\varepsilon_{\mathrm{tot}}$	Total strain	
η	Dynamic viscosity; Dimensionless y-coordinate	Pa s
η_{turb}	Turbulent viscosity	Pa s
C_η	Turbulent model constant	$\mathrm{m}^2\,\mathrm{s}^{-3}$
κ	Turbulent kinetic energy	$\mathrm{m}^2\,\mathrm{s}^{-2}$
λ	Thermal conductivity	$\mathrm{W\,m}^{-1}\,\mathrm{K}^{-1}$
λ_{eff}	Effective thermal conductivity	$\mathrm{W\,m}^{-1}\,\mathrm{K}^{-1}$
λ_{turb}	Turbulent thermal conductivity	$\mathrm{W\,m}^{-1}\,\mathrm{K}^{-1}$
Λ	Dimensionless rear part length to half-width ratio of the weld pool	
ξ	Dimensionless x-coordinate	
ρ	Mass density; Dimensionless growth rate	$\mathrm{kg\,m}^{-3}$
ρ_{hc}	Mass density for heat conduction computations	$\mathrm{kg\,m}^{-3}$
ρ_{liq}	Mass density at liquidus temperature	$\mathrm{kg\,m}^{-3}$
σ	Cauchy stress tensor	$\mathrm{N\,m}^{-2}$
σ_ϵ	Turbulent model constant	$\mathrm{m}^2\,\mathrm{s}^{-3}$

σ_κ	Turbulent model constant	$\mathrm{m^2\,s^{-3}}$
$\phi(x, x_c, y, z)$	Family of Lamé curves	
$\phi'_x,\ \phi'_y,\ \phi'_z$	Partial derivatives of $\phi(x, x_c, y, z)$	
ω	Dimensionless cross-sectional area of the columnar crystal	

Latin letters

Symbol	Meaning	Unit
$a_{r,f}$	Semi-major axes of the rear and front Lamé curves	m
A_1	Austenitization starting temperature	K
A_3	Austenitization ending temperature	K
ABC	Melting trajectory	
b	Weld pool half-width; semi-minor axis of the Lamé curves	m
$c_0, \ldots, c_j$	Constant coefficients	
c_1	Model constant	$\mathrm{kg\,m^{-3}\,s^{-1}}$
c_2	Model constant	
C	Location from which the crystal starts growing	
CDE	Solidification trajectory	
C_{new}	Intersection point of the crystal and the solidification front	
CO_2	Carbon dioxide	
C_p^0	Heat capacity	$\mathrm{J\,kg^{-1}\,K^{-1}}$
C_p^{app}	Apparent heat capacity	$\mathrm{J\,kg^{-1}\,K^{-1}}$
C_{moved}	Projection of C onto the $y-z$ plane	
dl	Infinitesimal change of the crystal axis in length	m
dt	Infinitesimal time interval	s
dx_0	Distance by which the solidification front is moved per time step	m
$\Delta t_{8/5}$	Cooling time from 800 °C to 500 °C	s
ΔT	Temperature increment	K

E	Young's modulus	$\mathrm{N\,m^{-2}}$
f_L	Liquid fraction	
$\mathbf{f_V}$	Body force per unit deformed volume	$\mathrm{N\,m^{-3}}$
$\mathbf{F}$	Momentum source term	$\mathrm{N\,m^{-3}}$
F, f	Functions	
Fe	Iron	
$\mathbf{g}$	Gravity acceleration vector	$\mathrm{m\,s^{-2}}$
G	Temperature gradient	$\mathrm{K\,m^{-1}}$
h	Height; thickness	m; m
H_f	Latent heat of solidification of pure iron	$\mathrm{J\,kg^{-1}}$
$\mathbf{I}$	Identity matrix	
j	Index variable	
k	Index variable; distribution coefficient	
K	Total number of levels	
l	Index variable; crystal axis	
l_dim	Dimensionless crystal axis	
I_T	Turbulent intensity	
L_T	Turbulent length scale	m
L_tot	Total number of data points	
$m_\mathrm{r,f}$	Shape parameter of the rear and front Lamé curves	
$\mathrm{M_s}$	Martensite start temperature	K
$\mathbf{n}$	Inward unit normal vector	
$n_\mathrm{r,f}$	Shape parameter of the rear and front Lamé curves	
O	Oxygen	
p_0	Ambient pressure	$\mathrm{N\,m^{-2}}$
p	Fluid pressure	$\mathrm{N\,m^{-2}}$
P	Incident laser power	kW
P	Phosphorus	
P_κ	Turbulent production term	$\mathrm{m^2\,s^{-3}}$
$\mathrm{Pr_{turb}}$	Turbulent Prandtl number	
q	Heat flux	$\mathrm{W\,m^{-2}}$
R	Crystal growth rate	$\mathrm{m\,s^{-1}}$

R_{2D}	Crystal growth rate in 2D	$\mathrm{m\,s^{-1}}$
R_{3D}	Crystal growth rate in 3D	$\mathrm{m\,s^{-1}}$
S	Sulfur	
$\top$	Transpose of a matrix	
T_0	Ambient temperature	K
T	Temperature	K
T_{ev}	Evaporation temperature	K
T_{liq}	Liquidus temperature	K
T_{melt}	Melting temperature	K
T_{peak}	Peak temperature	K
T_{sol}	Solidus temperature	K
$\mathbf{u}$	Fluid velocity vector; displacement vector	$\mathrm{m\,s^{-1}}$; m
u_x, u_y, u_z	Fluid velocity vector components; displacement vector components	$\mathrm{m\,s^{-1}}$; m
$\mathbf{v_{weld}}$	Welding speed vector	$\mathrm{m\,s^{-1}}$
v_{weld_x}, v_{weld_y}, v_{weld_z}	Welding speed vector components	$\mathrm{m\,s^{-1}}$
w_k	Weighting factor	
w_l	Weighting factor	
x, y, z	Global spatial coordinates	m
x_{c}	x-coordinate of the center of the Lamé curves	m
x_{crystal}, $y_{crystal}$, $z_{crystal}$	Coordinates of the crystal axis	m
x^{C}, y^{C}, z^{C}	Coordinates of the point C from which the crystal starts growing	m
$x_{Lamé}$, $y_{Lamé}$, $z_{Lamé}$	Coordinates along the Lamé curves	m
X, Y, Z	Coordinates of the new intersection point $\mathrm{C_{new}}$	m

List of Figures

List of Tables

Bibliography

[1] J. Ready and D. Farson. *LIA Handbook of Laser Materials Processing*. Laser Institute of America, Magnolia Publishing Inc., 2001.

[2] X. Zhang, E. Ashida, S. Tarasawa, Y. Anma, M. Okada, S. Katayama, and M. Mizutani. "Welding of thick stainless steel plates up to 50 mm with high brightness lasers". In: *Journal of Laser Applications* 23.2 (2011), pp. 1–7, 022002.

[3] S. Weise. "Heißrißbildung beim Laserstrahlschweißen von Baustählen". PhD thesis. Bias Verlag Bremen, 1998.

[4] M. Wolf. "Zur Phänomenologie der Heißrissbildung beim Schweißen und Entwicklung aussagekräftiger Prüfverfahren". PhD thesis. Bundesanstalt für Materialforschung und -prüfung (BAM), 2006.

[5] C. E. Cross. "On the origin of weld solidification cracking". In: *Hot Cracking Phenomena in Welds*. Ed. by T. Böllinghaus and H. Herold. Springer, 2005, pp. 3–18.

[6] M. Gebhardt. "Einfluss von Konstruktion und Schweißparametern auf die Erstarrungsrissentstehung beim Laser-MSG-Hybridschweißen dickwandiger Bauteile. Experimentelle und numerische Analyse". PhD thesis. Bundesanstalt für Materialforschung und -prüfung (BAM), 2013.

[7] V. Penaranda. "Investigation of the Metallurgical and Thermo-Mechanical Factors Influencing Centreline Solidification Cracking by Laser Beam and Hybrid Welding". PhD thesis. Fraunhofer Verlag, 2020.

[8] T. Shida, H. Okumura, and Y. Kawada. "Effects of welding parameters and prevention of defects in deep penetration electron beam welding of heavy section steel plates". In: *Welding in the World* 17 (1979), pp. 196–207.

[9] Y. Kawahito, Y. Uemura, Y. Doi, M. Mizutani, K. Nishimoto, H. Kawakami, M. Tanaka, H. Fujii, K. Nakata, and S. Katayama. "Elucidation of the effect of welding speed on melt flows in high-brightness and high-power laser welding of stainless steel on basis of three-dimensional X-ray transmission in situ observation". In: *Welding International* 31.3 (2017), pp. 206–213.

[10] S. Tsukamoto, H. Irie, and M. Inagaki. "Welding defects and molten metal behaviour in electron beam welding". In: *Fundamental and Practical Approaches to the Reliability of Welded Structures: The Fourth International Symposium of the Japan Welding Society*. 1982, pp. 115–120.

[11] S. Tsukamoto and H. Irie. "Welding defects and molten metal behaviour in low speed electron beam welding". In: *Welding in the World* 23.5-6 (1985), pp. 130–141.

[12] S. Tsukamoto and H. Irie. "Mechanism of locally delayed solidification in electron beam welding". In: *Welding International* 5.3 (1991), pp. 177–183.

[13] J. Schuster, S. Keitel, E. Schulze, and H. Maly. "Fachbeiträge – Entstehung erstarrungsbedingter Risse in Laserstrahlschweißverbindungen an unlegierten und niedriglegierten Baustählen". In: *Schweißen und Schneiden* 51.5 (1999), pp. 252–257.

[14] J. Schuster. *Heißrisse in Schweißverbindungen: Entstehung, Nachweis und Vermeidung*. Deutscher Verlag für Schweißtechnik DVS, 2004.

[15] N. Bakir, A. Gumenyuk, and M. Rethmeier. *P 1241 - Untersuchung des Einflusses der konstruktiven Steifigkeit von dickwandigen laser- und laserhybridgeschweißten Verbindungen auf die Heißrissbildung*. Forschungsvereinigung Stahlanwendung e.V. (FOSTA), 2021.

[16] W. M. Steen and J. Mazumder. *Laser Material Processing*. Springer, 2010.

[17] A. Kohyama, Y. Arata, M. Tomie, and N. Igata. "Electron beam welding of titanium and Ti-6AL-4V thick plates". In: *Journal of Nuclear Materials* 122.1-3 (1984), pp. 772–776.

[18] M. Bachmann. "Numerische Modellierung einer elektromagnetischen Schmelzbadkontrolle beim Laserstrahlschweißen von nicht-ferromagnetischen Werkstoffen". PhD thesis. Bundesanstalt für Materialforschung und -prüfung (BAM), 2014.

[19] U. Dilthey. *Schweißtechnische Fertigungsverfahren 1: Schweiß- und Schneidtechnologien*. Springer, 2006.

[20] E. Beyer. *Schweißen mit Laser: Grundlagen*. Springer, 1995.

[21] S. Katayama, M. Mizutani, Y. Kawahito, S. Ito, and D. Sumimori. "Fundamental research of 100 kW fiber laser welding technology". In: *Proceedings of the Lasers in Manufacturing Conference (LiM), Munich, Germany*. 2015, pp. 22–25.

[22] C. Thomy, T. Seefeld, and F. Vollertsen. "Schweißen mit Hochleistungs-Faserlasern – Was sind die Vorteile, wo sind die Grenzen?" In: *Laser Technik Journal* 2.3 (2005), pp. 28–31.

[23] M. Bachmann, A. Gumenyuk, and M. Rethmeier. "Welding with high-power lasers: Trends and developments". In: *Physics Procedia* 83 (2016), pp. 15–25.

[24] F. Matsuda, H. Nakagawa, and T. Ueyama. "Solidification Crack Susceptibility in Laser Beam Weld Metal of 0.2 C-Low Alloy Steels: effects of Bead Configuration and S and P Contents". In: *Transactions of Joining and Welding Research Institute* 16.2 (1987), pp. 331–342.

[25] J. C. Hodge. "The welding of pressure vessels". In: *Journal of the American Society for Naval Engineers* 48.4 (1936), pp. 498–522.

[26] W. R. Apblett and W. S. Pellini. "Factors which influence weld hot cracking". In: *Welding Journal* 33.2 (1954), pp. 83-s–90-s.

[27] P. P. Puzak, W. R. Apblett, and W. S. Pellini. "Hot cracking of stainless steel weldments". In: *Welding Journal* 35.1 (1956), pp. 9-s–17-s.

[28] W. Jüptner, A. Kurgusow-Link, G. Sepold, and S. Weise. "Beitrag zum Vermeiden von Heißrissen beim Laserstrahlschweißen von Grobblechen aus unlegiertem Baustahl". In: *DVS Berichte* 176 (1996), pp. 215–233.

[29] D. Eskin and L. Katgerman. "A quest for a new hot tearing criterion". In: *Metallurgical and Materials Transactions A* 38.7 (2007), pp. 1511–1519.

[30] L. Katgerman and D. Eskin. "In search of the prediction of hot cracking in aluminium alloys". In: *Hot Cracking Phenomena in Welds II*. Ed. by T. Böllinghaus, H. Herold, C. E. Cross, and J. C. Lippold. Springer, 2008, pp. 11–26.

[31] C. E. Cross, N. Coniglio, P. Schempp, and M. Mousavi. "Critical conditions for weld solidification crack growth". In: *Hot Cracking Phenomena in Welds III*. Ed. by T. Böllinghaus, J. Lippold, and C. E. Cross. Springer, 2011, pp. 25–41.

[32] N. Bakir, A. Gumenyuk, and M. Rethmeier. "Numerical simulation of solidification crack formation during laser beam welding of austenitic stainless steels under external load". In: *Welding in the World* 60.5 (2016), pp. 1001–1008.

[33] V. A. Karkhin, S. Y. Ivanov, P. N. Homich, and P. Rajamaki. "Analysis of solute macro- and microsegregation in fusion welding". In: *Mathematical Modelling of Weld Phenomena*. Ed. by H.-H. Cerjak and N. Enzinger. Vol. 9. Verlag der Technischen Universität Graz, 2010, pp. 31–39.

[34] U. Dilthey. *Schweißtechnische Fertigungsverfahren 2: Verhalten der Werkstoffe beim Schweißen*. Springer, 2006.

[35] J. Lippold. *Welding Metallurgy and Weldability*. John Wiley & Sons, Inc., 2014.

[36] T. Zacharia. "Dynamic stresses in weld metal hot cracking". In: *Welding Journal* 73.7 (1994), pp. 164-s–172-s.

[37] C. E. Cross and T. Böllinghaus. "The effect of restraint on weld solidification cracking in aluminium". In: *Welding in the World* 50.11 (2006), pp. 51–54.

[38] P. Rajamäki. "Fusion weld metal solidification: continuum from weld interface to centerline". PhD thesis. Lappeenranta University of Technology, 2008.

[39] V. A. Karkhin. *Thermal Processes in Welding*. Springer, 2019.

[40] W. I. Pumphrey. "A consideration of the nature of brittleness at temperatures above the solidus in castings and welds in aluminium alloys". In: *Journal of the Institute of Metals* 75 (1948), pp. 235–256.

[41] N. N. Prokhorov. "The technological strength of metals while crystallising during welding". In: *Welding Production* 9.4 (1962), pp. 1–8. (in Russian).

[42] U. Feurer. "Influence of alloy composition and solidification conditions on dendrite arm spacing, feeding and hot tearing properties of aluminum alloys". In: *Quality control of engineering alloys and the role of metals science*. 1977, pp. 131–145.

[43] D. Manitsas and J. Andersson. "Hot cracking mechanisms in welding metallurgy: a review of theoretical approaches". In: *MATEC Web of Conferences*. Vol. 188. EDP Sciences, 2018, pp. 1–8, 03018.

[44] T. Kannengiesser and T. Boellinghaus. "Hot cracking tests – an overview of present technologies and applications". In: *Welding in the World* 58.3 (2014), pp. 397–421.

[45] S. Katayama, T. Fujimoto, and A. Matsunawa. "Correlation among solidification process, microstructure, microsegregation and solidification cracking susceptibility in stainless steel weld metals". In: *Transactions of Joining and Welding Research Institute* 14.1 (1985), pp. 123–138.

[46] Z. Tang. "Heißrissvermeidung beim Schweißen von Aluminiumlegierungen mit einem Scheibenlaser". PhD thesis. Universität Bremen, 2014.

[47] S. Kou. "A simple index for predicting the susceptibility to solidification cracking". In: *Welding Journal* 94 (2015), pp. 374-s–388-s.

[48] S. Kou. *Welding Metallurgy*. John Wiley & Sons, Inc., 2002.

[49] H. Thier. "Heißrissneigung unlegierter Werkstoffe unter besonderer Berücksichtigung des Sauerstoffgehaltes". In: *DVS Berichte* 117 (1989), pp. 10–16.

[50] J. Tösch, H. Schabereiter, E. Perteneder, and G. Rabensteiner. "Bedeutung und praktische Beeinflussbarkeit des Ferritgehaltes bei der Schweißung austenitischer Stähle". In: *Schweiß- und Prüftechnik Wien* 2 (1997), pp. 18–26.

[51] H. Krafka. "Risse in Schweißverbindungen – Heißrissarten, Heißrissentstehung und Heißrissprüfung". In: *Bericht Festigkeits- und Bruchverhalten von Fügeverbindungen*. Vol. 232. Deutscher Verband für Materialforschung und -prüfung DVM. 2000, pp. 161–171.

[52] Z. Tang and F. Vollertsen. "Influence of grain refinement on hot cracking in laser welding of aluminum". In: *Welding in the World* 58.3 (2014), pp. 355–366.

[53] *Merkblatt DVS 1004-2 – Heißrißprüfverfahren mit fremdbeanspruchten Proben*. Tech. rep. 1996.

[54] L. Barbetta, W. Weingaertner, O. Seffer, R. Lahdo, and S. Kaierle. "Influence of molten pool geometry and process parameters on solidification cracks formation in hybrid laser-GMA welding of thick 5L X70 steel plates". In: *ABCM International Congress of Manufacturing Engineering (COBEM), 8th Brazilian Congress of Manufacturing Engineering, Salvador, Bahia, Brazil*. 2015, pp. 18–22.

[55] F. Lu, X. Li, Z. Li, X. Tang, and H. Cui. "Formation and influence mechanism of keyhole-induced porosity in deep-penetration laser welding based on 3D transient modeling". In: *International Journal of Heat and Mass Transfer* 90 (2015), pp. 1143–1152.

[56] M. Sohail, S.-W. Han, S.-J. Na, A. Gumenyuk, and M. Rethmeier. "Numerical investigation of energy input characteristics for high-power fiber laser welding at different positions". In: *The International Journal of Advanced Manufacturing Technology* 80.5 (2015), pp. 931–946.

[57] Z. Gao, P. Jiang, G. Mi, L. Cao, and W. Liu. "Investigation on the weld bead profile transformation with the keyhole and molten pool dynamic behavior simulation in high power laser welding". In: *International Journal of Heat and Mass Transfer* 116 (2018), pp. 1304–1313.

[58] D. Radaj. *Schweißprozeßsimulation. Grundlagen und Anwendungen*. Deutscher Verlag für Schweißtechnik DVS, 1999.

[59] H. Ki, J. Mazumder, and P. S. Mohanty. "Modeling of laser keyhole welding: Part I. Mathematical modeling, numerical methodology, role of recoil pressure, multiple reflections, and free surface evolution". In: *Metallurgical and Materials Transactions A* 33.6 (2002), pp. 1817–1830.

[60] M. Dal and R. Fabbro. "An overview of the state of art in laser welding simulation". In: *Optics & Laser Technology* 78 (2016), pp. 2–14.

[61] D. Rosenthal. "The theory of moving sources of heat and its application of metal treatments". In: *Transactions of American Society of Mechanical Engineers* 68 (1946), pp. 849–866.

[62] H. Wilson. "On convection of heat". In: *Proceedings of the Cambridge Philosophical Society*. Vol. 12. 5. 1904, pp. 406–423.

[63] T. Zacharia, S. David, and J. Vitek. "Effect of evaporation and temperature-dependent material properties on weld pool development". In: *Metallurgical Transactions B* 22.2 (1991), pp. 233–241.

[64] K. Mundra, T. Debroy, T. Zacharia, and S. David. "Role of thermophysical properties in weld pool modeling". In: *Welding Journal* 71.9 (1992), pp. 313-s–320-s.

[65] W. Sudnik, D. Radaj, S. Breitschwerdt, and W. Erofeew. "Numerical simulation of weld pool geometry in laser beam welding". In: *Journal of Physics D: Applied Physics* 33.6 (2000), pp. 662–671.

[66] J. Dowden, M. Davis, and P. Kapadia. "Some aspects of the fluid dynamics of laser welding". In: *Journal of Fluid Mechanics* 126 (1983), pp. 123–146.

[67] J. Dowden, M. Davis, and P. Kapadia. "The flow of heat and the motion of the weld pool in penetration welding with a laser". In: *Journal of Applied Physics* 57.9 (1985), pp. 4474–4479.

[68] M. Beck. "Modellierung des Lasertiefschweißens". PhD thesis. Teubner Stuttgart, 1996.

[69] R. Rai, G. Roy, and T. DebRoy. "A computationally efficient model of convective heat transfer and solidification characteristics during keyhole mode laser welding". In: *Journal of Applied Physics* 101.5 (2007), pp. 1–11, 054909.

[70] K. Hong, D. Weckman, A. Strong, and W. Zheng. "Modelling turbulent thermofluid flow in stationary gas tungsten arc weld pools". In: *Science and Technology of Welding and Joining* 7.3 (2002), pp. 125–136.

[71] N. Chakraborty and S. Chakraborty. "Modelling of turbulent molten pool convection in laser welding of a copper–nickel dissimilar couple". In: *International Journal of Heat and Mass Transfer* 50.9-10 (2007), pp. 1805–1822.

[72] Y. Kawahito, K. Nakada, Y. Uemura, M. Mizutani, K. Nishimoto, H. Kawakami, and S. Katayama. "Relationship between melt flows based on three-dimensional X-ray transmission in situ observation and spatter reduction by angle of incidence and defocussing distance in high-power laser welding of stainless steel". In: *Welding International* 32.7 (2018), pp. 485–496.

[73] W. Tan, N. Bailey, and Y. Shin. "Investigation of keyhole plume and molten pool based on a three-dimensional dynamic model with sharp interface formulation". In: *Journal of Physics D: Applied Physics* 46.5 (2013), pp. 1–12, 055501.

[74] A. Kaplan. "A model of deep penetration laser welding based on calculation of the keyhole profile". In: *Journal of Physics D: Applied Physics* 27.9 (1994), pp. 1805–1814.

[75] Y. Kawahito, N. Matsumoto, Y. Abe, and S. Katayama. "Relationship of laser absorption to keyhole behavior in high power fiber laser welding of stainless steel and aluminum alloy". In: *Journal of Materials Processing Technology* 211.10 (2011), pp. 1563–1568.

[76] P. Ferro, F. Bonollo, A. Tiziani, and I. Magnabosco. "A Review of welding process numerical simulation: methodologies and experimental validations". In: *2nd International Conference and Exhibition on New Developments in Metallurgical Process Technology*. 2004, pp. 19–21.

[77] A. Otto and M. Schmidt. "Towards a universal numerical simulation model for laser material processing". In: *Physics Procedia* 5 (2010), pp. 35–46.

[78] V. G. Smith, W. A. Tiller, and J. Rutter. "A mathematical analysis of solute redistribution during solidification". In: *Canadian Journal of Physics* 33.12 (1955), pp. 723–745.

[79] N. N. Prokhorov. *Physical processes in metals during welding. Elements of physics of metals and solidification process*. Vol. 1. Metallurgiya, 1968. (in Russian).

[80] W. M. Robert. *Principles of Welding; Processes, Physics, Chemistry, and Metallurgy*. John Willey & Sons, 1999.

[81] M. Rappaz. "Modelling of microstructure formation in solidification processes". In: *International Materials Reviews* 34.1 (1989), pp. 93–124.

[82] S. Babu. "Thermodynamic and kinetic models for describing microstructure evolution during joining of metals and alloys". In: *International Materials Reviews* 54.6 (2009), pp. 333–367.

[83] K. G. F. Janssens, D. Raabe, E. Kozeschnik, M. A. Miodownik, and B. Nestler. *Computational materials engineering: an introduction to microstructure evolution*. Academic Press, 2010.

[84] W. Pfann. "Principles of zone-melting". In: *The Journal of the Minerals* 4.7 (1952), pp. 747–753.

[85] W. Kurz and D. Fisher. *Fundamentals of solidification*. Trans Tech Publications Ltd, 1998.

[86] G. L. Petrov. *Inhomogeneity of weld metal*. Leningrad: Sudpromgiz, 1963. (in Russian).

[87] V. Pavlyk. "Modelling and direct numerical simulation of dendritic structures under solidification conditions during fusion welding". PhD thesis. Shaker Verlag, 2004.

[88] T. V. Olshanskaya. "Technological Bases of Forming Welded Joints of Alloy Steels by Electron Beam Welding with Beam Sweeping". PhD thesis. PERM National Research Polytechnic University, 2018. (in Russian).

[89] V. A. Karkhin and A. Y. Pilipenko. "Modelling thermal cycles in the weld metal and the heat affected zone in beam methods of welding thick plates". In: *Welding International* 11.5 (1997), pp. 401–403.

[90] N. N. Rykalin. *Calculation of Heat Flow in Welding*. translated by Z. Paley and C.M. Adams, Jr. Trans., 1951.

[91] J. Goldak, A. Chakravarti, and M. Bibby. "A new finite element model for welding heat sources". In: *Metallurgical Transactions B* 15.2 (1984), pp. 299–305.

[92] V. A. Karkhin, P. N. Homich, and V. Michailov. "Models for volume heat sources and functional-analytical technique for calculating the temperature fields in butt welding". In: *Mathematical Modeling of Welding Phenomena*. Ed. by H.-H. Cerjak, H. K. D. H. Bhadeshia, and E. Kozeschnik. Vol. 8. Verlag der Technischen Universität Graz, 2007, pp. 819–834.

[93] J. Chukkan, M. Vasudevan, S. Muthukumaran, R. Kumar, and N. Chandrasekhar. "Simulation of laser butt welding of AISI 316L stainless steel sheet using various heat sources and experimental validation". In: *Journal of Materials Processing Technology* 219 (2015), pp. 48–59.

[94] D. Radaj, H. Häuser, and S. Braun. "Numerische Simulation von Eigenspannungen und Verzug bei Schweißverbindungen aus AlMgSi-Legierungen". In: *Konstruktion* 50.7-8 (1998), pp. 31–37.

[95] R. P. Turner, C. Panwisawas, Y. Sovani, B. Perumal, R. M. Ward, H. C. Basoalto, and J. Brooks. "Linking a CFD and FE analysis for welding simulations in Ti-6Al-4V". In: *10th International Conference on Trends in Welding Research and 9th International Welding Symposium of Japan Welding Society (9WS), Tokyo, Japan*. 2016, pp. 11–14.

[96] W. Tan and Y. Shin. "Analysis of multi-phase interaction and its effects on keyhole dynamics with a multi-physics numerical model". In: *Journal of Physics D: Applied Physics* 47.34 (2014), pp. 1–17, 345501.

[97] S. Katayama. *Fundamentals and Details of Laser Welding*. Springer, 2020.

[98] A. Pilipenko. "Computer simulation of residual stress and distortion of thick plates in multielectrode submerged arc welding. Their mitigation techniques". PhD thesis. Norwegian University of Science and Technology, 2001.

[99] D. Radaj. *Eigenspannungen und Verzug beim Schweißen: Berechnungs- und Meßverfahren*. Deutscher Verlag für Schweißtechnik DVS, 2002.

[100] *ISO/TS 18166:2016 - Numerical welding simulation – Execution and documentation*. 2016.

[101] C. Schwenk. "FE-Simulation des Schweißverzugs laserstrahlgeschweißter dünner Bleche". PhD thesis. Bundesanstalt für Materialforschung und -prüfung (BAM), 2007.

[102] J. Hildebrand. "Numerische Schweißsimulation – Bestimmung von Temperatur, Gefüge und Eigenspannung an Schweißverbindungen aus Stahl- und Glaswerkstoffen". PhD thesis. Bauhaus-Universität Weimar, 2009.

[103] T. Nitschke-Pagel and H. Wohlfahrt. "Residual Stresses in Welded Joints – Sources and Consequences". In: *Residual Stresses VI, ECRS6*. Vol. 404. Materials Science Forum. Trans Tech Publications Ltd, 2002, pp. 215–226.

[104] Y. Ueda, K. Fukuda, and K. Nakacho. "Basic procedures in analysis and measurement of welding residual stresses by the finite element method". In: *Proceedings, International Conference on Residual Stresses in Welded Construction and Their Effects*. 1977, pp. 27–37.

[105] L. Karlsson. "Thermal stresses in welding". In: *Thermal stresses*. Elsevier, 1986, pp. 299–389.

[106] L.-E. Lindgren. *Computational welding mechanics*. Elsevier, 2014.

[107] *DIN EN 10025-2:2019: Hot rolled products of structural steels – Part 2: Technical delivery conditions for non-alloy structural steels*. 2005.

[108] *DIN EN 10088-3:2014: Stainless steels – Part 3: Technical delivery conditions for semi-finished products, bars, rods, wire, sections and bright products of corrosion resisting steels for general purposes*. 2014.

[109] E. Weck and E. Leistner. *Metallographic instructions for colour etching by immersion. Part III: Non-ferrous metals, cemented carbides and ferrous metals, nickel-base and cobalt-base alloys*. Deutscher Verlag für Schweißtechnik DVS, 1986.

[110] R. Zhang, X. Tang, L. Xu, F. Lu, and H. Cui. "Study of molten pool dynamics and porosity formation mechanism in full penetration fiber laser welding of Al-alloy". In: *International Journal of Heat and Mass Transfer* 148 (2020), pp. 1–14, 119089.

[111] X. Wen, D. Wu, P. Zhang, S. Liu, Z. Luo, Z. Jia, X. Ye, H. Shi, and Z. Yu. "Influence mechanism of the keyhole behavior on penetration depth by in-situ monitoring in pulsed laser welding of aluminum alloy". In: *Optik* 246 (2021), pp. 1–12, 167812.

[112] M. Bachmann, V. Avilov, A. Gumenyuk, and M. Rethmeier. "Numerical simulation of full-penetration laser beam welding of thick aluminium plates with inductive support". In: *Journal of Physics D: Applied Physics* 45.3 (2011), pp. 1–13, 035201.

[113] T. Faber. *Fluid Dynamics for Physicists*. Cambridge University Press, 1995.

[114] M. Zhang, G. Chen, Y. Zhou, and S. Li. "Direct observation of keyhole characteristics in deep penetration laser welding with a 10 kW fiber laser". In: *Optics Express* 21.17 (2013), pp. 1–8.

[115] P. G. Klemens. "Heat balance and flow conditions for electron beam and laser welding". In: *Journal of Applied Physics* 47.5 (1976), pp. 2165–2174.

[116] P. Y. Shcheglov, S. Uspenskiy, A. Gumenyuk, V. Petrovskiy, M. Rethmeier, and V. Yermachenko. "Plume attenuation of laser radiation during high power fiber laser welding". In: *Laser Physics Letters* 8.6 (2011), pp. 475–480.

[117] P. Y. Shcheglov, A. Gumenyuk, I. B. Gornushkin, M. Rethmeier, and V. Petrovskiy. "Vapor-plasma plume investigation during high-power fiber laser welding". In: *Laser Physics* 23.1 (2012), pp. 1–8, 016001.

[118] H. Hügel and F. Dausinger. "1.1 Fundamentals of laser-induced processes". In: *Laser Physics and Applications*. Ed. by R. Poprawe, H. Weber, and G. Herziger. Vol. 1C. Springer, 2004, pp. 25–68.

[119] N. Chakraborty. "The effects of turbulence on molten pool transport during melting and solidification processes in continuous conduction mode laser welding of copper–nickel dissimilar couple". In: *Applied Thermal Engineering* 29.17 (2009), pp. 3618–3631.

[120] D. C. Wilcox. *Turbulence modeling for CFD*. Vol. 2. DCW Industries, Incorporated, 1994.

[121] J. Wagner, P. Berger, P. He, F. Fetzer, R. Weber, and T. Graf. "Reduced finite-volume model for the fast numerical calculation of the fluid flow in the melt pool in laser beam welding". In: *Institute of Physics Conference Series: Materials Science and Engineering*. Vol. 1135. 1. Institute of Physics Publishing. 2021, pp. 1–9, 012010.

[122] *COMSOL Multiphysics® v. 5.3 COMSOL AB, Stockholm, Sweden*.

[123] P. C. Carman. "Fluid flow through granular beds". In: *Chemical Engineering Research and Design* 75 (1997), pp. S32–S48.

[124] A. Brent, V. Voller, and K. Reid. "Enthalpy-porosity technique for modeling convection-diffusion phase change: application to the melting of a pure metal". In: *Numerical Heat Transfer, Part A Applications* 13.3 (1988), pp. 297–318.

[125] V. Voller and C. Prakash. "A fixed grid numerical modelling methodology for convection-diffusion mushy region phase-change problems". In: *International Journal of Heat and Mass Transfer* 30.8 (1987), pp. 1709–1719.

[126] I. N. Bronstein, J. Hromkovic, B. Luderer, H.-R. Schwarz, J. Blath, A. Schied, S. Dempe, G. Wanka, and S. Gottwald. *Taschenbuch der Mathematik*. Vol. 1. Springer, 2012.

[127] J. Larsson. "Numerical simulation of turbulent flows for turbine blade heat transfer applications". PhD thesis. Chalmers University of Technology, 1998.

[128] *COMSOL Multiphysics Reference Manual, COMSOL Multiphysics® v. 5.3. COMSOL AB, Stockholm, Sweden*.

[129] H. Hashemi and C. Sliepcevich. "A numerical method for solving two-dimensional problems of heat conduction with change of phase". In: *Chemical Engineering Progress Symposium Series*. Vol. 63. 79. 1967, pp. 34–41.

[130] M. Hansen. *Constitution of binary alloys*. McGraw-Hill Book Company Inc, 1958.

[131] M. Salcudean and Z. Abdullah. "On the numerical modelling of heat transfer during solidification processes". In: *International Journal for Numerical Methods in Engineering* 25.2 (1988), pp. 445–473.

[132] W. M. Kays. "Turbulent Prandtl Number – Where Are We?" In: *Journal of Heat Transfer* 116.2 (1994), pp. 284–295.

[133] B. Weigand, J. R. Ferguson, and M. E. Crawford. "An extended Kays and Crawford turbulent Prandtl number model". In: *International Journal of Heat and Mass Transfer* 40.17 (1997), pp. 4191–4196.

[134] Y. Kim and W. Kim. "A numerical analysis of heat and fluid flow with a deformable curved free surface in a laser melting process". In: *International Journal of Heat and Fluid Flow* 29.5 (2008), pp. 1481–1493.

[135] K. Mills, B. Keene, R. Brooks, and A. Shirali. "Marangoni effects in welding". In: *Philosophical Transactions of the Royal Society of London. Series A: Mathematical, Physical and Engineering Sciences* 356.1739 (1998), pp. 911–925.

[136] A. Lundbäck and H. Runnemalm. "Validation of three-dimensional finite element model for electron beam welding of Inconel 718". In: *Science and Technology of Welding and Joining* 10.6 (2005), pp. 717–724.

[137] *Abaqus Theory Guide Dassault Systèmes Simulia Corp. Providence, RI, USA 2016*.

[138] *ANSYS Mechanical APDL Theory Reference, ANSYS® 2020 R1, ANSYS, Inc.*

[139] Y. Bergström. *The Plastic Deformation of Metals: a Dislocation Model and Its Applicability*. Reviews on powder metallurgy and physical ceramics. Freund Publishing House, 1983.

[140] E. Arzt. "Size effects in materials due to microstructural and dimensional constraints: a comparative review". In: *Acta Materialia* 46.16 (1998), pp. 5611–5626.

[141] V. A. Karkhin and K. M. Gatovskii. *Theory of welding stresses and deformations*. Leningrad Shipbuilding Institute, 1980. (in Russian).

[142] N. Bailey. *Weldability of Ferritic Steels*. Elsevier, 1994.

[143] H. K. D. H. Bhadeshia and L. E. Svensson. "Modelling the evolution of microstructure in steel weld metal". In: *Mathematical Modelling of Weld Phenomena*. Ed. by H.-H. Cerjak and K. E. Easterling. Vol. 1. Verlag der Technischen Universität Graz, 1993, pp. 109–182.

[144] M. Macedo, A. Cota, and F. Araújo. "The kinetics of austenite formation at high heating rates". In: *Rem: Revista Escola de Minas* 64 (2011), pp. 163–167.

[145] P. Seyffarth, B. Meyer, and A. Scharff. *Großer Atlas Schweiß-ZTU-Schaubilder*. Deutscher Verlag für Schweißtechnik DVS, 1992.

[146] *ESI Group Material database*. 2009.

[147] F. Richter. *Physikalische Eigenschaften von Stählen und ihre Temperaturabhängigkeit: Polynome und graphische Darstellungen*. Verlag Stahleisen, 1983.

[148] K. Mills. *Recommended values of thermophysical properties for selected commercial alloys*. Woodhead Publishing, 2002.

[149] U. Peil and M. Wichers. "Schweißen unter Betriebsbeanspruchung – Werkstoffkennwerte für einen S355J2G3 unter Temperaturen bis 1200 C". In: *Stahlbau* 73.6 (2004), pp. 400–415.

[150] U. Peil and M. Wichers. "Schweißen unter Betriebsbeanspruchung – Werkstoffkennwerte zur Temperaturfeldberechnung für einen S355J2G3". In: *Stahlbau* 74.4 (2005), pp. 249–257.

[151] C. Y. Ho and R. E. Taylor. *Thermal Expansion of Solids*. Vol. 4. Advanced Semiconductor Materials International, 1998.

[152] P. Sahoo, T. Debroy, and M. McNallan. "Surface tension of binary metal-surface active solute systems under conditions relevant to welding metallurgy". In: *Metallurgical Transactions B* 19.3 (1988), pp. 483–491.

[153] B. J. Keene, K. Mills, J. Bryant, and E. Hondros. "Effects of interaction between surface active elements on the surface tension of iron". In: *Canadian Metallurgical Quarterly* 21.4 (1982), pp. 393–403.

[154] M. Farajian. "Welding residual stress behavior under mechanical loading". In: *Welding in the World* 57.2 (2013), pp. 157–169.

[155] M. Seif, L. Choe, J. Gross, W. Luecke, J. Main, D. McColskey, F. Sadek, M. Seif, J. Weigand, and C. Zhang. *Temperature-dependent material modeling for structural steels: formulation and application*. US Department of Commerce, National Institute of Standards and Technology NIST, 2016.

[156] O. Kaitila. *Finite Element Modelling of Cold-Formed Steel Members at High Temperatures*. Tech. rep. 2002, pp. 1–90.

[157] J. Dworak. "Laser-welding technologies. Results of investigations and possible applications". In: *Welding International* 21.1 (2007), pp. 5–11.

[158] A. Warren, S. Bate, R. Charles, and C. Watson. "The effect of phase transformations on predicted values of residual stresses in welded ferritic components". In: *Materials Science Forum*. Vol. 524. 2006, pp. 827–832.

[159] P. Knoedel, S. Gkatzogiannis, and T. Ummenhofer. "Practical aspects of welding residual stress simulation". In: *Journal of Constructional Steel Research* 132 (2017), pp. 83–96.

[160] *MATLAB version 9.7.0.1190202 (R2018a)*. Natick, Massachusetts, 2018.

[161] G. A. Korn and T. M. Korn. *Mathematical Handbook for Scientists and Engineers: Definitions, Theorems, and Formulas for Reference and Review*. Courier Corporation, 2000.

[162] W. Research. *Hypergeometric2F1*. `https://reference.wolfram.com/language/ref/Hypergeometric2F1.html`. 2022.

Publications and Academic Activities

Journal Publications

AJ1 A. Artinov, M. Bachmann, M. Rethmeier. "Equivalent heat source approach in a 3D transient heat transfer simulation of full-penetration high power laser beam welding of thick metal plates". In: *International Journal of Heat and Mass Transfer*, 122, (2018), pp. 1003–1013.

AJ2 N. Bakir, A. Artinov, A. Gumenyuk, M. Bachmann, M. Rethmeier. "Numerical simulation on the origin of solidification cracking in laser welded thick-walled structures". In: *Metals*, 8.6, (2018), pp. 1–15, 406.

AJ3 F. Lange, A. Artinov, M. Bachmann, M. Rethmeier, K. Hilgenberg. "Numerical simulation of the weld pool dynamics during pulsed laser welding using adapted heat source models". In: *Procedia CIRP*, 74, (2018), pp. 679–682.

AJ4 A. Artinov, N. Bakir, M. Bachmann, A. Gumenyuk, M. Rethmeier. "Weld pool shape observation in high power laser beam welding". In: *Procedia CIRP*, 74, (2018), pp. 683–686.

AJ5 S. Ivanov, A. Artinov, E. Valdaytseva, S. Stankevich, G. Turichin. "A simplified model for numerical simulation of laser metal deposition process with beam oscillation". In: *Journal of Physics: Conference Series*, 1109, (2018), pp. 1–8, 012006.

AJ6 A. Artinov, N. Bakir, M. Bachmann, A. Gumenyuk , S.-J. Na, M. Rethmeier. "On the search for the origin of the bulge effect in high power laser beam welding". In: *Journal of Laser Applications*, 31.2, (2019), pp. 1–7, 022413.

AJ7 A. Artinov, V. Karkhin. "Comparison of the size of the weld end crater and the steady-state weld pool". In: *Welding and Diagnostics*, ISSN 2071-5234, (2019), pp. 19–23. (in Russian).

AJ8 X. Meng, A. Artinov, M. Bachmann, M. Rethmeier. "Numerical and experimental investigation of thermo-fluid flow and element transport in electromagnetic stirring enhanced wire feed laser beam welding". In: *International Journal of Heat and Mass Transfer*, 144, (2019), pp. 1–11, 118663.

AJ9 A. Artinov, V. Karkhin, P. Khomich, M. Bachmann, M. Rethmeier. "Assessment of thermal cycles by combining thermo-fluid dynamics and heat conduction in keyhole mode welding processes". In: *International Journal of Thermal Sciences*, 145, (2019), pp. 1–10, 105981.

AJ10 X. Meng, M. Bachmann, A. Artinov, M. Rethmeier. "Experimental and numerical assessment of weld pool behavior and final microstructure in wire feed laser beam welding with electromagnetic stirring". In: *Journal of Manufacturing Processes*, 45, (2019), pp. 408–418.

AJ11 S. Ivanov, A. Vildanov, P. Golovin, A. Artinov, I. Karpov. "Effect of inter-layer dwell time on distortion and residual stresses of laser metal deposited wall". In *Key Engineering Materials*, 822, (2019), pp. 445–451.

AJ12 A. Artinov, V. Karkhin, P. Khomich, M. Bachmann, M. Rethmeier. "Modeling of fluid dynamics and thermal processes of full penetration laser beam welding". In: *Machine Technology*, ISSN 0491-6441, (2019), pp. 58–69. (in Russian)

AJ13 A. Artinov, V. Karkhin, M. Bachmann, M. Rethmeier. "Mathematical modeling of the geometrical differences between the weld end crater and the steady-state weld pool". In: *Journal of Laser Applications*, 32.2, (2020), pp. 1–6, 022024.

AJ14 X. Meng, A. Artinov, M. Bachmann, M. Rethmeier. "Theoretical study of influence of electromagnetic stirring on transport phenomena in wire feed laser beam welding". In: *Journal of Laser Applications*, 32.2, (2020), pp. 1–9, 022026.

AJ15 A. Artinov, V. Karkhin, N. Bakir, X. Meng, M. Bachmann, A. Gumenyuk, M. Rethmeier. "Lamé curve approximation for the assessment of the 3D temperature distribution in keyhole mode welding processes". In: *Journal of Laser Applications*, 32.2, (2020), pp. 1–9, 022042.

AJ16 X. Meng, A. Artinov, M. Bachmann, M. Rethmeier. "Numerical study of additional element transport in wire feed laser beam welding". In: *Procedia CIRP*, 94, (2020), pp. 722–725.

AJ17 A. Artinov, M. Bachmann, X. Meng, V. Karkhin, M. Rethmeier. "On the relationship between the bulge effect and the hot cracking formation during deep penetration laser beam welding". In: *Procedia CIRP*, 94, (2020), pp. 5–10.

AJ18 X. Meng, M. Bachmann, A. Artinov, M. Rethmeier. "The influence of magnetic field orientation on metal mixing in electromagnetic stirring enhanced wire feed laser beam welding". In: *Journal of Materials Processing Technology*, 294, (2021), pp. 1–12, 117135.

AJ19 A. Artinov, X. Meng, M. Bachmann, M. Rethmeier. "Numerical analysis of the partial penetration high power laser beam welding of thick sheets at high process speeds". In: *Metals*, 11, (2021), pp. 1–16, 1319.

AJ20 S. Ivanov, M. Gushchina, A. Artinov, M. Khomutov, E. Zemlyakov. "Effect of elevated temperatures on the mechanical properties of a direct laser deposited Ti-6Al-4V". In: *Materials*, 14, (2021), pp. 1–17, 6432.

AJ21 A. Artinov, M. Bachmann, M. Rethmeier, V. Karkhin, P. Khomich. "Modeling of hydrodynamic and thermal processes at laser welding with through penetration." In: *Welding International*, 36, (2021), pp. 25–36.

AJ22 S. Ivanov, A. Artinov, E. Zemlyakov, I. Karpov, S. Rylov, V. Em. "Spatiotemporal evolution of stress field during direct laser deposition of multilayer thin wall of Ti-6Al-4V". In: *Materials*, 15.1, (2021), pp. 1–20, 263.

AJ23 A. Artinov, X. Meng, M. Bachmann, M. Rethmeier. "Study on the transition behavior of the bulging effect during deep penetration laser beam welding". In: *International Journal of Heat and Mass Transfer*, 184, (2021), pp. 1–15, 122171.

AJ24 A. Artinov, X. Meng, N. Bakir, Ö. Üstündağ, M. Bachmann, A. Gumenyuk, M. Rethmeier. "The bulging effect and its relevance in high power laser beam welding". In: *IOP Conference Series: Materials Science and Engineering*, Vol. 1135, (2021), pp. 1–11, 012003.

AJ25 M. Bachmann, X. Meng, A. Artinov, M. Rethmeier. "Elucidation of the bulging effect by an improved ray-tracing algorithm in deep penetration wire feed laser beam welding and its influence on the mixing behavior". In: *Advanced Engineering Materials*, 184, (2022), pp. 1–9, 2101299.

AJ26 X. Meng, M. Bachmann, A. Artinov, M. Rethmeier. "A study of the magnetohydrodynamic effect on keyhole dynamics and defect mitigation in laser beam welding". In: *Journal of Materials Processing Technology*, 307, (2022), pp. 1–10, 117636.

AJ27 X. Meng, M. Bachmann, A. Artinov, M. Rethmeier. "The detrimental molten pool narrowing phenomenon in wire feed laser beam welding and its suppression by magnetohydrodynamic technique". In: *International Journal of Heat and Mass Transfer*, 193, (2022), pp. 1–13, 122913.

AJ28 M. Bachmann, X. Meng, A. Artinov, M. Rethmeier. "Evaluation of narrowed weld pool shapes and their effect on resulting potential defects during deep penetration laser beam welding". In: *Journal of Laser Applications*, 34.4, (2022), pp. 1–7, 042005.

AJ29 X. Meng, S.N. Putra, M. Bachmann, A. Artinov, M. Rethmeier. "Influence of the free surface reconstruction on the spatial laser energy distribution in high power laser beam welding modeling". In: *Journal of Laser Applications*, 34.4, (2022), pp. 1–8, 042023.

AJ30 A. Artinov, V. Karkhin, X. Meng, M. Bachmann, M. Rethmeier. "A general analytical solution for two-dimensional columnar crystal growth during laser beam welding of thin steel sheets". In: *Applied Sciences*, 13.10, (2023), pp. 1–10, 6249.

Conference Proceedings

AC1 A. Artinov, M. Bachmann, M. Rethmeier. "Äquivalente Wämequellenmodellierung beim Hochleistungslaserstrahlschweißen dicker Bleche". In: *Assistentenseminar der Wissenschaftlichen Gesellschaft Fügetechnik e.V. im DVS*, Rabenau, 2017, pp. 66–76.

AC2 A. Artinov, M. Bachmann, M. Rethmeier. "Transient process simulation of heat transfer in laser beam welding with an equivalent heat source". In: *Proceedings of the 2017 COMSOL Conference in Roterdam*, 2017, pp. 1–7.

AC3 A. Artinov, M. Bachmann, V. Karkhin, M. Rethmeier. "A novel approach for calculating the thermal cycle of a laser beam welding process using a stationary CFD model". In: *Mathematical Modelling of Weld Phenomena*. Ed. by C. Sommitsch, N. Enzinger, and P. Mayer. Vol. 12. Verlag der Technischen Universität Graz, 2018, pp. 694–710.

AC4 M. Bachmann, A. Artinov, X. Meng, M. Rethmeier. "Numerical study of the bulging effect in deep penetration laser beam welding". In: *Lasers in Manufacturing (LiM)*, (online conference), 2021, pp. 1–8.

AC5 X. Meng, A. Artinov, M. Bachmann, Ö. Üstündağ, A. Gumenyuk, M. Rethmeier. "A numerical study on the suppression of detrimental weld pool profile in wire feed laser beam welding of magnetohydrodynamic technique". In: *Mathematical Modelling of Weld Phenomena*. Ed. by C. Sommitsch, N. Enzinger, and P. Mayer. Vol. 13. Verlag der Technischen Universität Graz, 2023.

AC6 F. Yang, M. Bachmann, X. Meng, A. Artinov, M. Rethmeier. "Numerical analysis of the influence of the auxiliary oscillating magnetic field on the suppressing the porosity formation in deep penetration laser beam welding of aluminum alloy". In: *Mathematical Modelling of Weld Phenomena*. Ed. by C. Sommitsch, N. Enzinger, and P. Mayer. Vol. 13. Verlag der Technischen Universität Graz, 2023.

AC7 A. Artinov, P. Kising, M. Bachmann, X. Meng, M. Rethmeier. "Numerical analysis of the dependency of the weld pool shape on turbulence and thermodynamic activity of solutes in laser beam welding of unalloyed steels". In: *Mathematical Modelling of Weld Phenomena*. Ed. by C. Sommitsch, N. Enzinger, and P. Mayer. Vol. 13. Verlag der Technischen Universität Graz, 2023.

AC8 A. Artinov, X. Meng, M. Bachmann, M. Rethmeier. "Numerical study on the formation of a bulging region in partial penetration laser beam welding". In: *Mathematical Modelling of Weld Phenomena*. Ed. by C. Sommitsch, N. Enzinger, and P. Mayer. Vol. 13. Verlag der Technischen Universität Graz, 2023.

Presentations

AP1 *Assistentenseminar der Wissenschaftlichen Gesellschaft Fügetechnik*. Rabenau, Germany, September 2017, Oral Presentation

AP2 *COMSOL Conference*. Rotterdam, Netherlands, October 2017, Oral Presentation

AP3 *BAM Alumni Kolloquium*. Berlin, Germany, November 2017, Oral Presentation

AP4 *10th CIRP Conference on Photonic Technologies (LANE)*. Führt, Germany, September 2018, Oral Presentation

AP5 *9th Beam Technologies & Laser Applications Conference*. Saint Petersburg, Russia, September 2018, Oral Presentation

AP6 *12th International Seminar on Numerical Analysis of Weldability*. Graz-Seggau, Austria, September 2018, Oral Presentation

AP7 *International Congress on Applications of Lasers & Electro-Optics*. Orlando, United States, October 2018, Oral Presentation

AP8 *Trends in Joining*. Cottbus, Germany, November 2018, Oral Presentation

AP9 *72nd International Institute of Welding Annual Assembly*. Bratislava, Slovakia, July 2019, Oral Presentation

AP10 *International Congress on Applications of Lasers & Electro-Optics*. Orlando, United States, October 2019, Oral Presentation

AP11 *11th CIRP Conference on Photonic Technologies (LANE)*. Führt, Germany, September 2020, Keynote Presentation (online)

AP12 *Lasers in Manufacturing*. Erlangen, Germany, September 2021, Oral Presentation (online)

AP13 *10th Beam Technologies & Laser Applications Conference*. Saint Petersburg, Russia, September 2021, Oral Presentation (online)

AP14 *13th International Seminar on Numerical Analysis of Weldability*. Graz-Seggau, Austria, September 2022, Oral Presentation

AP15 *International Congress on Applications of Lasers & Electro-Optics*. Orlando, United States, October 2022, Oral Presentation

Awards

- Best presentation award from the 10th CIRP Conference on Photonic Technologies
- IIW Kenneth Easterling Best Paper Award from the 13th International Seminar "Numerical Analysis of Weldability"